Effect of Stress Field on Self-Assembly in Crystalline Polyolefins

Mizuki KISHIMOTO

2022

Contents

Chapter 3
Spatial Distribution of the Amorphous Region with Reduced Mobility

Chapter 4
Effect of Stress Field on the Mechanical Behavior of PE

Chapter 5
Factors Governing the Strain-Induced Density Fluctuations in PE

Chapter 6
Spatial Inhomogeneity of Chain Orientation Associated with the Strain-Induced Density Fluctuations in PE

Chapter 1
General Introduction

1.1 Hierarchical Structures in Crystalline Polyolefins

Polyolefins are polymers consisting of simple alkenes as monomers. Typical examples are polyethylene (PE) and polypropylene (PP).[1] Even though they are relatively inexpensive among polymer materials, they have low weight and excellent mechanical properties, and show good weatherability since they do not have double bonds and are resistant to degradation. They also show excellent water and chemical resistances. For such reasons, they are used in a wide range of applications such as containers, bags, and automotive materials, and thus are one of the most important materials for daily life. The superior physical properties of the polyolefins are owing to their hierarchical structures.

When crystalline polymer materials, including crystalline polyolefins, crystallize from melt in a static field, they form hierarchical structures over a wide spatial scale, as shown in figure 1.1.[2] On the scale of Å, the chains are systematically folded and packed to form crystalline lattice structures. Wide-angle X-ray scattering (WAXS) is the most commonly used for analysis. On the scale of nm, crystalline and amorphous phases are alternately stacked to form lamellar structures. They can be observed by electron microscopy, atomic force microscopy (AFM), small-angle X-ray scattering (SAXS), etc. On the scale of a couple of 100 nm, or submicron scale, the grown lamellae form branching structures. They are also observed by electron microscopy, AFM, ultra-small-angle X-ray scattering (USAXS), etc. On the scale larger than μm, the lamellar branching

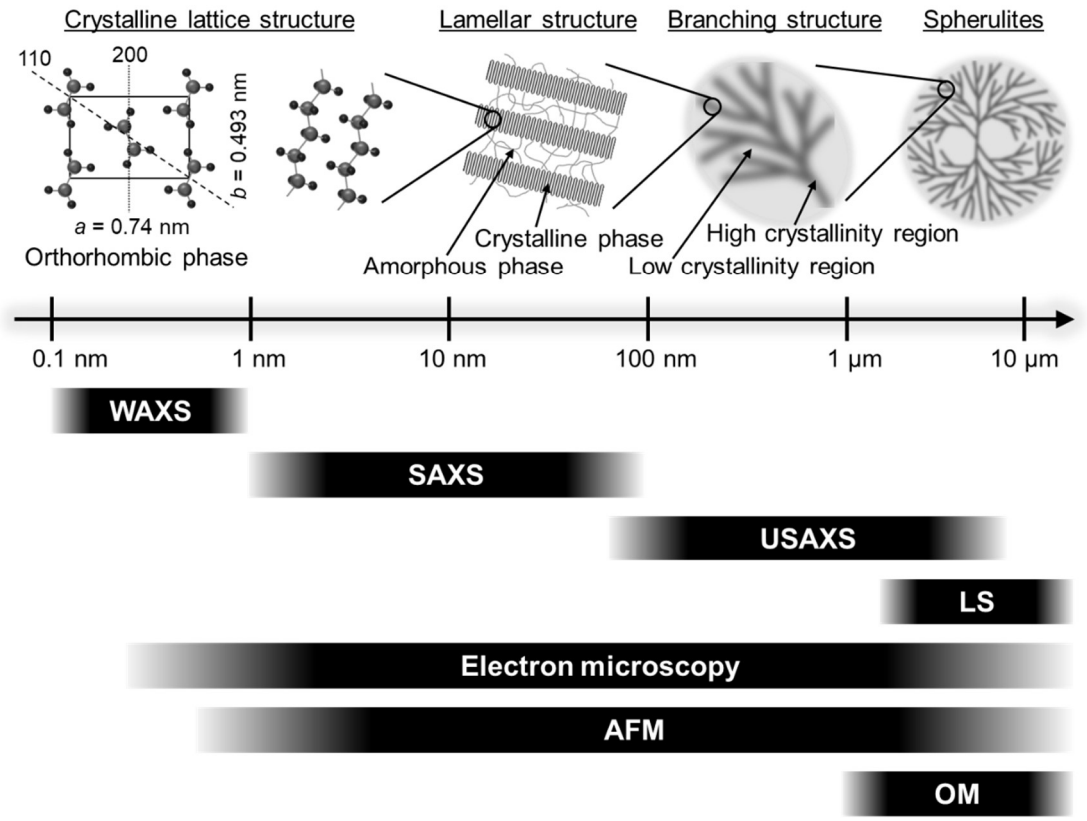

Figure 1.1 Hierarchical structures in crystalline polymers (example of PE) and typical observation techniques.

structures fill the spherulitic structures. Optical microscope (OM) is the most commonly used for observations. Light scattering (LS) can also be applied for samples with high transmittance.

1.2 Effect of Stress Field on Crystallization Process

The self-assembly of the hierarchical structures described above is affected by the stress field in the system. In the formation of the crystalline lattice structures and the lamellar structures associating with chain folding, the spatial inhomogeneity of the stress field caused by the spatial inhomogeneity of the entanglements affects the formation.

In the crystallization from melts, a nucleus first forms, and then the chains attach to the nucleus. The formation of a three-dimensional (3D) nucleus in the melt is called primary nucleation, and the attachment of chains to the nucleus to form a two-dimensional (2D) nucleus is called secondary nucleation. When the primary nucleus forms consisting of a length l and a width a as shown in Figure 1.2(a), the change in the free energy of formation $\Delta\phi_1$ associating with the primary nucleus is expressed as[3]

$$\Delta\phi_1 = 2a^2\sigma_e + 4al\sigma - a^2 l\Delta f \tag{1.1}$$

where, σ_e, σ, and Δf are the surface free energy of the chain folding plane, the surface free energy of the plane along the chain, and the free energy of fusion per unit volume, respectively. Differentiating by a and l, respectively, the size of the critical nucleus can be obtained as

$$a_1{}^* = \frac{4\sigma}{\Delta f} = \frac{4\sigma T_m{}^0}{\Delta H \Delta T} \tag{1.2}$$

$$l_1{}^* = \frac{4\sigma_e}{\Delta f} = \frac{4\sigma_e T_m{}^0}{\Delta H \Delta T} \tag{1.3}$$

$$\Delta\phi_1{}^* = \frac{32\sigma_e\sigma^2}{\Delta f} \tag{1.4}$$

$T_m{}^0$ is the equilibrium melting temperature, ΔT is the degree of supercooling, and ΔH is the enthalpy of fusion per unit volume. Actually, the primary nucleation cannot be directly observed, but the secondary nucleation can. The free energy required for secondary nucleation is much lower than that for primary nucleation. Therefore, chains sequentially attach and the crystal growth proceeds until the growth front collides with the neighboring

spherulites. The secondary nucleation model is called Lauritzen-Hoffman (L-H) theory.[3,4] As shown in Figure 1.2(b), when the secondary nucleus forms consisting of a length l, a width a, and a stem thickness b_s, $\Delta\phi$ associating with secondary nucleus is expressed as[3,4]

$$\Delta\phi = 2ab_s\sigma_e + 2b_s l\sigma - ab_s l\Delta f \tag{1.5}$$

Differentiating by a and l, respectively, the size of the critical nucleus can be obtained as

$$a^* = \frac{2\sigma}{\Delta f} = \frac{2\sigma {T_m}^0}{\Delta H \Delta T} \tag{1.6}$$

$$l^* = \frac{2\sigma_e}{\Delta f} = \frac{2\sigma_e {T_m}^0}{\Delta H \Delta T} \tag{1.7}$$

$$\Delta\phi^* = \frac{4b_s\sigma_e\sigma}{\Delta f} \tag{1.8}$$

The crystal growth rate G at the crystallization temperature T_c is expressed as the rate of overcoming the barrier that is the sum of the critical nucleation energy $\Delta\phi^*$ and the mole energy of chain diffusion ΔE.[3,4]

$$G = G_0 \exp\left(\frac{-\Delta E}{RT_c}\right)\exp\left(\frac{-K}{T_c \Delta T}\right) \tag{1.9}$$

G_0 is the constant that hardly depends on temperature, R is the gas constant, and $K = 4b_s\sigma_e\sigma {T_m}^0/k_B\Delta H$. k_B is the Boltzmann constant. This theory successfully describes the crystal growth rate of most polymer species. ΔE in Eq. (1.9) is associated with the inhomogeneity of entanglements and stress field. Since the crystalline lattice structures

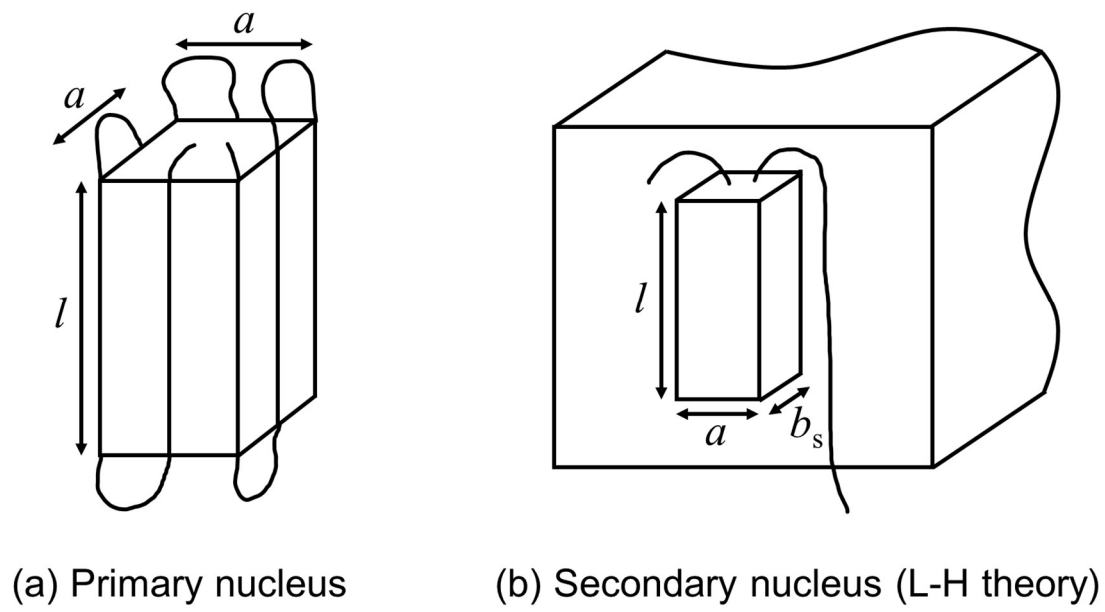

Figure 1.2 Models of (a) primary and (b) secondary nucleation. The nucleus consists of a length l, a width a, and a stem thickness b_s,

cannot include the entanglements, their spatial inhomogeneity increases with the progress of crystallization. In the case of a high-entropy phase such as a hexagonal phase, the chains can slide within the lattice along the chain direction, eliminating the inhomogeneity of entanglements and stress field in the amorphous regions.[5,6]

In the formation of the lamellar branching structures, the spatial inhomogeneity of the stress field leads to the instability at the growth front and lamellar branching. I describe the mechanism of lamellar branching, which has been recently proposed by Toda et al.[7,8]

When the lamellae at the growth front reaches a critical width λ^*, it destabilizes and splits into two branches. This is dynamically coupled with the reorientation due to inherent torsional stress. This coupling induces the independent growth of each branch. As each branch grows and reaches λ^*, it again branches and reorients. This process

repeatedly occurs. Figure 1.3 shows the schematic illustration of this concept. The origin of the inherent torsional stress is considered to be the stress on the upper and lower surfaces of the lamellae due to the congestion of chain folds, cilia, and tie chains.[8,9]

It has been pointed out for many years that the gradient of the chemical potential on the liquid side of the growth surface causes the instability.[11-13] The fluctuation of the growth front increases because more driving force for crystallization is generated farther from the growth front. Figure 1.4 shows the schematic illustration. Toda et al. proved that this gradient originates from the pressure field, or the difference in the density between crystal and amorphous phases. In other words, the nature of lamellar branching is considered to be the same as viscous fingering (Saffman-Taylor instability)[14,15] observed in dynamically asymmetric systems.

Let us consider a lamellar crystal as an x-y plane, with the y-axis in the growth direction and the x-axis perpendicular to the growth direction. Then, the shape of the interface at the growth front can be defined as $y(x) = y_0 + A_{\mathrm{gf}}\cos(q_{\mathrm{gf}}x)$ using the amplitude and wavenumber of the fluctuation, A_{gf} and q_{gf}, respectively. y_0 is the mean position. This fluctuation is stabilized by the surface tension σ.[12] Considering these contributions, the driving force for crystallization at the growth front, or the difference in chemical potential per segment $\Delta\mu$, can be expressed as[7,8]

$$\begin{aligned}\Delta\mu &\cong \Delta\mu_0 + a_{\mathrm{g}}(y - y_0) + v_{\mathrm{c}}\sigma\frac{\mathrm{d}^2 y}{\mathrm{d}x^2} \\ &= \Delta\mu_0 + \left(a_{\mathrm{g}} - v_{\mathrm{c}}\sigma {q_{\mathrm{gf}}}^2\right)A_{\mathrm{gf}}\cos\left(q_{\mathrm{gf}}x\right)\end{aligned} \tag{1.10}$$

where $\Delta\mu_0$ is $\Delta\mu$ at the mean position, a_{g} is the gradient, and v_{c} is the specific volume of the segment in the crystalline phase. When $a - v_{\mathrm{c}}\sigma {q_{\mathrm{gf}}}^2 > 0$, the fluctuation accelerates

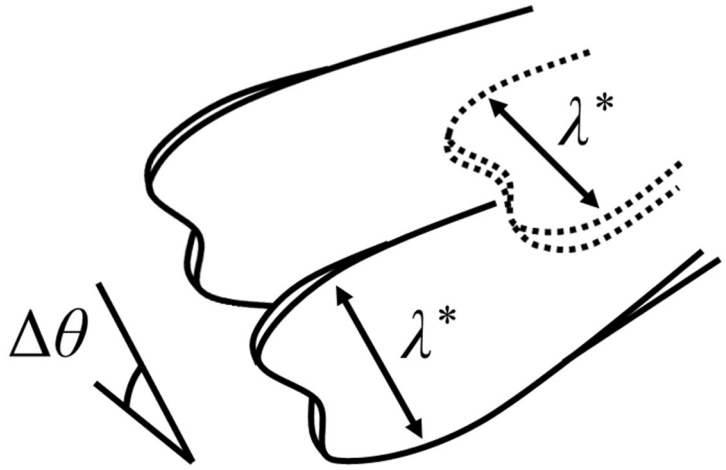

Figure 1.3 Schematic illustration of dynamic coupling between lamellar branching and reorientation. λ^* and $\Delta\theta$ denote the critical lamellar width and the angle of reorientation, respectively.

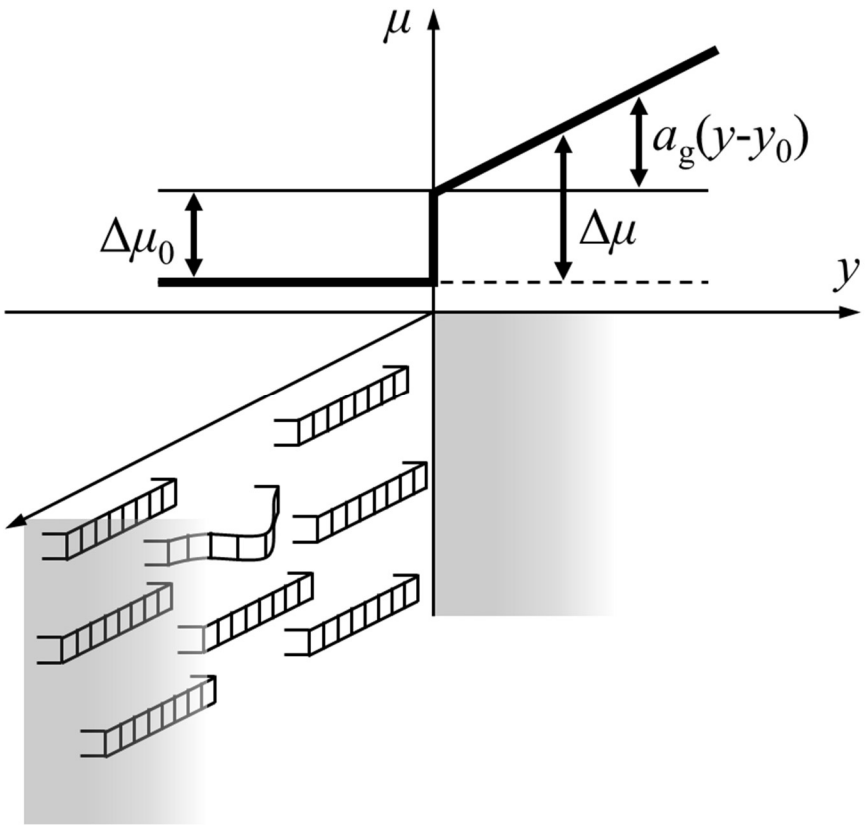

Figure 1.4 Schematic illustration of the gradient field spontaneously formed at the growth front and the change in the chemical potential due to the gradient.

and lamellar branching occurs. Therefore, the critical width is obtained as

$$\lambda^* = 2\pi \left(\frac{v_c \sigma}{a_g} \right)^{1/2} \tag{1.11}$$

Using Clausius-Clapeyron relation of the melting line, a_g can be expressed as

$$a_g = \frac{\Delta H_s}{T_m} \frac{\partial(\Delta T)}{\partial y} = \frac{\Delta H_s}{T_m} \left(\frac{\Delta v}{\Delta S_s} \frac{\partial p}{\partial y} \right) = \Delta v \frac{\partial p}{\partial y} \tag{1.12}$$

where p is the pressure, Δv is the difference in the density between crystalline and amorphous phases, and ΔH_s and ΔS_s are the enthalpy and entropy of fusion per segment, respectively.

The pressure gradient in the fluid of viscosity η causes the shear flow of thickness b_f with the flow rate u, which balances the difference in the density, as[8]

$$\frac{\partial p}{\partial y} = \frac{12\eta}{{b_f}^2} u = \frac{12\eta}{{b_f}^2} \frac{\Delta v}{v_c} G \tag{1.13}$$

From Eqs. (1.11)–(1.13), the critical lamellar width is obtained as

$$\lambda^* = 2\pi b_f \frac{v_c}{\Delta v} \left(\frac{\sigma}{12 G \eta} \right)^{1/2} \tag{1.14}$$

This equation shows that the lower viscosity of the matrix region makes the interface more stable and the lamellar width larger, similar to viscous fingering. In summary, the stress field in the melts should determine the morphology of the lamellar branching

structures. However, the effects of the stress field have not been clarified.

1.3 Effect of Stress Field on Self-Assembling Process under Deformation

The spatial inhomogeneity of the stress field also affects the structural changes in crystalline polymers during the deformation process. The crystalline lattice structures and lamellar structures under deformation has been well investigated. Crystalline polymers exhibit one or two yield points on the stress-strain curve under tensile tests. The origin of the yielding behaviors has been discussed mainly using SAXS and WAXS. Researchers have found that the yielding behaviors originate from so-called "slip" behaviors on the nm scale, or the scale of the lamellar structures.[2,16,17] The slips are categorized as interlamellar slip and intralamellar slip. During interlamellar slip, only amorphous regions in the lamellar structures are deformed by stretching, and the slip deformation between crystalline regions occurs. Intralamellar slip is further categorized as fine slip and coarse slip. Coarse slip describes the fragmentation of the crystalline regions into mosaic blocks. Fine slip corresponds to homogeneous block shearing, which leads to transformation into a metastable phase, or monoclinic phase. The intralamellar slip facilitates the chains in the crystalline regions becoming oriented parallel to the stretching direction in contrast to interlamellar slip. Figure 1.5 shows the schematic illustration of these slipping processes.

On the other hand, the effect of the spatial inhomogeneity of the stress field due to the lamellar branching structures has not been clarified. Recently, however, USAXS has been established to observe submicron-scale structures, and has enabled us to observe

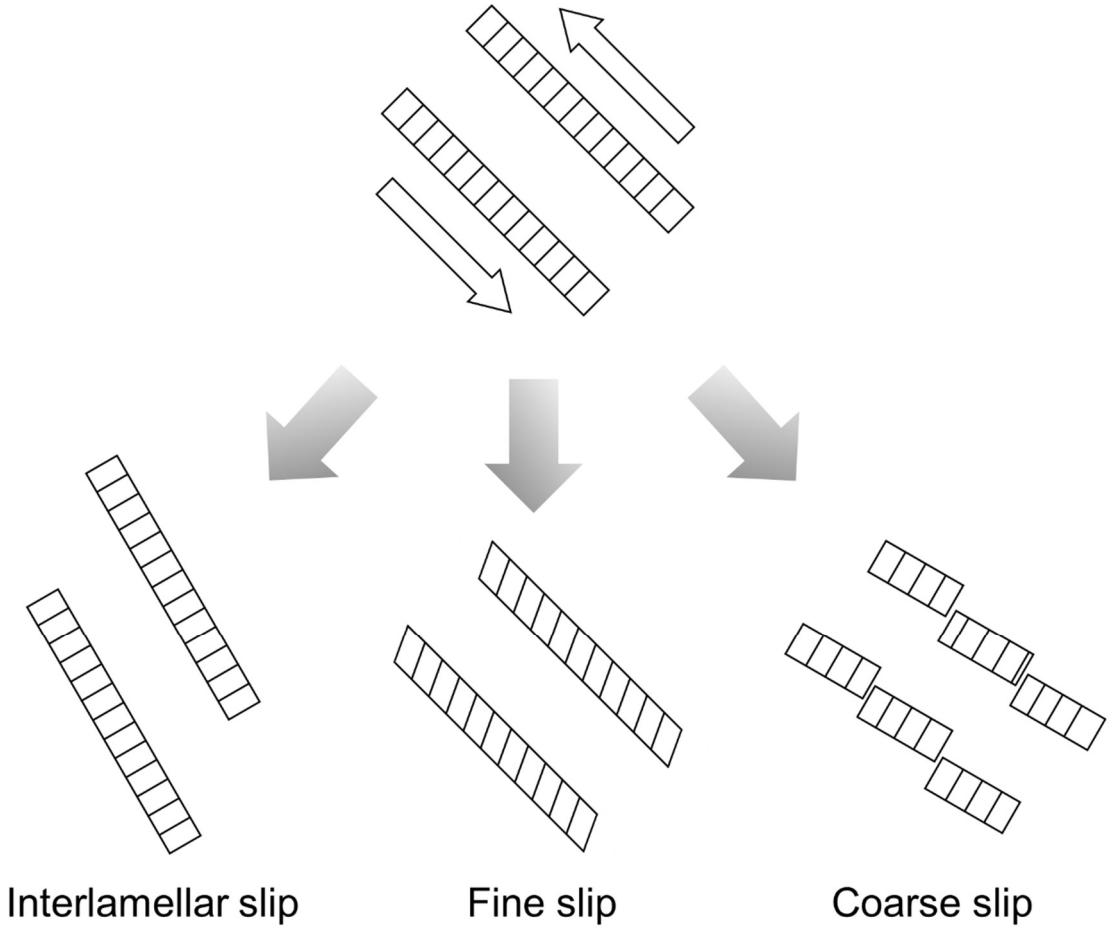

Figure 1.5 Representative slipping processes in the lamellar structures during uniaxial stretching.

changes in the lamellar branching structures.[18] Takenaka et al. observed a butterfly pattern in PE by USAXS, where the intensity increased in the direction parallel to the stretching direction around the yield point.[19] The butterfly pattern is also observed by small-angle neutron scattering (SANS) on gels under deformation[20] and LS on semidilute solutions under simple shear.[21] The butterfly pattern characterizes coupling between the concentration fluctuation and the stress originating from the dynamic asymmetry between polymer and solvent, which Doi and Onuki theoretically proved.[22] Later, Furukawa and Tanaka theoretically proved that coupling between the density fluctuation and the stress

can lead to mechanical instability, even if a single-component material such as glass is deformed at a rate slower than the glass transition.[23,24] We can expect that the theory can describe the strain-induced density fluctuations in the crystalline polymer. I briefly describe this theory below.

The essence of this theory is that the density dependence of viscosity is explicitly considered in the Navier-Stokes equation for compressible fluids. the density $\rho(\mathbf{r},t)$ at position **r** and time *t* obeys the continuity equation:

$$\frac{\partial}{\partial t}\rho = -\nabla\cdot(\rho\mathbf{v}) \tag{1.15}$$

where **v** is the velocity field. The velocity field obeys the Navier-Stokes equation:

$$\rho\left(\frac{\partial}{\partial t}+\mathbf{v}\cdot\nabla\right)\mathbf{v} = -\nabla\cdot\overleftrightarrow{\Pi}+\nabla\cdot\overleftrightarrow{\sigma} \tag{1.16}$$

where $\overleftrightarrow{\Pi}$ and $\overleftrightarrow{\sigma}$ are the pressure tensor and the viscous stress tensor, respectively. The linearized equation of motion for the volume dilation rate $Z = \nabla\cdot\mathbf{v}$ under uniaxial stretching is derived in the Fourier representation in **q** space as[24]

$$\begin{aligned}\rho_0\frac{\partial Z_{\mathbf{q}}}{\partial t} &- \frac{\dot{\varepsilon}}{2}\left(q_z\frac{\partial}{\partial q_z}Z_{\mathbf{q}} - q_x\frac{\partial}{\partial q_x}Z_{\mathbf{q}}\right) + i\dot{\varepsilon}\left(q_z v_{z\mathbf{q}} - q_x v_{x\mathbf{q}}\right)\\ &= -\left(\frac{2d-2}{d}\eta_0+\zeta_0\right)q^2 Z_{\mathbf{q}} + \frac{1}{K_T\rho_0}q^2\rho_{\mathbf{q}} - \left(\frac{\partial\eta}{\partial\rho}\right)\dot{\varepsilon}({q_z}^2-{q_x}^2)\rho_{\mathbf{q}}\end{aligned} \tag{1.17}$$

where ρ_0, η, d, $\dot{\varepsilon}$, and K_T are the spatially averaged density, viscosity, spatial dimension, strain rate, and isothermal compressibility, respectively. η_0 and ζ_0 are η and the bulk

viscosity at ρ_0, respectively. The second term on the right-hand side suppresses the density fluctuation, while the third term on the right-hand side increases the density fluctuation. Considering the balance of them, the critical strain rate $\dot{\varepsilon}_c$ is obtained as

$$\dot{\varepsilon}_c = \left(\frac{\partial \eta}{\partial p}\right)_T^{-1} \tag{1.18}$$

In the case of high-viscosity fluids such as polymer materials, $\dot{\varepsilon}_c$ is small enough to be evaluated experimentally because their viscosity strongly depends on the density. In contrast, in the case of low-viscosity fluids such as water under normal temperature and pressure, an extremely large $\dot{\varepsilon}_c$ is required. In such a case, instability due to turbulence or other mechanisms, which is different from the present theory, is considered to dominate the cavitation.

The interpretation of the butterfly pattern found in PE is that the stress field dynamically coupled with the density fluctuations, or the crystallinity fluctuations, on the scale of the lamellar branching structures induces the enhancement in the density fluctuations. However, there have been no in-situ observations of the evolution of density fluctuations in crystalline polymers. Thus, it has not been clarified how the strain-induced density fluctuations affect the mechanical properties and are affected by the primary structures.

1.4 Motivation and Outline of This Thesis

Polymer materials experience a process from molding (crystallization) to practical use or mechanical testing (fracture). As described above, it has recently been

proposed that the stress field might have the significant effects on these processes. In this thesis, I investigated the role of the stress field using PE, which has the simplest primary structure among polyolefins, comparing its results with those of several different polyolefins as appropriate.

In Chapter 2, I studied the effect of the viscosity of the melts on the morphology during crystallization. The morphology of poly(3-methylbutene-1) (P3MB1), which has very high melting temperature (T_m^0 = 323°C), was compared with that of PE, whose thermodynamic parameters are already known. P3MB1 has not been industrialized so far and is expected to be a new polymer material with high heat resistance. I demonstrate that the stress field can determine the morphology of the lamellar branching.

In Chapter 3, I attempted to clarify the spatial distribution of the dynamic inhomogeneity in a crystalline polyolefin after crystallization by focusing on the difference in solvent swelling properties due to the difference in mobility. I used ethylene-octene copolymer (EOC), which is also called as very low-density PE (VLDPE).[1] Such a low crystallinity polymer makes it easier to evaluate the spatial correlation between the crystallites and rigid amorphous regions. Contrast variation SAXS (CV-SAXS) using two solvent mixtures with equivalent interactions with EOC and pulsed proton nuclear magnetic resonance (^{1}H-NMR) revealed the presence of the rigid amorphous regions surrounding the crystallites.

In Chapter 4, I investigated the changes in the hierarchical structures of high-density PE (HDPE) and linear low-density PE (LLDPE) under uniaxial stretching by means of time-resolved USAXS, SAXS, and WAXS. I observed butterfly patterns in USAXS for both samples, and found the correlation between the enhancement of the density fluctuations and the generation of voids. In other words, the dynamic asymmetry

on the submicron (lamellar branching) scale dominates the mechanical properties of PE.

In Chapter 5, in order to investigate the factors governing the strain-induced density fluctuations (SIDF) in PE, I observed the changes in the hierarchical structures of LLDPE with different comonomer species and contents, using the same method as in Chapter 4. I performed detailed analyses, focusing on the density fluctuations on the submicron scale before stretching and mechanical melting during stretching.

In Chapter 6, I conducted to visualize the SIDF and the spatial inhomogeneity of chain orientation in PE by means of scanning transmission X-ray microscopy (STXM). It is expected that stretching induces not only the enhancement of the density fluctuations but also the orientation fluctuations. I attempted the real-space observation of the SIDF and the accompanying orientation fluctuations by STXM of the stretched specimen.

References

1. Vasile, C., *Handbook of polyolefins*. CRC Press: 2000.
2. Kishimoto, M.; Mita, K.; Ogawa, H.; Takenaka, M., *Macromolecules* **2020,** *53*, 9097-9107.
3. Okui, N., Crystallization of Polymers. Kyoritsu Shuppan **2012**.
4. Lauritzen, J. I. Jr.; Hoffman, J. D., *J. Appl. Phys.* **1973**, *44*, 4340-4352.
5. Hikosaka, M.; Watanabe, K.; Okada, K.; Yamazaki, S., *Adv. Polym. Sci.* **2005**, *191*, 137-186.
6. Strobl, G., The Physics of Polymers. Springer-Verlag Berlin Heidelberg **2007**.
7. Toda, A.; Okamura, M.; Taguchi, K.; Hikosaka, M.; Kajioka, H., *Macromolecules* **2008,** *41*, 2484-2493.
8. Toda, A.; Taguchi, K.; Kajioka, H., *Macromolecules* **2008,** *41*, 7505-7512.
9. Lotz, B.; Cheng, S. Z. D., *Polymer* **2005,** *46*, 577-610.
10. Bassett, D. C.; Olley, R. H., *Polymer* **1984,** *25*, 935-943.
11. Keith, H. D., *J. Appl. Phys.* **1963,** *34*, 2409-2421.
12. Goldenfeld, N., *J. Cryst. Growth* **1987,** *84*, 601-608.
13. Schultz, J. M., *Polymer* **2003,** *44*, 433-441.
14. Saffman, P. G.; Taylor, G. I., *Proc. R. Soc. London, Ser. A.* **1958,** *245*, 312-329.
15. Fields, R. J.; Ashby, M. F., *Philos. Mag.* **1976,** *33*, 33-48.
16. Bowden, P. B.; Young, R. J., *J. Mat. Sci.*. **1974,** *9*, 2034-2051.
17. Butler, M. F.; Donald, A. M.; Ryan, A. J., *Polymer* **1998,** *39*, 39-52.
18. Yagi, N.; Inoue, K., *J. Appl. Crystallogr.* **2003,** *36*, 783-786.
19. Takenaka, M.; Shimizu, H.; Nishitsuji, S., *Phys. Rev. E* **2007,** *75*, 061802.
20. Bastide, J.; Leibler, L.; Prost, J., *Macromolecules* **1990,** *23*, 1821-1825.
21. Kume, T.; Hattori, T.; Hashimoto, T., *Macromolecules* **1997,** *30*, 427-434.

22. Doi, M.; Onuki, A., *J. Phys. II* **1992,** *2*, 1631-1656.

23. Furukawa, A.; Tanaka, H., *Nature* **2006,** *443*, 434-438.

24. Furukawa, A.; Tanaka, H., *Nat. Mat.* **2009,** *8*, 601-609.

Chapter 2
Effect of Stress Field on Lamellar Branching during Isothermal Crystallization

2.1 Introduction

One of the most important parameters of polyolefins is their melting temperature (T_m), which depends on their monomer structures. For example, the melting temperatures of polyethylene (PE) and isotactic polypropylene (iPP) are approximately 120 °C and 160 °C, respectively; further, polyolefins show relatively poor heat resistance. Though isotactic poly(4-methylpentene-1) (P4MP1) has a high T_m (~ 240 °C[1-3]) and shows relatively high heat resistance among commercially available polyolefins, polyolefins with higher heat resistance are required. Isotactic poly(3-methylbutene-1) (P3MB1) has a higher T_m (~ 305 °C[4,5]) than P4MP1 and is thus expected to be a new polymer material with high heat resistance. The chemical structure of P3MB1 is shown in Figure 2.1(c). However, P3MB1 is very brittle, and for practical use, its mechanical properties need to be improved by controlling the morphologies. Hence, it is very important to understand the formation process of the crystalline structure of P3MB1. There are no studies on the isothermal crystallization of P3MB1, although there are studies regarding the crystal lattice[6-8] or the softening point.[4,5]

In this chapter, the changes in morphologies of P3MB1 during isothermal crystallization were investigated and discussed in conjunction with the measured thermodynamic parameters, such as the enthalpy of fusion, thickness and surface free

energy of lamellae, to understand the effect of the high T_m of P3MB1 on the crystallization dynamics. Since crystalline polymers form hierarchical structures over a wide spatial scale, it is necessary to employ various techniques to observe the hierarchical structures. For in-situ observations over a wide spatial scale from 0.1 nm to several μm, optical microscopy (OM), small-angle X-ray scattering (SAXS), and wide-angle X-ray scattering (WAXS) measurements using synchrotron radiation were conducted. Fast scanning calorimetry (FSC) and pressure-volume-temperature (PVT) measurements were also conducted to evaluate the thermodynamic parameters of P3MB1.

2.2 Experimental Section

2.2.1 Sample Preparation

P3MB1 powder was polymerized with conventional Ziegler-Natta catalysts. The P3MB1 powder was vacuum-pressed above T_m and quenched by cold pressing at room temperature, to obtain a film specimen of thickness 0.5 mm. I performed differential scanning calorimetry (DSC) measurements at a heating rate of 10 °C/min, and determined the T_m and the glass transition temperature (T_g) of P3MB1 to be 304 °C and 51 °C, respectively, which agree with the values reported previously[5,9].

2.2.2 FSC Measurements

FSC measurements were performed with a Flash DSC (METTLER TOREDO) system. A 10 μm-thin film was cut out from the P3MB1 film specimen. The film was placed on a chip sensor and pre-melted at 340 °C for 1 s to ensure good adhesion to the sensor. Measurements were carried out as follows: First, the sample was held at 340 °C for 0.1 s, and quenched to the pre-set crystallization temperature (T_c) at a cooling rate of

4000 °C/s. After isothermal crystallization for 1 min, the sample was heated at the pre-set rate and the heat flow was recorded. T_c was set to a range of 220 to 295 °C, and the heating rate (β_H) was set to a range of 10 to 5000 °C/s.

2.2.3 OM Observations

The isothermal crystallization dynamics of P3MB1 was investigated at various T_c (297, 290 and 275 °C) after being quenched from the melt at T_i (348 °C). BX50 (Olympus) was used for OM. A piece of the film specimen was pressed to a thickness of 50 μm and sandwiched between two cover glasses to obtain a sample for the OM observations. Quench was attained as follows: First, the sample was set on the heater stage at T_i (heater stage I). After maintaining the sample for 5 min at T_i to erase the thermal history, it was slid from heater stage I to another heater stage at T_c (heater stage II). Subsequently, isothermal crystallization was observed. When the transfer was completed, the time (t) was set to zero.

2.2.4 Simultaneous SAXS and WAXS Measurements

Simultaneous synchrotron radiation SAXS and WAXS measurements were carried out under the same crystallization conditions as for the OM observation using the beamline BL03XU at SPring-8, Hyogo, Japan.[10] The wavelength of the incident X-rays was 0.1 nm. For the SAXS and WAXS measurements at T_c = 297 °C, a charge-coupled device camera with an image intensifier and a flat panel detector were used as detectors, the sample-to-detector distances were 2461 mm and 64 mm, and the exposure times were 100 ms and 330 ms, respectively; the scattering images were acquired every second. For the SAXS and WAXS measurements at T_c = 290 and 275 °C, Pilatus 1M (DECTRIS) and

a flat panel detector were used as detectors, the sample-to-detector distances were 2421 mm and 68 mm, and the exposure times were 670 ms and 670 ms, respectively; the scattering images were acquired every second. Quench was attained as follows: First, the specimens filled in sample cells with 12.5 μm-thick Kapton windows were set in a heater block at T_i (heater block I). After maintaining the samples for 5 min at T_i, the cell was transferred to another heater block (heater block II) set to T_c. When the transfer was completed, t was set to zero, as in the OM observations.

2.2.5 Parameter Collection for Determining Δ*H* of P3MB1

In addition, to calculate the enthalpy of fusion, another WAXS measurement was performed. The P3MB1 film was placed in the abovementioned sample cell for the X-ray scattering experiment, and the WAXS measurements were performed in the range of 200–280 °C with NANO-Viewer (RIGAKU) and another heater block. PILATUS 10K (DECTRIS) was used as a detector. The wavelength of the incident X-rays was 0.154 nm. The sample-to-detector distance was 91 mm, and the exposure time was 20 min.

The zero-shear viscosity (η) at 310 °C was measured by a rheometer, ARES (TA Instruments). The strain was 5% and the angular frequency was 0.1 to 500 rad/s.

PVT measurements were performed with the GNOMIX apparatus. A few pieces of the P3MB1 film were vacuum-dried at 80 °C for 4 h and then sealed in the sample cell. The change in the specific volume during isobaric heating was recorded. The pressure was set to a range of 20 to 100 MPa, and the heating rate was 4 °C/min. The temperature dependence of the specific volume at 0 MPa was calculated from the results of the isothermal measurement in the range of 10–30 MPa.

2.3 Results and Discussion

2.3.1 Determination of T_m^0 of P3MB1 by FSC Measurement

I estimated the equilibrium melting temperature (T_m^0) by using the Hoffman-Weeks (H-W) plot[11] with the FSC measurements[12,13]. In the H-W plots, the intersection between $T_m = T_c$ and the linear line extrapolated from the plots of $T_m(T_c)$ vs T_c corresponds to T_m^0, where $T_m(T_c)$ is the melting temperature of the crystals crystallized at T_c. $T_m(T_c)$ can be estimated by measuring the β_H dependence of T_m during quick melting processes from the crystals crystallized at T_c, with the FSC measurements. It should be noted that slow cooling induces crystallization during the cooling processes with conventional DSC measurements; therefore, we cannot obtain the crystals crystallized at T_c and estimate $T_m(T_c)$ correctly with slow cooling. Figure 2.1(a) shows the β_H dependence of the heat flow during heating processes in the P3MB1 samples crystallized at T_c = 280 °C. The peaks corresponding to T_m can be observed in each curve. As β_H decreases, the peak temperature T_p shifts to a lower temperature. I also measured the β_H dependence of the heat flow for the P3MB1 samples crystallized at T_c = 283–295 °C. At T_c < 280 °C, the crystallization occurred during quenching; hence, $T_m(T_c)$ could not be evaluated accurately. Figure 2.1(b) shows the β_H dependence of $T_p(T_c)$ for various T_c. According to Toda et al.[14], the β_H dependence of $T_p(T_c)$ for T_c is expressed by

$$T_p(T_c) = T_m(T_c) + A_f \beta_H{}^z \tag{2.1}$$

where A_f and z are constants. The solid lines are the fitting results with Eq. (2.1), showing that Eq. (2.1) can express the experimental results and $T_m(T_c)$ for 280–295 °C can be estimated. Figure 2.1(c) shows the H-W plot or $T_m(T_c)$ as a function of T_c. The plot shows

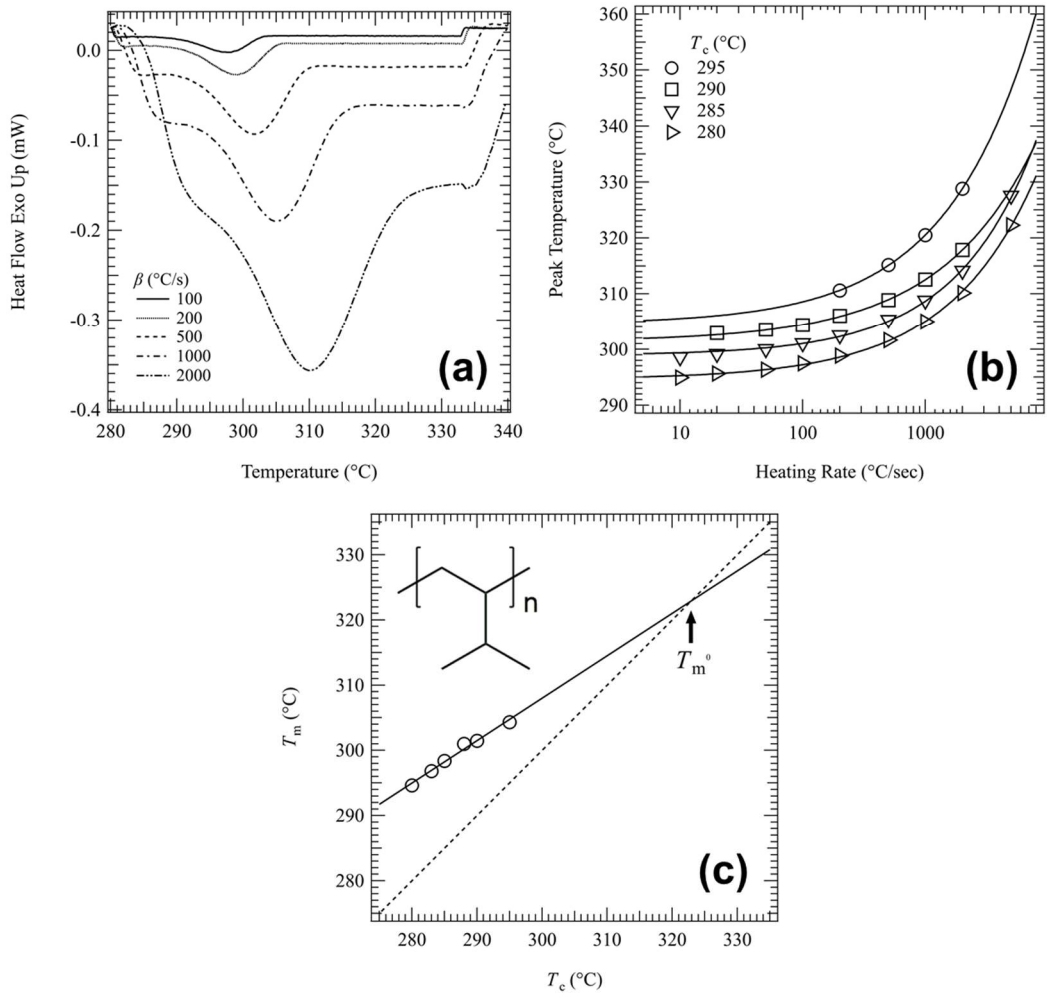

Figure 2.1 (a) Melting behaviors of P3MB1 after isothermal crystallization at T_c = 280 °C measured by FSC. (b) β_H dependence of melting peak temperatures for P3MB1 crystallized at various T_c. The solid lines are the fitting curves expressed by Eq. (2.1). (c) Hoffman-Weeks plots for P3MB1. T_m^0 = 322.9 °C.

a linear relationship, and T_m^0 (= 322.9 °C) is obtained from the intersection between the line of $T_m = T_c$ and the linear line extrapolated from the plot of $T_m(T_c)$ vs T_c.

2.3.2 OM Observation during Isothermal Crystallization

The OM images at each T_c are shown in Figure 2.2. The OM images at T_c = 275 °C were observed under the crossed Nicols condition. In contrast, I observed

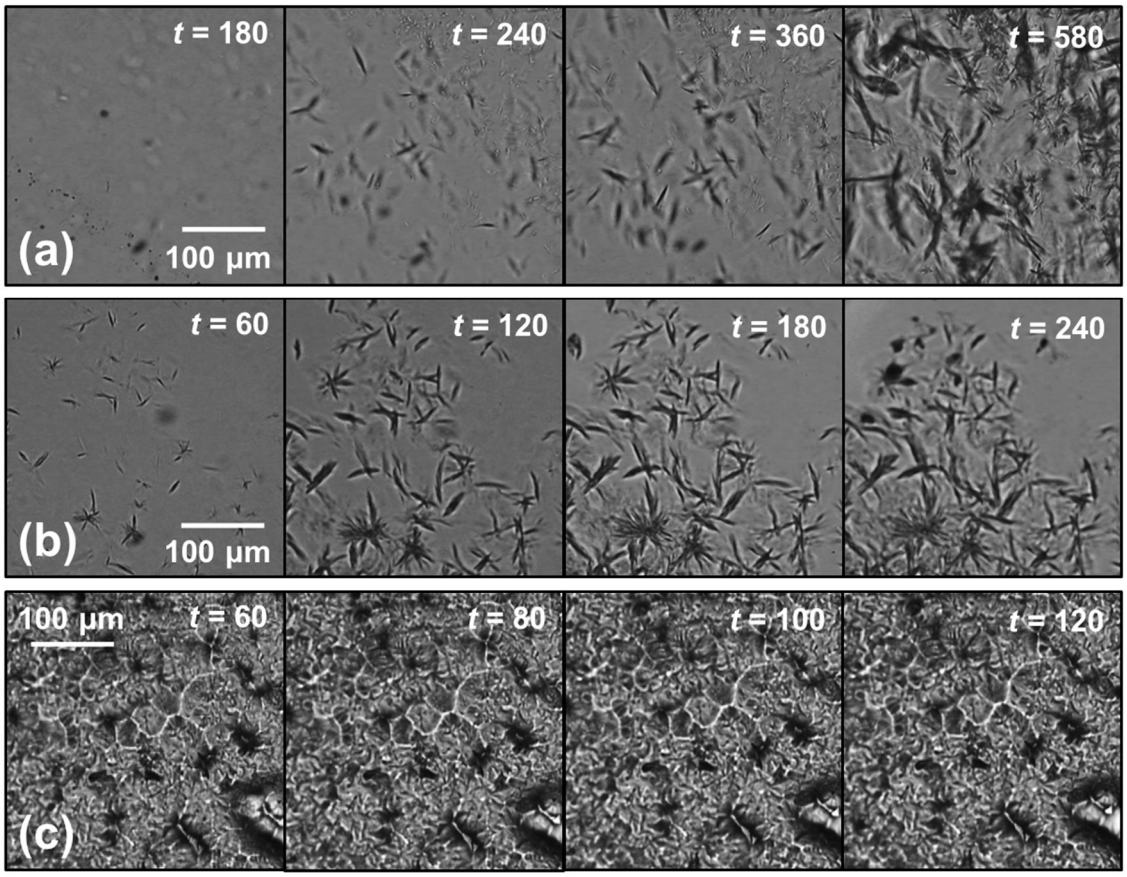

Figure 2.2 Representative OM images at T_c = (a) 297 °C, (b) 290 °C, and (c) 275 °C. (c) was obtained under the crossed Nicols condition.

the OM images under the parallel Nicols conditions at T_c = 290 and 297 °C, because I could not obtain enough contrast under the crossed Nicols condition. As shown in Figure 2.2(a), needle-like crystals developed during the isothermal crystallization at T_c = 297 °C. At t = 580 s, the longitudinal size of the crystals reached 100 μm. This morphology is quite different from that of the spherulites commonly observed in PE. In addition, the needle-like crystals flow in the melts.

At T_c = 290 °C, the needle-like crystals and axialites coexisted (Figure 2.2(b)). The change in morphology was not observed after t = 40 s. The needle-like crystals flow while the axialites appear not to flow in the melts. I could not observe the needle-like

crystals and the axialites clearly under the crossed Nicols condition. These crystals are considered thinner than spherulites, and hence cannot make sufficient retardation.

At T_c = 275 °C, isotropic crystals grew immediately after quenching and collided with each other, following which the growth stopped (Figure 2.2(c)). I could not distinguish whether these crystals were in the form of spherulites or axialites. Kirshenbaum et al. observed spherulites of P3MB1 more clearly by slow cooling.[5] The OM observations at T_c = 275–297 °C indicate that as T_c increased, the number of lamellar branches decreased, and the spherulites changed to needle-like crystals via axialites.

2.3.3 SAXS and WAXS Measurements during Isothermal Crystallization

Figure 2.3 shows the scattering patterns obtained by time-resolved SAXS and WAXS measurements at each T_c, and Figure 2.4 shows the circular averaged profiles corresponding to the pattern. Here, q is the magnitude of the scattering vector defined by $q = (4\pi/\lambda_{X\text{-ray}})\sin(\theta/2)$, where $\lambda_{X\text{-ray}}$ and θ are the wavelength of the incident X-rays and the scattering angles, respectively. As seen in the SAXS patterns at 297 °C (left side of Figure 2.3(a)), peaks from the long spacing of the stacked lamellae were observed, except at t = 240 s, and the patterns possessed anisotropy even though the crystallization occurred in the static field. In the WAXS patterns, anisotropic patterns with multiple diffracted spots in the azimuthal direction were observed (right side of Figure 2.3(a)). As seen in the representative profiles, peaks from the long spacing were observed up to the second order in SAXS (Figure 2.4(a)), whereas in WAXS, the diffraction peaks attributed to monoclinic crystals were observed, and no other crystal systems were obtained (Figure 2.4(b)). To clarify the change in lamellar structures, I fitted the series of SAXS profiles around the primary peak with Eq. (2.2):

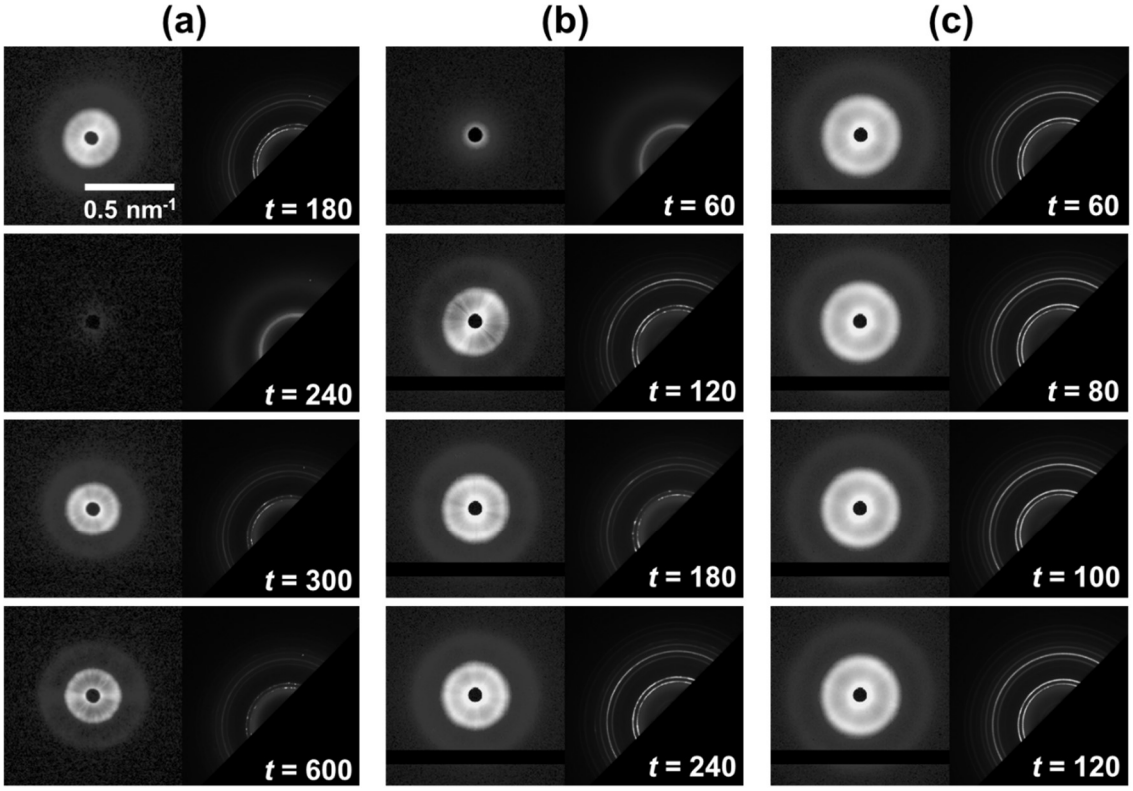

Figure 2.3 Representative SAXS and WAXS patterns at T_c = (a) 297 °C, (b) 290 °C, and (c) 275 °C. The left side of each set shows the SAXS patterns. The black lines at the bottom of the SAXS patterns of (b) and (c) represent the gap between the detector modules.

$$I(q) = I_s q^{-n_s} + I_{ls} \exp\left[-\frac{(q - x_{ls})^2}{w_{ls}}\right] \tag{2.2}$$

Eq. (2.2) is a linear combination of the power law and the Gaussian function, where I_{ls}, x_{ls}, and w_{ls} are the peak intensity, position and width, respectively. I also fitted the series of WAXS profiles at q < 8 nm^{-1} with Eq. (2.3). Equation (2.3) is a linear combination of three Gaussian functions and a constant I_{base}; the first term is the amorphous contribution, whereas the second and third terms are the contributions from the lattice planes

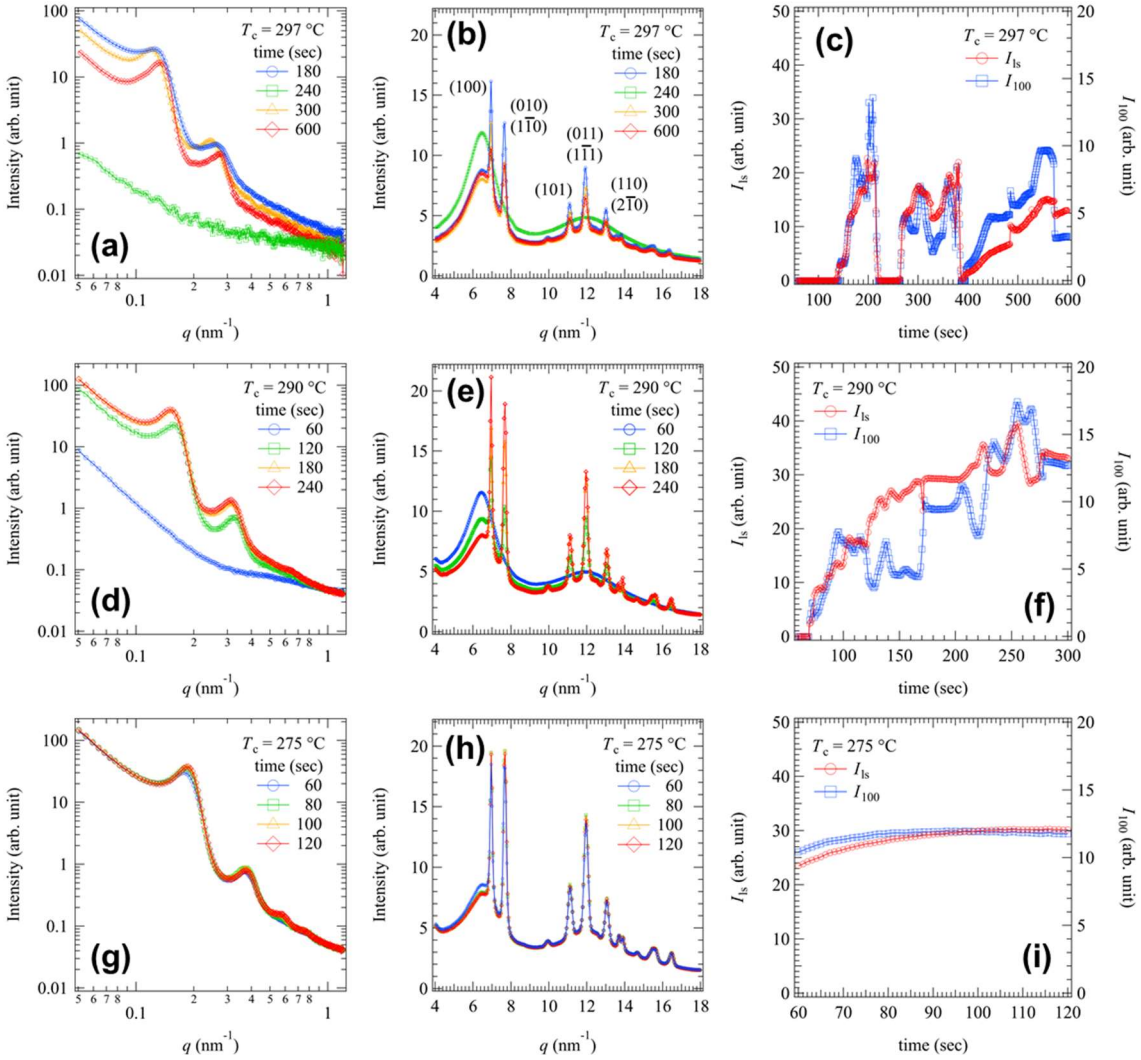

Figure 2.4 Representative SAXS profiles at T_c = (a) 297 °C, (d) 290 °C, and (g) 275 °C; WAXS profiles at T_c = (b) 297 °C, (e) 290 °C, and (h) 275 °C; time evolutions of the peak intensities I_{ls} and I_{100} defined in Eqs. (2.2) and (2.3) at T_c = (c) 297 °C, (f) 290 °C, and (i) 275 °C.

corresponding to the subscripts.

$$I(q) = I_{\mathrm{am}}\exp\left[-\frac{(q-x_{\mathrm{am}})^2}{w_{\mathrm{am}}}\right] + I_{100}\exp\left[-\frac{(q-x_{100})^2}{w_{100}}\right] + I_{010,1\bar{1}0}\exp\left[-\frac{(q-x_{010,1\bar{1}0})^2}{w_{010,1\bar{1}0}}\right] + I_{\mathrm{base}} \tag{2.3}$$

The lattice spacings of (010) and $(1\bar{1}0)$ are mutually too close to distinguish on the profiles. Figure 2.4(c) shows the time evolutions of the peak intensities, I_{ls} and I_{100}, which repeatedly increase and decrease irregularly with time. At t = 240 s, no signals from the crystals were detected in either SAXS or WAXS. This fluctuation in the peak intensities suggests that the amount of the crystalline region in the irradiated area (120 μm × 80 μm) of the incident X-ray beam changes irregularly with time due to the flow of the crystalline structures in the melt. This also indicates that the crystallization kinetics of P3MB1 cannot be discussed with the time-resolved X-ray scattering data. A similar tendency can be observed at T_c = 290 °C. The anisotropic SAXS and WAXS patterns can be seen at T_c = 290 °C (Figure 2.3(b)). The time evolutions of the peak intensities (Figure 2.4(f)) increase in the SAXS and WAXS profiles with fluctuations. In the case of T_c = 275 °C, the isotropic SAXS and WAXS patterns were well developed even at t = 60 s, and a slight increase in the intensities was observed thereafter (Figure 2.3(c)). The time evolutions of the peak intensities also show that the changes in the intensities after t = 60 s were very small.

Furthermore, in the changes in the SAXS and WAXS profiles with time at T_c = 297 °C, since the moments of the appearance/disappearance of the long spacings and the diffraction peaks were synchronized, a lamella stack was found in the needle-like crystals. The needle-like crystals reported thus far have been limited to single crystals, and those with stacked lamellae have not yet been discovered, to the best of my knowledge. In polyolefins, PE and P4MP1 form extended-chain single crystals under high pressures.[15,16] Such single crystals consist of hexagonal crystal lattices, with thicknesses on the order of micrometers. Moreover, PP forms giant single crystals via the meso phase.[17] As mentioned above, hexagonal crystals of P3MB1 were not observed in the present WAXS measurements. If the needle-like crystals in P3MB1 were single crystals, then the

lamellae composed of monoclinic crystal lattices would have a thickness on the order of micrometers. In that case, $T_m \simeq T_m^0$ and especially at $T_c > 290$ °C, two melting peaks should be obtained in the thermal analysis, since the single crystals coexist with the lamellae with a thickness of tens of nanometers. However, in the series of FSC measurements mentioned above, the melting peak was always unimodal at T_c = 280–295 °C, and T_m continued to increase as T_c increased, as shown in the H-W plots (Figure 2.1(c)). This indicates that the needle-like crystals of P3MB1 are not single crystals but are composed of stacked lamellae, which are nanometer-thick folded chain crystals.

2.3.4 Growth of Needle-Like Crystals in P3MB1

As shown in the previous section, needle-like crystals are formed in P3MB1 in the wide ΔT region. It was reported that the number of lamellar branches decreases as T_c increases in PE and isotactic poly(butene-1) (PB1).[18,19] Granasy et al. have reported a morphological transition from spherulites to needle-like crystals with a decrease in supersaturation by computer simulation.[20] In addition, in the high T_c region, PE is reported to often form axialites with a regime transition (II → I).[21,22] Regime I and II represent the single- and multi-nucleation growth, respectively. However, the region of the axialites of PE is much narrower than that of P3MB1.

I examined why P3MB1 has less lamellar branches than PE. One reason may be the morphological instability caused by the gradient of the chemical potential spontaneously generated at the growth front as described in Chapter 1.[18,19,23] In their model, decreasing branches and increasing lamellar widths were synonymous. The critical lamellar width λ^* under a pressure field can be expressed as

$$\lambda^* = 2\pi b_f \frac{v_c}{\Delta v}\left(\frac{\sigma}{12G\eta}\right)^{\frac{1}{2}} \quad (2.4)$$

where b_f, v_c, Δv, σ, G and η are the thickness of the shear flow induced by the gradient field, specific volume of the crystal, difference between the specific volume of the crystal and the melt, surface free energy of the growth front, crystal growth rate and viscosity at T_c, respectively. It is known that b_f is as large as the bundle of lamellae in the melt; hence, in this study, b_f is equivalent to the lamella thickness (d_c). In the following part, I describe the estimation of λ^*. To estimate the values of λ^*, we needs b_f, v_c, Δv, η, G, and σ. Several G values were determined from the microscope observations at T_c = 290–300 °C. The time evolutions of the size in the longitudinal direction of several needle-like crystals were investigated. Subsequently, considering their anisotropies, the largest G value in each T_c was adopted. Finally, the value was halved. As stated above, axialites are commonly observed in regime I. Hence, I assumed that the P3MB1 crystals grow in regime I, at least for T_c > 290 °C. According to L-H theory, G is expressed as[22]

$$G = G_0 \exp\left(\frac{-\Delta E}{RT_c}\right)\exp\left(\frac{-K}{T_c \Delta T}\right) \quad (2.5)$$

Particularly in regime I,

$$K = \frac{4 b_s \sigma \sigma_e T_m^0}{k_B \Delta H} \quad (2.6)$$

where G_0, ΔE, b_s, σ_e, k_B, and ΔH are the preexponential factor, activation energy of chain motion in the melt, thickness of the molecular stem, fold surface free energy, Boltzmann

constant, and enthalpy of fusion, respectively. They are all constants independent of the temperature in this study ($\Delta T = T_m^0 - T_c$). ΔE of P3MB1 was calculated from the viscoelasticity data of Takayanagi.[24] $\Delta E = \ln a_T R T_1 T_2/(T_2 - T_1) = 40$ kJ/mol. Here, a_T is the shift factor and $\ln a_T = 2.63$, $T_1 = 363$ K and $T_2 = 453$ K. Equation (2.5) was transformed as $\ln G + Q/RT_c = \ln G_0 - K/T_c\Delta T$, and the $\ln G + Q/RT_c$ vs $1/T_c\Delta T$ plot was obtained (Figure 2.5). Assuming that T_c = 290–300 °C is the range of regime I and fitted to a linear line, G_0 and K were obtained from the ordinate intercept and the slope, respectively. All parameters for Eq. (2.5) are shown in Table 2.1. For comparison, those of PE (M_w = 74,400, M_w/M_n = 1.12) reported by Armistead and Hoffman are also listed.

Table 2.1 Parameters for P3MB1 and PE in Eq. (2.5)

	P3MB1	PE (M_w = 74,400, M_w/M_n = 1.12)
T_m^0 (K, °C)	596.1, 322.9	417.9, 144.7 (ref 24)
ΔE (kJ/mol)	40.0	24.0 (ref 25)
G_0 for regime I, II, III (cm/s)	4.56×10^5 (regime I)	1.4×10^{10}, 1.02×10^3, 1.65×10^7 (ref 22)
K for regime I, II, III (K^2)	2.26×10^5 (regime I)	1.98×10^5, 0.940×10^5, 1.85×10^5 (ref 22)

To evaluate σ in Eq. (2.6), the following analyses were conducted. First, ΔH was calculated from the Clausius-Clapeyron equation,[2] expressed as

$$\Delta H = T_m(V_l - V_c)/\frac{dT_m}{dp} \tag{2.7}$$

where V_l and V_c are the atmospheric pressure volumes of the melt and the crystal at T_m, respectively. dT_m/dp is the dependence of T_m on pressure. Selected isobars in the PVT relationship of P3MB1 are shown in Figure 2.6. The intersection points of the black solid

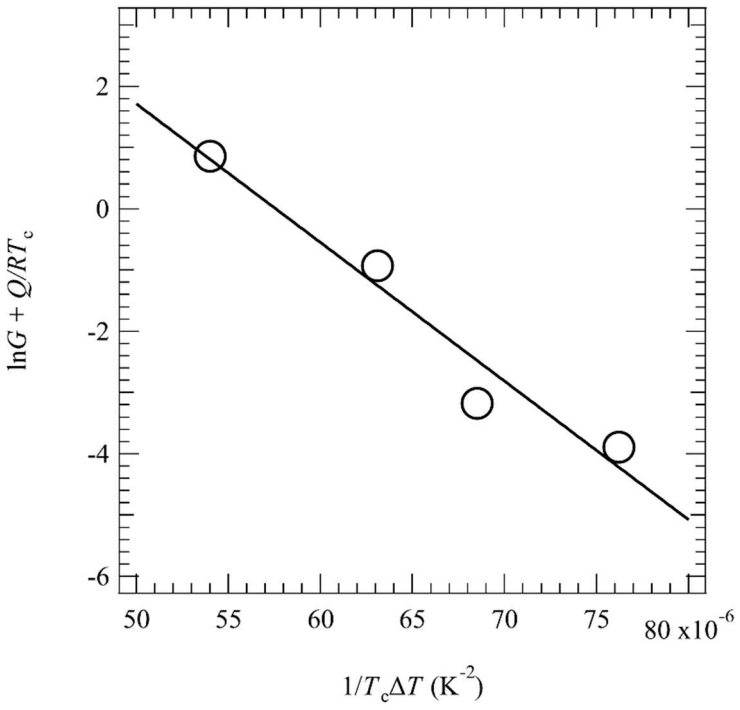

Figure 2.5 Plots of $\ln G + Q/RT_c$ vs $1/T_c\Delta T$. $G_0 = 4.56\times10^5$ cm/s and $K = 2.26\times10^5$ K^2.

lines correspond to T_m. $V_l = 1.439$ cm^3/g was obtained by fitting the volume at 0 MPa and $T > T_m$ to a quadratic function. Figure 2.7 shows the pressure dependence of T_m of P3MB1. The solid line is the fitting curve expressed by a third-order polynomial. By differentiating it, I obtained $dT_m/dp = 0.844$ °C/MPa. The results of the WAXS measurements to evaluate V_c are shown in Figure 2.8. Finally, $\Delta H = 113$ J/cm^3 was calculated. All parameters for Eq. (2.7) are shown in Table 2.2.

Table 2.2 Parameters for Eq. (2.7)

T_m	V_l	V_c	dT_m/dp	ΔH
585 K	1.439 cm^3/g	1.103 cm^3/g	0.844 °C/MPa	113 J/cm^3
312 °C				124 J/g

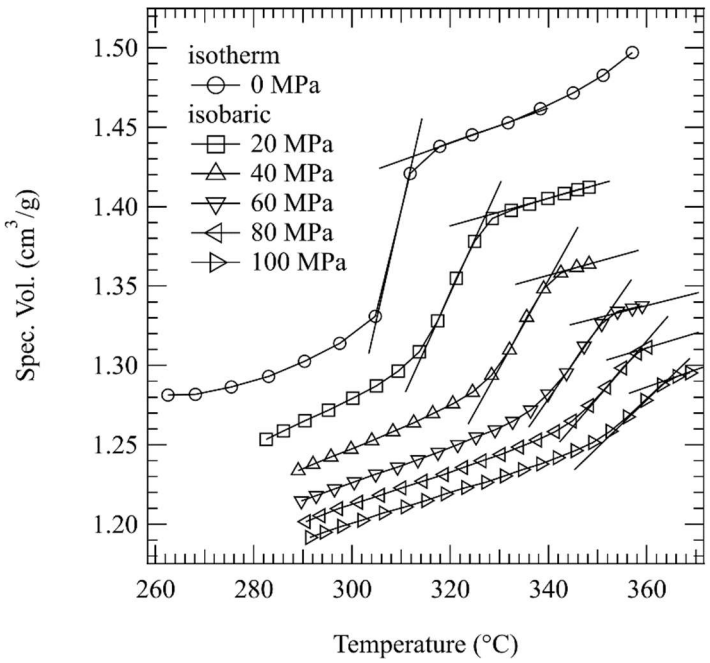

Figure 2.6 Selected isobars in the PVT relationship of P3MB1. The 0 MPa volume was extrapolated from the isotherm measurements at 10–30 MPa. The intersection points of the black solid lines correspond to T_m.

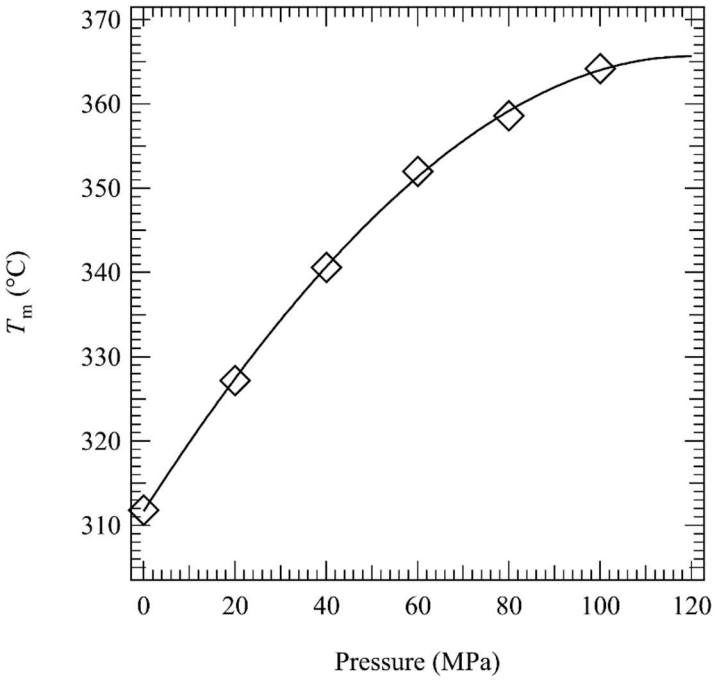

Figure 2.7 Pressure dependence of T_m of P3MB1. The solid line is the fitting curve expressed by a third-order polynomial.

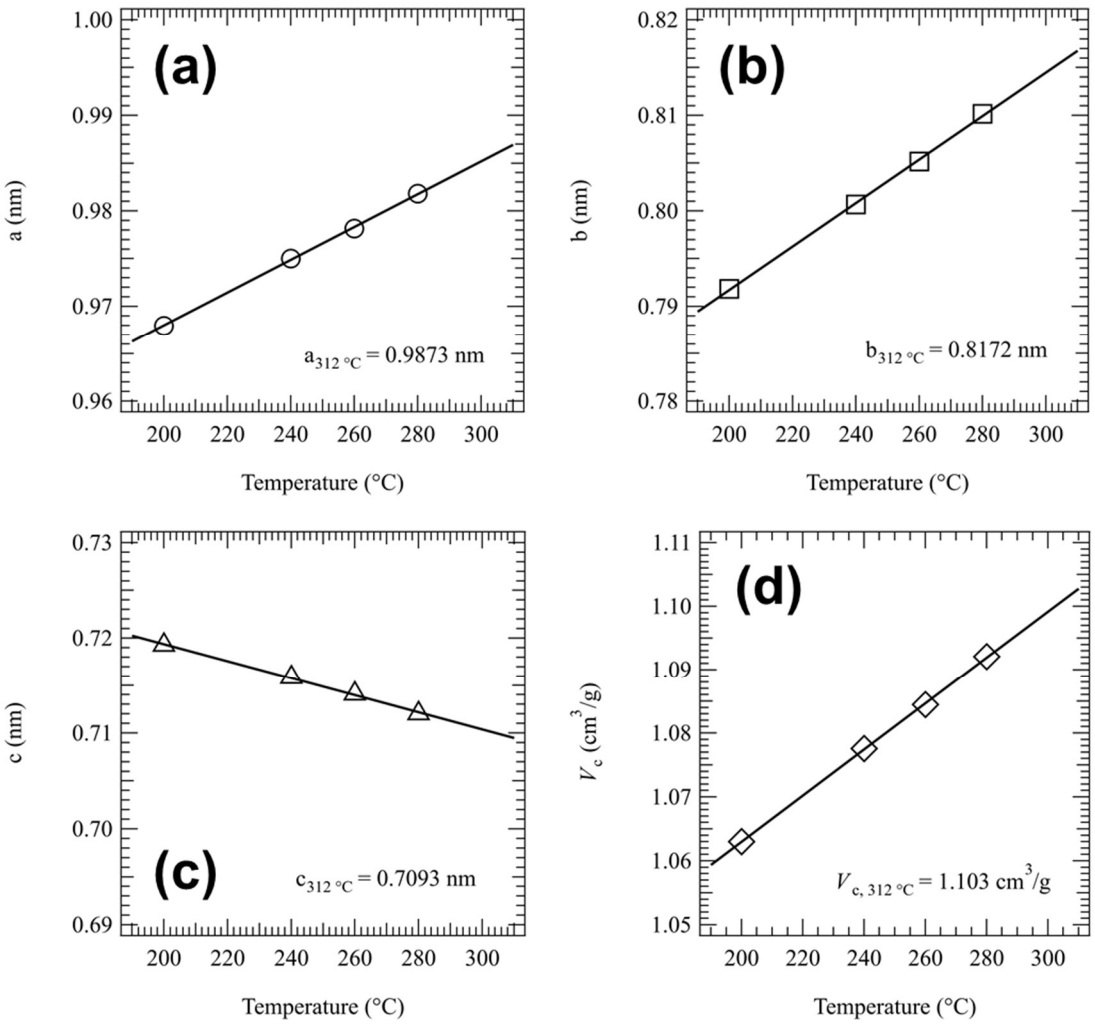

Figure 2.8 Temperature dependence of the lattice constants (a) *a*, (b) *b*, (c) *c*, and the specific volume (d) V_c of the P3MB1 crystal measured by WAXS. Diffractions from the (100), (101), and $(1\bar{1}1)$ lattice planes were used for the calculation. All axial angles were fixed and independent of temperature.

Next, σ_e was obtained using the Gibbs-Thomson equation. expressed by[11]

$$T_m = T_m^0\left(1 - \frac{2\sigma_e}{\Delta H d_c}\right) \quad (2.8)$$

d_c was calculated from the SAXS profile at T_c = 290 °C and t = 300 s by using the correlation function, as shown in Figure 2.9.[27] The results of FSC were used for T_m. Corradini et al. reported a P3MB1 monoclinic unit cell with

a = 9.55 Å, b = 8.54 Å, c = 6.84 Å, γ = 116.30 ° (ref 6)

From these values, the lattice spacings of the (100), (010), and (110) planes were calculated to be 8.56 Å, 7.66 Å, and 7.63 Å, respectively. Here, I assumed the value of the (110) plane as b_s. Finally, σ was obtained from Eq. (2.6). All parameters for Eq. (2.6) are shown in Table 2.3. The σ_e and σ values of P3MB1 are both smaller than those of PE.

The ΔT dependence of λ^* was calculated by Eq. (2.4) and is shown in Figure 2.10 for each polymer. Note that the curve of P3MB1 was calculated by assuming regime I for T_c = 290–300 °C. The η of P3MB1 at 310 °C was 51.4 Pa·s. Hence, the temperature dependence of η was obtained by the Andrade equation,[29] $\eta = \eta_0\exp(\Delta E/RT) = 1.3\times10^{-2}\exp(4.8\times10^2/T)$. Using the same way as Toda et al., I calculated the η of PE from the Vogel-Fulcher equation. based on the results of Pearson et al.[30] The d_c values of both polymers were evaluated by Eq. (2.8). The T_m of PE was obtained by considering the doubling of the lamellar thickness ($T_m = (T_c+T_m^0)/2$).[12] The value of $v_c/\Delta v$ is 4.5.[31,32]

Comparing at the same ΔT, P3MB1 has a larger λ^* than PE and forms axialites or needle-like crystals in the range where PE forms spherulites. All parameters for P3MB1 at T_c = 297 °C and PE at the same ΔT (26 °C) as for P3MB1 are shown in Table 2.4. The difference in η affects λ^* most strongly. Hence, one of the most significant factors for the

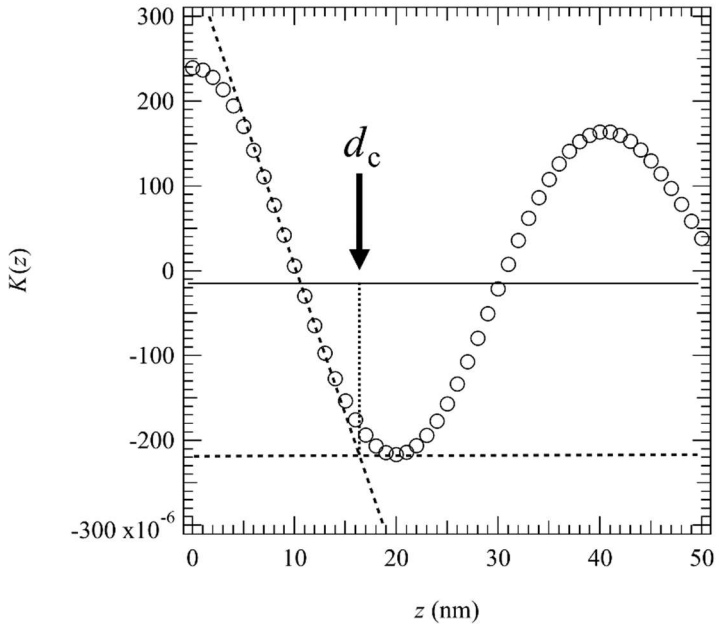

Figure 2.9 1D electron density correlation function $K(z)$ of P3MB1 at T_c = 290 °C. $K(z)$ is defined below and experimentally integrated q = 0.11–0.24 nm^{-1}.

Table 2.3 Parameters for P3MB1 and PE in Eq. (2.6)

	P3MB1	PE (M_w = 74,400, M_w/M_n = 1.12)
ΔH (J/cm^3, J/g)	113, 124	280, 293 (ref 28)
d_c (nm)	16.3 (T_c = 290 °C, T_m = 301 °C)	-
b_s (Å)	7.63 ((110) plane spacing)	4.15 (ref 28)
σ_e (J/cm^2)	3.29×10^{-6}	9.0×10^{-6} (ref 28)
σ (J/cm^2)	5.87×10^{-7}	11.8×10^{-7} (ref 28)

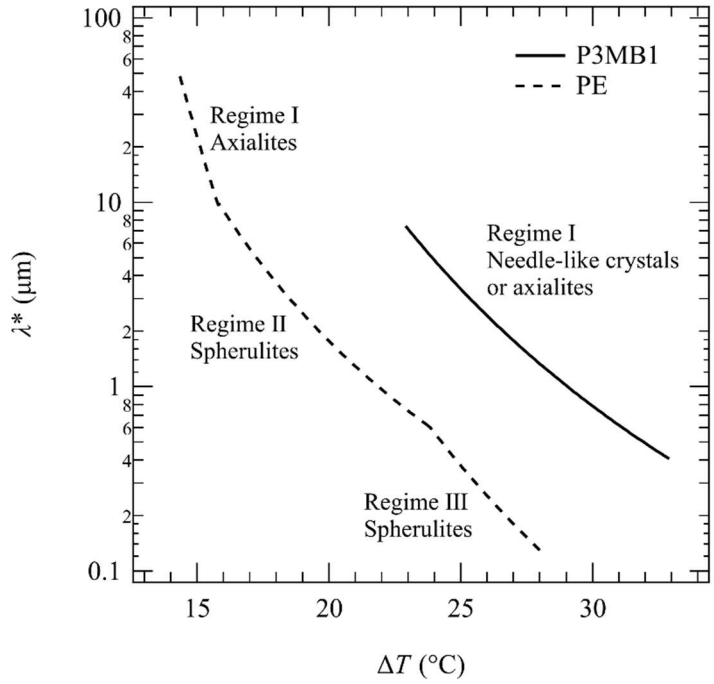

Figure 2.10 G dependence of ΔT of P3MB1 and PE (M_w = 74,400, M_w/M_n = 1.12) calculated by Eq. (2.4).

suppression of branching in P3MB1 was the low η at T_c. Of course, the η of P3MB1 is higher than that of PE at the same temperature, due to its bulkier side group. However, P3MB1 has a very high T_m and often crystallizes with a low η that cannot be reached when PE crystallizes. In such a case, the characteristic morphology may be observed.

However, the range of λ^* in the temperature region where the needle-like crystals of P3MB1 were observed is $0.41 < \lambda^* < 7.4$ μm, and PE forms the spherulites in the same range of λ^*, indicating that suppression is not the only origin of the needle-like crystals in P3MB1. I believes that another reason may be the flow of the needle-like crystals in the melts. As observed in the OM images, the low viscosity induces the flow of the needle-like crystals. The flow may induce the local orientation of the polymer chains in the melts and the orientation might suppress the branching.

Table 2.4 Parameters for P3MB1 and PE in Eq. (2.4) at ΔT = 26 °C

	P3MB1	calculated by
b_f (nm)	21 (T_c = 297 °C, T_m = 306 °C)	Eq. (2.8), FSC and SAXS data
$v_c/\Delta v$	3.2	WAXS and PVT data
G (cm/s)	1.8×10^{-5}	Eq. (2.5) and Table 2.1
η (Pa·s)	62	Andrade equation, η at 310 °C and ref 23
λ^* (μm)	2.8	Eq. (2.4)

	PE (M_w = 74,400, M_w/M_n = 1.12)	calculated by
b_f (nm)	21 (T_c = 119 °C, T_m = 132 °C)	Eq. (2.8) and ref 12, 22
$v_c/\Delta v$	4.5	ref 31, 32
G (cm/s)	1.0×10^{-4}	ref 22
η (Pa·s)	3.8×10^{3}	ref 30
λ^* (μm)	0.30	Eq. (2.4)

2.4 Conclusion

I investigated the isothermal crystallization of P3MB1, a polyolefin with a high melting temperature, after the onset of quench from the molten state by OM observations and time-resolved SAXS and WAXS measurements. At T_c = 297 °C, the OM observations revealed that needle-like crystals were formed and moved in melt matrices. Anisotropic scattering patterns were observed in SAXS and WAXS at 297 °C, and the anisotropies and the scattering intensities changed irregularly with time. The irregular changes in scattered intensity are due to the flow of the needle-like crystals in and out of the irradiated area of the incident X-ray beam. This needle-like crystal is not a single crystal, but one composed of stacked lamellae.

As T_c increased, the morphological transition from spherulites to needle-like crystals was considered to occur via axialites. In other words, the needle-like crystals were considered axialites without lamellar branches. To elucidate the origin of the

suppression of branching, I evaluated thermodynamic parameters such as ΔH, d_c, and σ, and calculated λ^* for P3MB1 and PE. λ^* for P3MB1 was larger than that for PE, suggesting that the suppression of branching is due to the low η at T_c. The low viscosity also induces the local orientation of the polymer chains in the melts, and this orientation might suppress branching.

References

1. Charlet, G.; Delmas, G., *J. Polym. Sci. Part B: Polym. Phys.* **1988,** *26*, 1111-1125.
2. Zoller, P.; Starkweather, H. W.; Jones, G. A., *J. Polym. Sci. Part B: Polym. Phys.* **1986,** *24*, 1451-1458.
3. Mita, K.; Okumura, H.; Kimura, K.; Isaki, T.; Takenaka, M.; Kanaya, T., *Polym. J.* **2012,** *45*, 79.
4. Quynn, R. G.; Sprague, B. S., *J. Polym. Sci. Part A-2: Polym. Phys.* **1970,** *8*, 1971-1985.
5. Kirshenbaum, I.; Feist, W. C.; Isaacson, R. B., *J. Appl. Polym. Sci.* **1965,** *9*, 3023-3031.
6. Corradini, P.; Ganis, P.; Petraccone, V., *Eur. Polym. J.* **1970,** *6*, 281-291.
7. Utsunomiya, H.; Kawasaki, N.; Niinomi, M.; Takayanagi, M., *J. Polym. Sci. Part B: Polym. Lett.* **1967,** *5*, 907-910.
8. Jones, A. T.; Aizlewood, J. M., *J. Polym. Sci. Part B: Polym. Lett.* **1963,** *1*, 471-476.
9. Reding, F. P.; Faucher, J. A.; Whitman, R. D., *J. Polym. Sci.* **1962,** *57*, 483-498.
10. Masunaga, H.; Ogawa, H.; Takano, T.; Sasaki, S.; Goto, S.; Tanaka, T.; Seike, T.; Takahashi, S.; Takeshita, K.; Nariyama, N.; Ohashi, H.; Ohata, T.; Furukawa, Y.; Matsushita, T.; Ishizawa, Y.; Yagi, N.; Takata, M.; Kitamura, H.; Sakurai, K.; Tashiro, K.; Takahara, A.; Amamiya, Y.; Horie, K.; Takenaka, M.; Kanaya, T.; Jinnai, H.; Okuda, H.; Akiba, I.; Takahashi, I.; Yamamoto, K.; Hikosaka, M.; Sakurai, S.; Shinohara, Y.; Okada, A.; Sugihara, Y., *Polym. J.* **2011,** *43*, 471-477.
11. Hoffman, J. D.; Weeks, J. J., *J. Chem. Phys.* **1962,** *37*, 1723-1741.

12. Toda, A.; Taguchi, K.; Nozaki, K.; Konishi, M., *Polymer* **2014,** *55*, 3186-3194.

13. Furushima, Y.; Nakada, M.; Takahashi, H.; Ishikiriyama, K., *Polymer* **2014,** *55*, 3075-3081.

14. Toda, A.; Androsch, R.; Schick, C., *Polymer* **2016,** *91*, 239-263.

15. Hikosaka, M.; Amano, K.; Rastogi, S.; Keller, A., *Macromolecules* **1997,** *30*, 2067-2074.

16. Rastogi, S.; Höhne, G. W. H.; Keller, A., *Macromolecules* **1999,** *32*, 8897-8909.

17. Asakawa, H.; Nishida, K.; Kanaya, T.; Tosaka, M., *Polym J* **2013,** *45*, 287-292.

18. Toda, A.; Okamura, M.; Taguchi, K.; Hikosaka, M.; Kajioka, H., *Macromolecules* **2008,** *41*, 2484-2493.

19. Kajioka, H.; Hikosaka, M.; Taguchi, K.; Toda, A., *Polymer* **2008,** *49*, 1685-1692.

20. Gránásy, L.; Pusztai, T.; Tegze, G.; Warren, J. A.; Douglas, J. F., *Phys. Rev. E* **2005,** *72*, 011605.

21. Hoffman, J. D., *J. Res. Nat. Bur. Stand. Section A.* **1975,** *79A*, 671-699.

22. Armistead, J. P.; Hoffman, J. D., *Macromolecules* **2002,** *35*, 3895-3913.

23. Toda, A.; Taguchi, K.; Kajioka, H., *Macromolecules* **2008,** *41*, 7505-7512.

24. Takayanagi, M., *Pure Appl. Chem.* **1970,** *23*, 151-182.

25. Flory, P. J.; Vrij, A., *J. Am. Chem. Soc.* **1963,** *85*, 3548-3553.

26. Fletcher, D.; Klein, J., *Polym. commun.* **1985,** *26*, 2-4.

27. Strobl, G., The Physics of Polymers. *Springer-Verlag Berlin Heidelberg* **2007**.

28. Hoffman, J. D.; Miller, R. L., *Polymer* **1997,** *38*, 3151-3212.

29. Andrade, E. N. d. C., LVIII. A theory of the viscosity of liquids.—Part II. *Lond., Edinb., Dub. Philos. Mag. J. Sci.* **1934,** *17*, 698-732.

30. Pearson, D. S.; Ver Strate, G.; Von Meerwall, E.; Schilling, F. C.,

Macromolecules **1987,** *20*, 1133-1141.

31. Orwoll, R. A., *J. Am. Chem. Soc.* **1967,** *89*, 6814-6822.

32. Cole, E.; Holmes, D., *J. Polym. Sci.* **1960,** *46*, 245-256.

Chapter 3
Spatial Distribution of the Amorphous Region with Reduced Mobility

3.1 Introduction

Crystalline polymer materials are generally composed of crystalline and amorphous phases. Many studies have supported that the presence of crystallites affects the mobility of chains in the amorphous phase and that there is the region with reduced mobility in the amorphous phase.[1-7] Hertlein et al. found that the three relaxation processes in spin-spin relaxation obtained by pulsed proton nuclear magnetic resonance (^{1}H-NMR) measurements during the isothermal crystallization of various polymers. [3] They concluded that the fast, medium, slow relaxation processes originate from the crystalline region, the rigid amorphous region, and the melt-like amorphous region, respectively, and found that the weight fraction of the rigid amorphous region increases with the proceeding of crystallization. Differential scanning calorimetry have also detected the rigid amorphous region. It is known that the heat capacity just above the glass transition temperature (T_g) deviates from the heat capacity predicted from the crystallinity.[4-6] The result suggests that the amorphous region with higher T_g, or the rigid amorphous region exist in addition to the crystalline and melt-like region. Dynamic mechanical, dielectric, and raman spectroscopy also characterize the rigid amorphous region.[1,6,7]

However, we cannot determine the spatial distribution of the rigid amorphous

region by using the abovementioned experiments. It is very difficult to distinguish the rigid amorphous region from the melt-like amorphous region by using the small angle X-ray scattering (SAXS) in the bulk state because they have almost the same density.[8,9] To overcome the difficulty, I attempted to observe the rigid amorphous region by the SAXS experiment of the crystalline polymer swollen by solvent. In the swollen state, the rigid amorphous region does not swell more than the melt-like region, so we can distinguish between the rigid amorphous and the melt-like regions. Moreover, I applied contrast variation small-angle scattering (CV-SAS) method for a crystalline polymer under solvent swelling. CV-SAS can separate the scattering length density (SLD) and the spatial distribution of each component for a multicomponent system.[10-15] Therefore, separation of the spatial distribution of the crystalline and amorphous components under solvent swelling reveals the features and spatial distribution of the two amorphous regions.

I used ethylene-octene copolymer (EOC) as the crystalline polymer to apply CV-SAS. EOC is one of the commodity plastics used for automotive materials, shoes, wire coating, etc. I chose EOC for the following three reasons. (i) Even good solvents cannot permeate the crystalline phase of EOC. The bulk specimen turns into a gel state under solvent swelling, where the crystallites behave as physical cross-linking points. (ii) EOC has low crystallinity, so it provides a clearer spatial correlation between the crystalline regions and the amorphous regions with reduced mobility. (iii) The EOC with suitable swelling properties for the measurement can be easily obtained since many grades of EOC with crystallinity and molecular weight are commercially available. A high molecular weight grade with crystallinity of approximately 20 % was the best for this study because it absorbs the sufficient amount of solvents without elution of the polymer.

CV-SAS is usually conducted with small angle neutron scattering (so-called CV-

SANS). In CV-SANS, the scattering contrast can be varied without changing the structures by using mixtures of deuterated and hydrogenated solvent and varying their mixing ratio. Especially, several studies on nanocomposites have been reported to evaluate the dense polymer layer near the filler surface.[11-14] One might think that the similar CV experiment, where the crystallites are regarded as the filler, reveals the concentration fluctuations in the swollen amorphous region. However, CV-SANS is not suitable for this study because the difference in the neutron SLD between the crystalline and amorphous phase is very small, as discussed later. Thus, I conducted CV small angle X-ray scattering (CV-SAXS) using two solvents, 4-ethyltoluene (Et-tol) and 2-Br-xylene (Br-xyl), whose interaction with the EOC is equivalent and whose scattering ability, or electron density is different from each other.

In this chapter, I performed CV-SAXS of the EOC under solvent swelling and clarified the features and spatial distribution of the concentration fluctuations in the swollen amorphous region. In addition, I discussed the relationship between the two amorphous regions with different swelling properties determined by CV-SAXS and the amorphous regions with different mobility determined by pulsed ^{1}H-NMR.

3.2 Experimental Section

3.2.1 Solvent Swelling of Chemically Cross-Linked EOC

Pellets of ENGAGE 8003 (Dow Chemical) were used as the EOC. The melt index at 190℃/2.16 kg and the melting temperature (T_m) are 1 g/10 min and 77℃, respectively. 10 wt% hot *p*-xylene solution, containing the EOC and dicumyl peroxide in weight ratio of 100/3, was prepared. The solution was spread out on a Petri dish, dried under reduced pressure, and subsequently heated at 150°C for 3 hours to proceed the

cross-linking reaction. Note that the EOC was kept above the T_m from dissolution until the completion of the cross-linking reaction. The cross-linked specimen was refluxed with *p*-xylene at 138°C for 3 hours to remove the unreacted components.

For the estimation of the average molecular weight between the crosslinks (M_c), the storage shear modulus (G') of the vacuum-dried specimen at 160°C was measured by a rheometer, MCR 302 (Anton Paar). The strain was 1% and the angular frequency was 0.1 to 100 rad/s.

The swelling ratio (Q) measurements were performed as follows. Here, $Q = V_a/V_b$, and V_b and V_a are the volumes before and after swelling, respectively. The weight of the vacuum-dried specimen was measured. Then, the weight at the equilibrium state after solvent swelling above T_m was measured, and the Q was calculated. The density of the molten EOC, Et-tol, and Br-xyl were fixed at 0.855 g/cm^3, 0.861 g/cm^3, and 1.34 g/cm^3, respectively.

3.2.2 Preparation of Film Specimens for Pulsed ^{1}H-NMR and CV-SAXS Measurements

The pellets of ENGAGE 8003 were pressed between two glass slides on a heater at 160°C. After 5 minutes, they were dropped into ice water to crystallize. The thickness of the obtained specimens were approximately 250 μm. Note that this preparation procedure does not include any chemical cross-linking.

3.2.3 Pulsed ^{1}H-NMR Measurements

Pulsed ^{1}H-NMR measurements were performed on the film specimen by using JNM-MU25 (JEOL). Free induction decays (FIDs) were detected by solid echo[16] and

Hahn echo method[17] at 23°C.

3.2.4 CV-SAXS measurements

The film specimens were swollen by Br-xyl/Et-tol mixtures with different mixing ratio at 23℃ for more than 48 hours to reach their equilibrium states. The SAXS measurements were performed at 23℃ by using Nanoscale Dynamic Structural Analysis X-ray System of Institute for Chemical Research, Kyoto University. The main unit of the system consists of NANO-Viewer (RIGAKU) and the detector is PILATUS 100K (DECTRIS). The wavelength of the incident X-rays, the camera length, and the exposure time were, respectively, 1.54 Å, 1024 mm, and 1 hour. The swollen specimens were sealed in a cell to prevent the solvent from evaporating during the measurement, and Kapton films were used as the window. The two-dimensional (2D) scattering intensity of the empty cell was subtracted from the 2D scattering intensity obtained from each sample, taking into account the transmittance. The two solvents and the EOC without swelling were, respectively, measured to correct the thermal diffuse scattering (TDS) intensity.

3.3 Results and Discussion

3.3.1 Dynamics without Solvent Swelling

Figure 3.1 shows the FID signals obtained by pulsed ^{1}H-NMR measurements. When several components with different mobility exist in the system, the FID curve can be expressed by[18]

$$M(t) = \sum_i M_{0,i} \exp\left[-\left(\frac{t}{T_{2,i}}\right)^{W_i}\right] \tag{3.1}$$

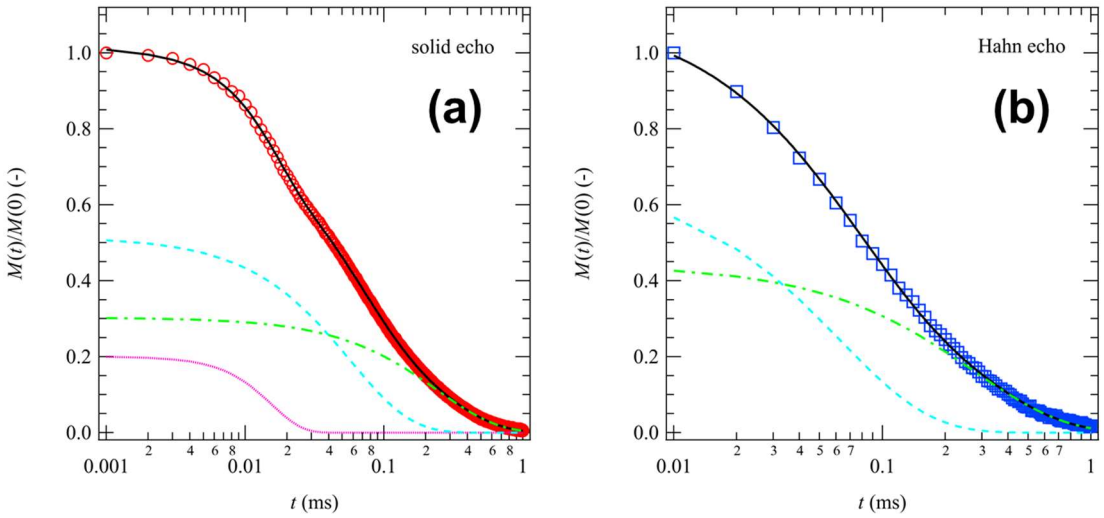

Figure 3.1 FID signals obtained by (a) solid echo and (b) Hahn echo, respectively. The solid curves in the figure indicate the best fit by using Eq. (3.1). The dotted, dashed, and dot-dashed curves indicate the contribution of the crystalline, rigid amorphous, and melt-like components, respectively.

where $M_{0,i}$, W_i, and $T_{2,i}$ are, respectively, the signal intensity at t = 0, the Weibull coefficient, and is the time constant of the transverse relaxation of the i component. W ranges from 1 to 2, W = 1 for sufficiently fast motion and W = 2 for sufficiently slow motion. The weight fraction of the i component $\phi_{i,\mathrm{w,NMR}}$ can be obtained by

$$\phi_{i,\mathrm{w,NMR}} = \frac{M_{0,i}}{\sum_i M_{0,i}} \tag{3.2}$$

By fitting, I was able to separate the FID signals obtained by the solid echo and Hahn echo into three and two components, respectively, as shown in Figure 3.1(a) and (b). While the time range evaluated by Hahn echo is narrower than that by the solid echo, Hahn echo provides more accurate detection for long time region because it is not affected by inhomogeneity of the magnetic field. Therefore, I obtained the weight fraction of the

component with the smallest T_2 by the result of solid echo, and subsequently determined the weight fractions of the other two components according to the result of Hahn echo. The obtained parameters and weight fractions are listed in Table 2.1. The component with the smallest T_2, or, the lowest mobility, was well fitted at $W = 2$, which implies that this component is frozen as the crystalline or glassy state. The weight crystallinity determined from the film density (0.885 g/cm^3) was 23 %. Considering that this value is close to the weight fraction of the component with the lowest mobility (20 %), I attributed this component to the crystalline region. The components with the medium and highest mobility showed T_2 that were approximately 4 and 16 times larger, respectively, than that of the component with lowest mobility. The W of these two components was approximately 1, suggesting that they were not frozen at 23°C. Therefore, I attributed the components with the medium and highest mobility to the rigid amorphous region and the melt-like region, respectively.

Table 3.1 Fitting Parameters obtained by pulsed ^{1}H-NMR

	Crystalline region	Rigid amorphous region	Melt-like region
Weight fraction (%)	20	48	32
T_2 by solid/Hahn echo (ms)	0.015 / -	0.059 / 0.062	0.239 / 0.274
W* by solid/Hahn echo	2 / -	1.06 / 1	1 / 1

*Obtained by the constraint of $1 \leqq W \leqq 2$.

3.3.2 Evaluation of the Interaction Parameters between the EOC and Solvents

CV-SAS under solvent swelling requires that the structure must be identical regardless of the solvent mixing ratio. In this section, I show that Et-tol and Br-xyl have equivalent interactions with the EOC, respectively.

Flory-Rehner theory is well known as one of the models describing the interaction parameter (χ) between the polymer and solvent. In this theory, χ is related to Q of the chemically cross-linked polymer as[19]

$$\chi = -Q^2\left[\ln\left(1-\frac{1}{Q}\right)+\frac{1}{Q}+\frac{V_1}{\bar{v}M_c}\left(1-\frac{2M_c}{M_w}\right)\left(\frac{1}{Q^{1/3}}-\frac{1}{2Q}\right)\right] \tag{3.3}$$

where $\bar{v}$ is the specific volume of the polymer, V_1 is the molar volume of solvent, and M_w is the primary molecular weight. This theory is based on chemically cross-linked polymers with homogeneous network structures, so I measured Q in the high temperature range without crystalline structures. Figure 3.2 shows the temperature dependence of Q for the chemically cross-linked EOC. Q for the two solvents agreed in the high temperature range. I determined the Q at 23°C by linear extrapolation, and obtained the Q for Et-tol and Br-xyl, 12.5 and 12.6, respectively.

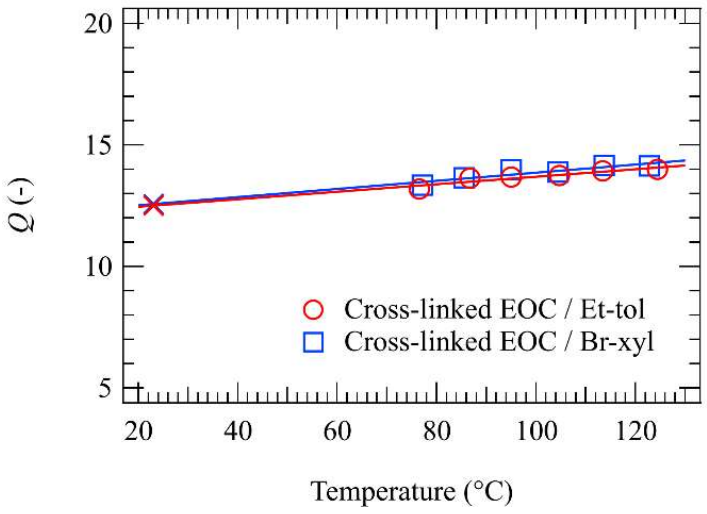

Figure 3.2 Solvent swelling behavior of the chemically cross-linked EOC. The cross marks indicate the Q at 23°C obtained by linear extrapolation.

M_c is related to G' as[20]

$$M_c = \frac{\rho RT}{G'} \tag{3.4}$$

where ρ is the density ($\rho = 1/\bar{v}$), and R is the gas constant. I obtained M_c = 33,200 by the plateau modulus at 160°C and Eq. (3.4). Note that the ρ at 160°C was calculated with the data of Orwoll and Flory.[21] In addition, M_w = 151,000,[22] and V_1 of Et-tol and Br-xyl are 140 cm^3/mol and 138 cm^3/mol, respectively.

From the above parameters and Eq. (3.3), the χ was obtained to be 0.41 at 23°C for both solvents. This agreement indicates that the interaction of the EOC with these two solvents is equivalent at 23°C.

3.3.3 Swelling Properties of the EOC in Br-xyl/Et-tol Mixtures

In this section, I confirm that the agreement of the polymer-solvent interactions is effective even in the presence of crystallites. Note that all the following results are obtained by specimens without chemical cross-linking.

Figure 3.3(a) shows the dependence of Q on the solvent mixing ratio. Q was constant independent of the mixing ratio, and the average value (Q_{av}) was 1.787. This result supports that the swollen specimens have the same structures independent of the mixing ratio.

Figure 3.3(b) shows the dependence of the X-ray transmittance on the solvent mixing ratio. The observed values agreed with the ones calculated from the thickness of the specimens and the absorption coefficients in the literature.[23] This result indicates that

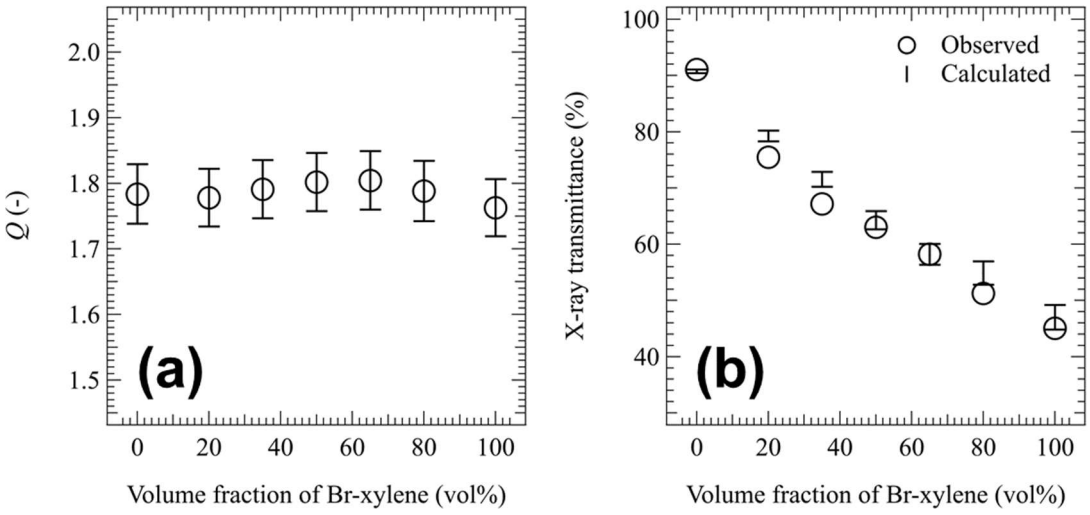

Figure 3.3 Dependence of the solvent mixing ratio on (a) Q and (b) X-ray transmittance of the EOC at 23℃, respectively.

the EOC did not selectively absorb only one of the solvents, but absorbed the mixed solvents as prepared.

From the above results, I concluded that the mixed solvents with different electron densities provide the same structure even in the presence of crystallites.

In addition, I vacuum dried the swollen specimens to evaporate the solvent, and measured the weight of them. The weight loss compared to the weight before swelling was less than 2 wt% for all the specimens. Thus, the elution of the polymer can be ignored.

3.3.4 Structure Analysis by CV-SAXS under Solvent Swelling

In this section, I calculate partial scattering functions $S_{ij}(q)$, which will be defined later, from SAXS profiles, and analyzes $S_{ij}(q)$ by fitting.

All the specimens showed isotropic 2D patterns. In addition, I confirmed that the scattering intensities of the two solvents were, respectively, constant in the obtained q range. Here, q is the magnitude of the scattering vector defined by $q = (4\pi/\lambda_{\text{X-ray}})\sin(\theta/2)$

with $\lambda_{\text{X-ray}}$ and θ being the wavelength of the incident X-rays and the scattering angle, respectively. Thus, to correct the TDS intensity, I subtracted the intensities at q = 1.8 nm^{-1} for the EOC without swelling, Et-tol, and Br-xyl multiplied by the volume fraction of each component from the circular-averaged scattering profiles $I(q)$. Figure 3.4 shows $I(q)$ after the TDS correction. $I(q)$ varied depending on the solvent mixing ratio.

I calculate $S_{ij}(q)$ from $I(q)$ in Figure 3.4, treating as the three-component system. Under incompressible conditions, $I(q)$ can be expressed as

$$I(q) = (a_{\text{c}} - a_{\text{s}})^2 S_{\text{cc}}(q) + 2(a_{\text{c}} - a_{\text{s}})(a_{\text{a}} - a_{\text{s}}) S_{\text{ca}}(q) + (a_{\text{a}} - a_{\text{s}})^2 S_{\text{aa}}(q) \qquad (3.5)$$

where a_i is the X-ray SLD of the i component (i: c, crystalline phase; a, amorphous phase; s, solvent). In this study, I define the X-ray SLD as (electron density) × (classical electron radius). Figure 3.5 shows the dependence of the X-Ray SLD of each component on the solvent mixing ratio. The densities of crystalline and amorphous phase are 1.000 g/cm^3 and 0.855 g/cm^3, respectively.[24] Using these X-ray SLD and Eq. (3.5), we can decompose $I(q)$ into $S_{ij}(q)$ defined by

$$S_{ij}(q) = \frac{1}{V} \iint \left(\delta\phi_i(\vec{r}) \delta\phi_j\left(\overrightarrow{r'}\right) \right) \exp\left[i\vec{q}\left(\vec{r} - \overrightarrow{r'}\right) \right] d\vec{r} d\overrightarrow{r'} \qquad (3.6)$$

where V is the scattering volume radiated by the incident beam and $\delta\phi_i(\vec{r})$ is the fluctuation of the volume fraction of i component at position $\vec{r}$.

In this study, I obtained seven $I(q)$ to calculate three $S_{ij}(q)$. Thus, I employed the singular value decomposition algorithm to calculate the accurate $S_{ij}(q)$.[10, 12] Figure 3.6 shows the obtained $S_{ij}(q)$. $-S_{\text{ca}}(q)$ is also shown in Figure 3.6(b) because $S_{\text{ca}}(q)$ is positive

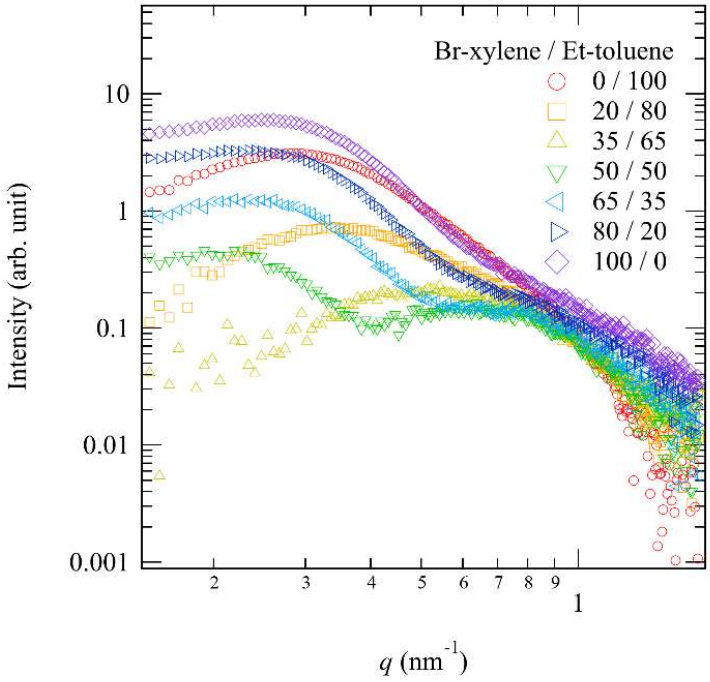

Figure 3.4 SAXS profiles of the EOC swollen by Et-tol/Br-xyl mixtures.

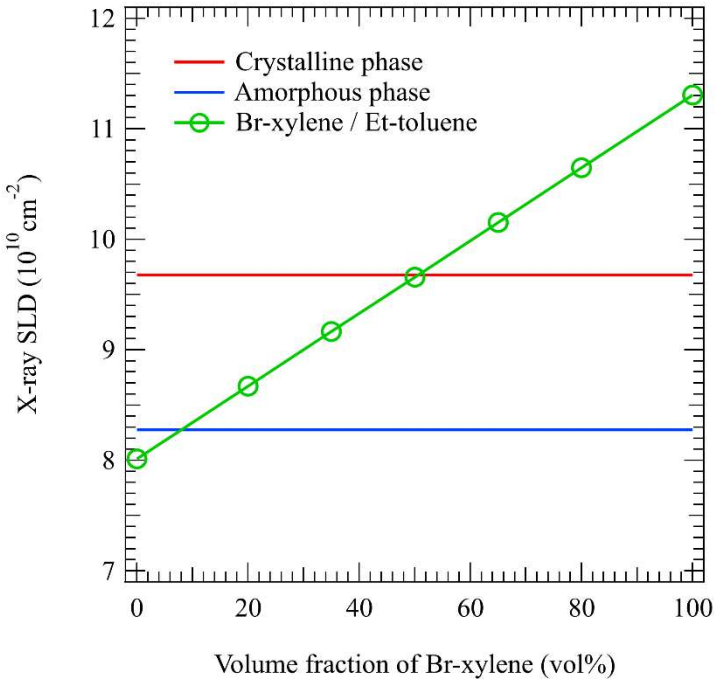

Figure 3.5 Dependence of the solvent mixing ratio on the X-ray SLD of each component. The circle marks correspond to the conditions measured by SAXS.

in the smaller q region and negative in the larger q region.

I describe the model functions to fit the experimental $S_{ij}(q)$. According to the study by Bensason et al., the EOC used in this study is categorized as elastomer due to its density.[25] They clarified by transmission electron microscopy that elastomers show a morphology with random distribution of granular crystallites instead of lamellar structures as seen in high-density polyethylene.[1, 26] Thus, I assumed the existence of the highly concentrated amorphous region surrounding the crystallites, as shown in Figure 3.7. When the crystalline region, the highly concentrated amorphous region, and the matrix region are denoted as α, β, and γ, respectively, $S_{ij}(q)$ can be expressed by

$$S_{\mathrm{cc}}(q) = F_{\alpha}(q)^2 S(q) \tag{3.7}$$

$$S_{\mathrm{ca}}(q) = F_{\alpha}(q)\left[\left(\phi_{\beta} - \phi_{\gamma}\right)F_{\alpha+\beta}(q) - \phi_{\beta}F_{\alpha}(q)\right]S(q) \tag{3.8}$$

$$S_{\mathrm{aa}}(q) = \left[\left(\phi_{\beta} - \phi_{\gamma}\right)F_{\alpha+\beta}(q) - \phi_{\beta}F_{\alpha}(q)\right]^2 S(q) + S_{\xi}(q) \tag{3.9}$$

where $F_{\alpha}(q)$ and $F_{\alpha+\beta}(q)$ are, respectively, the scattering amplitudes of region α and region α+β. $S(q)$ is the structure factor and ϕ_i is the volume fraction of the polymer in region i. $S_{\xi}(q)$ in Eq. (3.9) expresses the concentration fluctuations originating from network structures in region γ. If the high concentration region spatially correlated with the crystallites does not exist, $-S_{\mathrm{ca}}(q) = \phi_{\gamma} S_{\mathrm{cc}}(q)$ from $\phi_{\beta} = \phi_{\gamma}$, and the shapes of $S_{\mathrm{cc}}(q)$ and $-S_{\mathrm{ca}}(q)$ agree on the logarithmic plot. However, Figure 3.6 clearly shows that their shapes do not agree with each other, qualitatively indicating the existence of the concentration fluctuations spatially correlated with the crystallites.

The shoulder around q = 0.8 nm^{-1} and the peak around q = 0.3 nm^{-1} in $S_{\mathrm{cc}}(q)$ would reflect the size of the crystallites and the correlation between them, respectively.

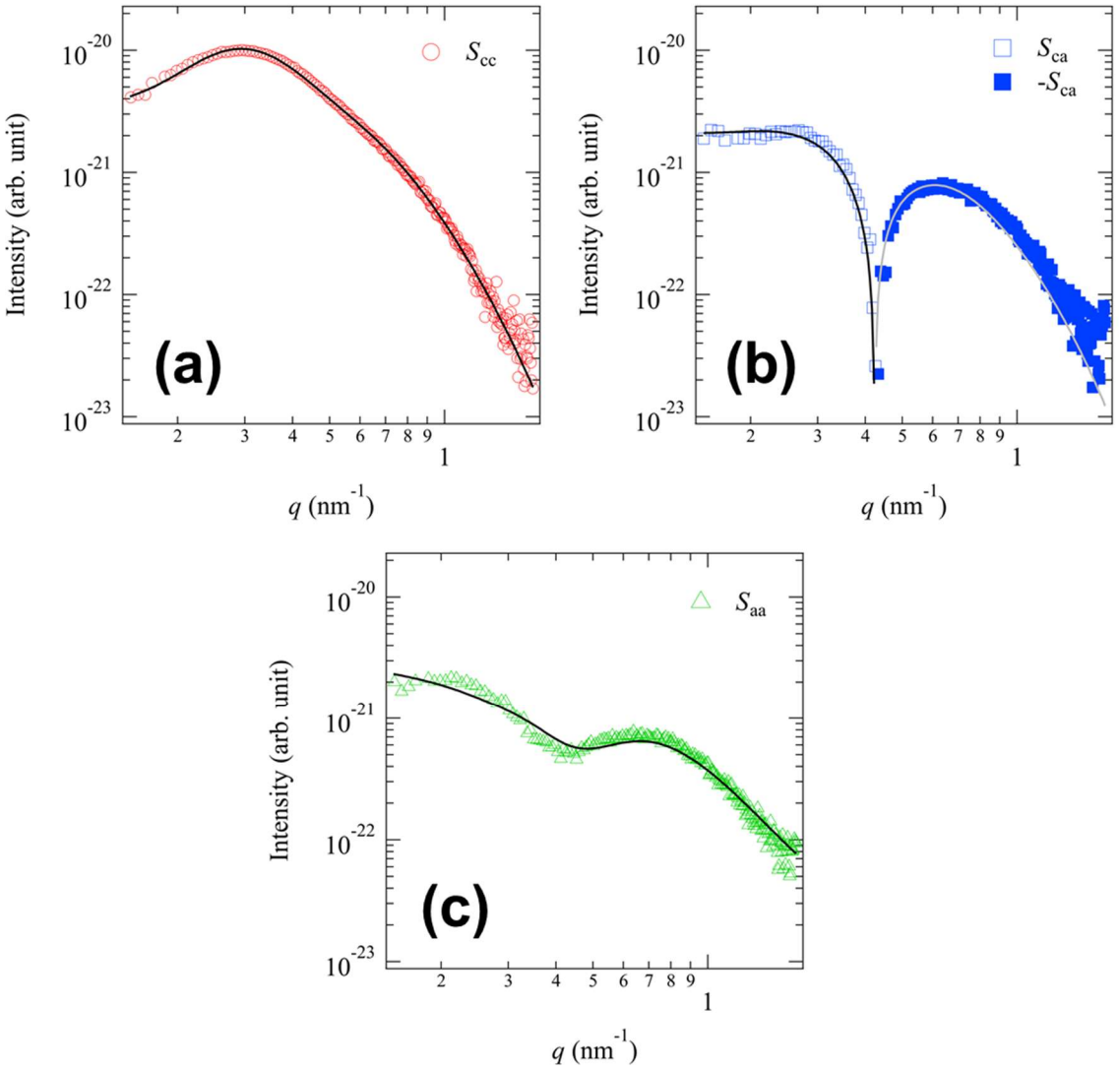

Figure 3.6 Partial scattering functions (a) $S_{cc}(q)$, (b) $S_{ca}(q)$, and (c) $S_{aa}(q)$ of the swollen EOC system, respectively. The solid curves indicate the fitting results with the model functions.

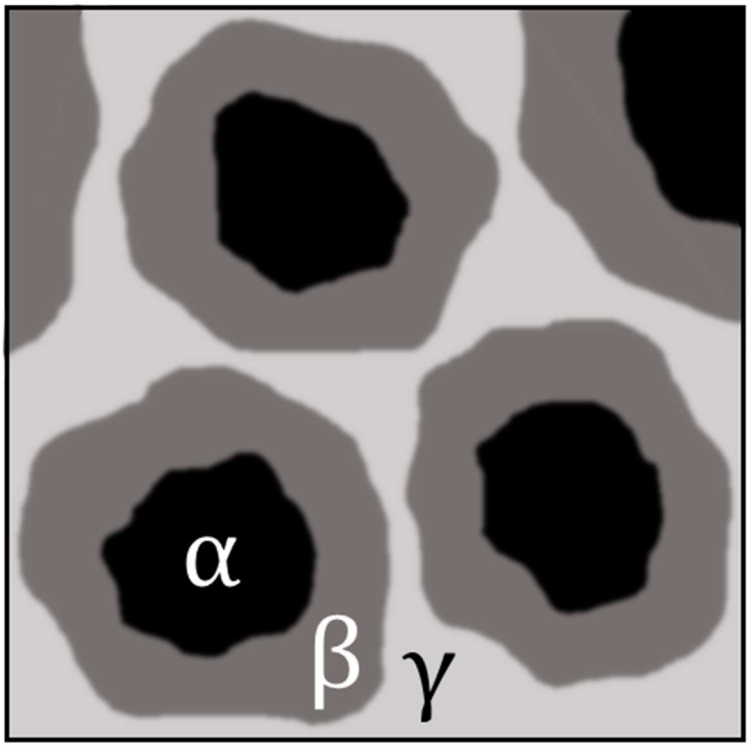

Figure 3.7 Schematic diagram of the model of the swollen EOC system.

The shoulder was broad, so I did not consider a fitting model that specifically describes the shape of the scatterer to be suitable. In addition, the intensity in the larger q region (q > 0.8 nm^{-1}) showed the steeper decrease compared to Porod law ($S_{cc}(q) \sim q^{-4}$). Therefore, I used the unified Guinier/power-law function that includes a parameter characterizing the interfacial thickness as the form factor $F_\alpha^2(q)$ in Eq. (3.7).[27,28]

$$F_\alpha(q)^2 = A\exp\left(-\frac{q^2 {R_{g,\alpha}}^2}{3}\right) + B\left[\mathrm{erf}\left(\frac{qR_{g,\alpha}}{\sqrt{6}}\right)\right]^{12} q^{-4}\exp\left(-q^2{\sigma_{\alpha\beta}}^2\right) \qquad (3.10)$$

where A and B are the prefactors, $R_{g,\alpha}$ is the radius of gyration of the crystallites, and $\sigma_{\alpha\beta}$ is a parameter that characterizes the thickness of the α/β interface $\varepsilon_{\alpha\beta}$. If the

concentration change at the interface follows a Gaussian distribution, $\varepsilon_{\alpha\beta} = \sqrt{2\pi}\sigma_{\alpha\beta}$. The peak was also broad, which probably indicates that the correlation distance was polydisperse. Therefore, I employed the polydisperse Born-Green model for $S(q)$. The Born-Green approximation is one of the approximations that has the closure relationship with the Ornstein-Zernike equation describing the two-body correlation.[29] Recently, McGlasson et al. proposed that the Born-Green approximation is most suitable for a system where the correlation distance follows a normalized distribution function $P(q)$.[30] Using a Gaussian function as $P(q)$, S(q) can be expressed as

$$S(q) = \int_0^\infty P(D_{\mathrm{BG}}) \left[\frac{1}{1 + p_{\mathrm{f}}\theta(q, D_{\mathrm{BG}})}\right] \mathrm{d}D_{\mathrm{BG}} \tag{3.11}$$

$$P(D_{\mathrm{BG}}) = \frac{1}{\sqrt{2\pi}\sigma_{\mathrm{BG}}} \exp\left[\frac{(D_{\mathrm{BG}} - \langle D_{\mathrm{BG}}\rangle)^2}{2{\sigma_{\mathrm{BG}}}^2}\right] \tag{3.12}$$

$$\theta(q, D_{\mathrm{BG}}) = 3\left[\frac{\sin(qD_{\mathrm{BG}}) - qD_{\mathrm{BG}}\cos(qD_{\mathrm{BG}})}{(qD_{\mathrm{BG}})^3}\right] \tag{3.13}$$

where $\langle D_{\mathrm{BG}}\rangle$ is the mean correlation distance, σ_{BG} is the standard deviation of the distribution of correlation distances, and p_{f} is the packing factor. p_{f} is 8 times the packing fraction of hard spheres with the diameter of $\langle D_{\mathrm{BG}}\rangle$, which gives $p_{\mathrm{f}} = 5.92$ at the closest packing. $F_{\alpha+\beta}$ in Eq. (3.8) can also be expressed by the unified Guinier/power-law function as

$$F_{\alpha+\beta}(q)^2 = C\exp\left(-\frac{q^2{R_{\mathrm{g},\alpha+\beta}}^2}{3}\right) + D\left[\mathrm{erf}\left(\frac{qR_{\mathrm{g},\alpha+\beta}}{\sqrt{6}}\right)\right]^{12} q^{-4}\exp\left(-q^2{\sigma_{\beta\gamma}}^2\right) \tag{3.14}$$

where C and D are the prefactors, $R_{\mathrm{g},\alpha+\beta}$ is the radius of gyration of region α+β, and $\sigma_{\beta\gamma}$ is a parameter characterizing the thickness of the β/γ interface $\varepsilon_{\beta\gamma}$ ($= \sqrt{2\pi}\sigma_{\beta\gamma}$). I

employed a Lorentz function for $S_\xi(q)$ in Eq. (3.9) expressed by

$$S_\xi(q) = \frac{S_{\xi,0}}{1 + q^2\xi^2} \tag{3.15}$$

where $S_{\xi,0}$ is the prefactor, and ξ is the correlation length of the polymer network.[11,14,31]

The solid curves in Figure 3.6 indicate the fitting results. The model functions described above were well fitted to the experimental $S_{ij}(q)$. The obtained parameters are listed in Table 2.2. The size of the crystallites ($2R_{g,\alpha}$) was 8.7 nm, and their mean correlation distance $\langle D_{BG} \rangle$ was 16.8 nm under solvent swelling. The high concentration region (region β) existed around the crystallites, and the size of the region α+β ($R_{g,\alpha+\beta}$) was 16.9 nm ≅ $\langle D_{BG} \rangle$. Therefore, the crystallites would form a network structure via the region β. This interpretation is also supported by the fact that the packing fraction ($p_f/8$ = 0.615) agreed well with one at random packing. Unexpectedly, ϕ_β converged to 1, indicating that a region existed in the region β that was not swollen by the solvents. Note that not all of the region β is the non-swollen amorphous layer because the α/β and β/γ interface with a finite thickness ($\varepsilon_{\alpha\beta}$ and $\varepsilon_{\beta\gamma}$, respectively) affects $R_{\alpha+\beta}$. The α/β interface with a finite thickness $\varepsilon_{\alpha\beta}$ is the so-called transition layer, which would not be affected by solvent swelling. Subtracting the contribution of these interfacial layers, the thickness of the non-swelling layer t_{nsw} was obtained as

$$t_{nsw} = R_{g,\alpha+\beta} - R_{g,\alpha} - \frac{\varepsilon_{\alpha\beta}}{2} - \frac{\varepsilon_{\beta\gamma}}{2} = 0.95 \text{ nm} \tag{3.16}$$

Thus, the crystalline-amorphous transition layer with a thickness of 1.86 nm exists around

the pure crystallites, and the non-swelling layer with a thickness of 0.95 nm exists around the transition layer.

Table 3.2 Parameters obtained by fitting

$R_{g,\alpha}$ (nm)	$\varepsilon_{\alpha\beta}$ (nm)	$\langle D_{BG} \rangle$ (nm)	σ_{BG} (nm)	p_f
4.36	1.86	16.8	4.13	4.92
$R_{g,\alpha+\beta}$ (nm)	$\varepsilon_{\beta\gamma}$ (nm)	ϕ_β	ϕ_γ	ξ (nm)	$S_{\xi,0}$
8.48	4.03	1.01	0.09	2.93	1.55×10^{-21}
A	B	C	D		
1.26×10^{-20}	5.86×10^{-22}	5.01×10^{-20}	3.82×10^{-22}		

Let us discuss how the three regions (α, β, and γ) defined in CV-SAXS analysis under solvent swelling correspond to the three components with different mobility (crystalline, rigid amorphous, and melt-like region) obtained by pulsed ^{1}H-NMR without solvent swelling. I have already attributed the component with the lowest mobility to the crystalline region, or the region α. I attribute the rigid amorphous component to the non-swollen amorphous layer, or a part of the region β, and the melt-like component to the swollen amorphous region, or the other part of the region β and region γ. Using the volume crystallinity of EOC $\phi_{c,den}$ (= 21 %) and the parameters obtained by CV-SAXS, the volume fractions of non-swollen and swollen regions ($\phi_{nsw,SAXS}$ and $\phi_{sw,SAXS}$, respectively) without solvent swelling can be estimated as

$$\phi_{nsw,SAXS} = \left\{ \left[\frac{\left(R_{g,\alpha+\beta} - \varepsilon_{\beta\gamma}/2 \right)}{R_{g,\alpha}} \right]^3 - 1 \right\} \times \phi_{c,dens} = 46\ \% \tag{3.17}$$

$$\phi_{sw,SAXS} = 100 - \phi_{c,dens} - \phi_{nsw,SAXS} = 33\ \% \tag{3.18}$$

The results of the calculation are listed in Table 2.3. The volume fractions of each component calculated from the density and CV-SAXS roughly agreed with those obtained by pulsed ^{1}H-NMR, respectively. Thus, I concluded that the rigid amorphous region exists surrounding the crystallites and is not swollen by the solvent.

Table 3.3 Estimated volume fraction of each component in the EOC without solvent swelling (%)

	Crystalline region	Rigid amorphous region	Melt-like region
By pulsed ^{1}H-NMR	17	50	33
By density and CV-SAXS	21	46	33

3.3.5 Comparison with CV-SANS

Using Eq. (3.5), the experimental $S_{ij}(q)$ by CV-SAXS, and the neutron SLD, I calculate $I(q)$ that will be obtained by the CV-SANS, and discuss the precision required for the measurements.

Figure 3.8(a) shows the SLD in the case of CV-SANS with varying the solvent mixing ratio of deuterated Et-tol (*d*-Et-tol) and Et-tol. Under any mixing ratio, no matching points appear. In such a case, $I(q)$ monotonically varies depending on the volume fraction of *d*-Et-tol at every q. Figure 3.8(c) shows $I(q)$ of the EOC swollen by Et-tol and *d*-Et-tol (0/100 and 100/0 in the figure, respectively). The solid curve in the figure indicates the $I(q)$ of 0/100 multiplied by a constant. The superposition of them indicates that the shape of $I(q)$ hardly changes by solvent mixing ratio. It would be impossible to experimentally evaluate the slight difference in the shape and calculate $S_{ij}(q)$. The reason for this situation is that the crystalline and amorphous phase give little contrast in SANS. The SLD of polyolefins is close to zero, as shown in Figure 3.8(a).

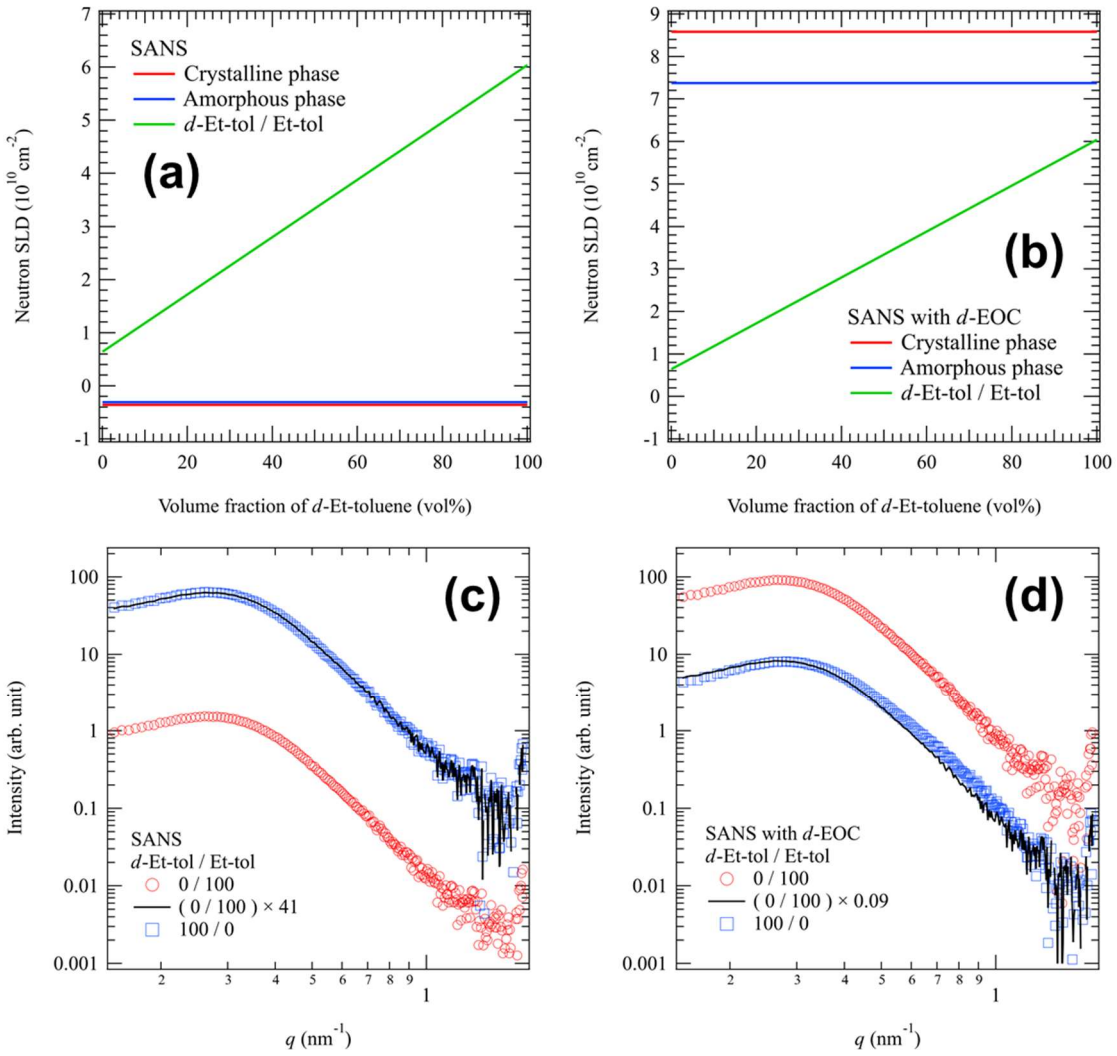

Figure 3.8 Dependence of the *d*-Et-tol/Et-tol mixing ratio on the neutron SLD of the solvent and (a) the EOC and (b) the *d*-EOC, respectively. (c) and (d) SANS profiles simulated with Eq. (3.5), the experimental $S_{ij}(q)$ by CV-SAXS, and the neutron SLD shown in (a) and (b), respectively.

Figure 3.8(b) shows the SLD of the deuterated EOC (*d*-EOC) and the *d*-Et-tol/Et-tol mixture. No matching points appear in this case either. Figure 3.8(d) shows $I(q)$ of the *d*-EOC swollen by the solvent with the mixing ratio of 0/100 and 100/0, and the shifted $I(q)$ of 0/100. In this case, the difference in the SLD between the crystalline and amorphous phase is larger, so the change in the shape of $I(q)$ with solvent mixing ratio is slightly larger than that in the case of the EOC. However, the decomposition into the partial scattering functions would require the measurement with extremely high precision.

From the above discussion, I concluded that the CV-SAXS is the best way to separate the spatial distribution of the crystalline and amorphous phase in polyolefins.

3.4 Conclusion

To elucidate the spatial distribution of the amorphous region with reduced mobility, I performed pulsed ^{1}H-NMR and CV-SAXS for the EOC under solvent swelling. I was able to separate the spatial distribution of the crystalline and amorphous regions by calculating the partial scattering functions. Fitting indicated that a non-swollen amorphous layer existed surrounding the crystallites. The volume fractions of the crystalline, non-swollen amorphous, and swollen amorphous region estimated from CV-SAXS roughly agreed with those of the crystalline, rigid amorphous, and melt-like region determined by pulsed ^{1}H-NMR, respectively. In summary, I first revealed the spatial distribution of the amorphous region constrained by the polymer crystallites.

References

1. Strobl, G., The Physics of Polymers. *Springer-Verlag Berlin Heidelberg* **2007**.
2. Strobl, G., *Prog. Polym. Sci.* **2006,** *31*, 398-442.
3. Hertlein, C.; Saalwächter, K.; Strobl, G., *Polymer* **2006,** *47*, 7216-7221.
4. Schick, C.; Wurm, A.; Mohamed, A., *Colloid Polym. Sci.*. **2001,** *279*, 800-806.
5. Wunderlich, B., *Prog. Polym. Sci.* **2003,** *28*, 383-450.
6. Schick, C.; Dobbertin, J.; Pötter, M.; Dehne, H.; Hensel, A.; Wurm, A.; Ghoneim, A.; Weyer, S., *J. Therm. Anal. Calorim.* **1997,** *49*, 499-511.
7. Ishida, Y.; Yamafuji, K.; Ito, H.; Takayanagi, M., *Kolloid Z. u. Z. Polym.* **1962,** *184*, 97-108.
8. Strobl, G., *Eur. Phys. J. E* **2000,** *3*, 165-183.
9. Häfele, A.; Heck, B.; Kawai, T.; Kohn, P.; Strobl, G., Crystallization of a poly(ethylene-co-octene): I A precursor structure and two competing mechanisms. *Eur. Phys. J. E* **2005,** *16*, 207-216.
10. Endo, H.; Schwahn, D.; Cölfen, H., *J. Chem. Phys.* **2004,** *120*, 9410-9423.
11. Endo, H.; Miyazaki, S.; Haraguchi, K.; Shibayama, M., *Macromolecules* **2008,** *41*, 5406-5411.
12. Takenaka, M.; Nishitsuji, S.; Amino, N.; Ishikawa, Y.; Yamaguchi, D.; Koizumi, S., *Macromolecules* **2009,** *42*, 308-311.
13. Takenaka, M.; Nishitsuji, S.; Watanabe, Y.; Yamaguchi, D.; Koizumi, S., *J. Appl. Crystallogr.* **2021,** *54*, 949-956.
14. Mashita, R.; Kishimoto, H.; Inoue, R.; Kanaya, T., *Polym J* **2016,** *48*, 239-245.
15. Shinohara, Y.; Seike, H.; Kishimoto, H.; Tamenori, Y.; Amemiya, Y., *Polymer* **2016,** *105*, 368-377.

16. Powles, J. G.; Strange, J. H., *Proc. Phys. Soc.* **1963,** *82*, 6-15.

17. Folland, R.; Charlesby, A., *Polymer* **1979**, *20*, 207-210.

18. Tanaka, H.; Nishi, T., *J. Chem. Phys.* **1986,** *85*, 6197-6209.

19. Flory, P. J.; Jr., J. R., *J. Chem. Phys.* **1943,** *11*, 521-526.

20. Hiemenz, P. C.; Lodge, T. P., *Polymer chemistry*. CRC press: 2007.

21. Orwoll, R. A., *J. Am. Chem. Soc.* **1967,** *89*, 6814-6822.

22. Premphet, K.; Paecharoenchai, W., *J. Appl.Polym. Sci.* **2002,** *85*, 2412-2418.

23. Henke, B. L.; Gullikson, E. M.; Davis, J. C., *Atomic data and nuclear data tables* **1993,** *54*, 181-342.

24. Wunderlich, B., Molecular Physics, Vol. 3, Melting. Academic, New York: 1980.

25. Bensason, S.; Minick, J.; Moet, A.; Chum, S.; Hiltner, A.; Baer, E., *J. Polym. Sci. Part B: Polym. Phys.* **1996,** *34*, 1301-1315.

26. Kishimoto, M.; Mita, K.; Ogawa, H.; Takenaka, M., *Macromolecules* **2020,** *53*, 9097-9107.

27. Beaucage, G., *J. Appl. Crystallogr.* **1995,** *28*, 717-728.

28. Ruland, W., *J. Appl. Crystallogr.* **1971,** *4*, 70-73.

29. Guinier, A.; Fournet, G.; Yudowitch, K. L., Small-angle scattering of X-rays. **1955**.

30. McGlasson, A.; Rishi, K.; Beaucage, G.; Chauby, M.; Kuppa, V.; Ilavsky, J.; Rackaitis, M., *Macromolecules* **2020,** *53*, 2235-2248.

31. Kanaya, T.; Takeshita, H.; Nishikoji, Y.; Ohkura, M.; Nishida, K.; Kaji, K., *Supramol. Sci.* **1998,** *5*, 215-221.

Chapter 4
Effect of Stress Field on the Mechanical Behavior of PE

4.1 Introduction

Polyethylene (PE) is one of the most widely used polymers in daily life owing to its excellent mechanical properties and processability. In this study, I first observed changes in the structures in PE that are on the order of 100 nm to 1 μm (submicron scale) by using time-resolved ultra-small-angle X-ray scattering (USAXS) and show that the changes on the submicron scale dominate the mechanical behavior of PE under uniaxial stretching.

It is well known that crystals in PE form hierarchical structures, as shown in Figure 1.1. The structures include crystalline lattice structures, where molecular chains are systematically folded and packed; lamellar structures, where crystalline and amorphous phases are alternately stacked; branch structures formed by the lamellar structure; and spherulitic structures filled with the branch structure. The changes in the hierarchical structures under deformation induce a yield point (YP) in stress-strain (S-S) curves under uniaxial stretching of PE at room temperature (cold drawing). Some LLDPEs exhibit two YPs in the S-S curve, although one YP is usually observed in the S-S curve during cold drawing.[1]

Researchers have thought that the yielding behaviors originate from the so-called "slip" behaviors in the lamellar structures. The slips are categorized as interlamellar slip and intralamellar slip.[1-7] During interlamellar slip, only amorphous phases in the lamellar structures are deformed by stretching, and slip deformation between crystalline phases

occurs. Intralamellar slip is further categorized as fine slip and coarse slip. Coarse slip describes the fragmentation of the crystalline phases into mosaic blocks. Fine slip corresponds to homogeneous block shearing, which leads to transformation into a metastable phase, or monoclinic phase. The intralamellar slip facilitates the chains in the crystalline phases becoming oriented parallel to the stretching direction in contrast to the interlamellar slip.

To clarify the relationship between the YPs and the slip behaviors, Butler et al. have investigated the changes in the lamellar and lattice structures of PE that showed two YPs during uniaxial stretching by time-resolved small- and wide-angle X-ray scattering (SAXS and WAXS, respectively).[6] They found the formation of monoclinic phase at the first YP (1YP) by WAXS and concluded that the 1YP originated from the fine slip. Brooks et al. and Gaucher-Miri and Séguéla also obtained the same results for the origin of 1YP.[2,3] Hiss et al. suggested that the cooperative action of the fine slip was needed for the 1YP.[4] As for the second YP (2YP), Butler et al. observed the disappearance of the SAXS peak parallel to the stretching direction at the 2YP. The disappearance indicated that the stacking of lamellar structures parallel to the stretching direction was deformed by the coarse slip and Butler et al. concluded that the origin of the 2YP is the coarse slip. Brooks et al. and Gaucher-Miri and Séguéla also came to the same conclusion, while Hiss et al. did not associate the 2YP with any mechanism of plastic flow. Thus, the researchers have concluded that the 1YP and 2YP were attributed to fine slip and coarse slip, respectively. However, the researchers have not investigated the effects of the changes in the structures on the submicron scale on the yielding behaviors, so the changes need to be investigated since it is expected that the structures on the submicron scale would also affect the yielding behaviors.

The USAXS technique that uses synchrotron radiation enables us to perform in situ observations on the submicron scale.[8-10] By using USAXS, Takenaka et al. previously discovered that a particular scattering pattern, referred to as an “abnormal” butterfly

pattern, appears in PE around the YP under uniaxial stretching, indicating that inhomogeneous deformation occurs on the submicron scale.[11-13]

In this chapter, I investigated the changes in the structures on the submicron scale of PE during uniaxial stretching by time-resolved USAXS as well as changes in the lamellar structures and lattice structures by time-resolved SAXS and WAXS. Then, I clarified how the changes in the structures on the submicron scale affect the yielding behaviors.

4.2 Experimental Section

4.2.1 Sample Preparation

LLDPE and HDPE were used in this chapter. The characterization of the materials is listed in Table 4.1. Sheets of each material were made by press machines with the following conditions. Two press machines (MINI TEST PRESS-10, TOYOSEIKI) were used. One was set at 180 °C, where the pellets were melted by pressing them in a 2-mm-thick mold for 10 min. Then, they were quenched by transferring them to the other machine set at 20 °C. Sandglass-shaped specimens with a center width of 2 mm were punched out from the sheets.

Table 4.1 Characterization of the Materials Used Herein

name	M_w[a]	M_w/M_n[a]	density of the sheet at 20°C[b]	comonomer species
LLDPE (H935)	2.1×10^5	5.3	0.937 g/cm^3	4-methylpentene-1
HDPE	2.3×10^5	11.9	0.962 g/cm^3	-

a. Determined by gel permeation chromatography (Viscotek Triple Detector HT-GPC Model-SG system, Malvern Instruments Ltd.) to be polystyrene-equivalent values at Northeastern Industrial Research Center of Shiga Prefecture, Shiga, Japan.
b. Measured by helium pycnometer (AccuPyc 1330, Shimadzu).

4.2.2 USAXS, SAXS, and WAXS Measurements

In situ X-ray scattering measurements were performed during tensile testing

using a homemade tensile tester. The tensile speed was 1 mm/min. During the measurements, I confirmed that the X-ray beam always irradiated the center of the specimens with a camera. The USAXS measurements were performed with an incident wavelength of 2.0 Å in the second hutch of beamline BL03XU at SPring-8, Hyogo, Japan.[14] Pilatus was used as a detector. The camera length and exposure time for the LLDPE were 7.5 m and 850 ms, respectively. The HDPE measurements were performed with a specimen-to-detector distance of 7.9 m using a 100 μm thick Al plate as an attenuator. The exposure time was 900 ms. The simultaneous SAXS and WAXS measurements were performed on the same beamline as the USAXS measurements. For the LLDPE, a 10 μm thick Au plate was used as the attenuator, and the incident wavelength was 1.0 Å. The specimen-to-detector lengths, exposure times, and detectors for the SAXS/WAXS measurements were 2.4 m/119 mm, 330 ms/330 ms, and Pilatus/a flat panel detector, respectively. For the HDPE, a 10-μm-thick Au plate was used as the attenuator, and the incident wavelength was 0.8 Å. The specimen-to-detector lengths, exposure times, and detectors were 2.4 m/120 mm, 670 ms/570 ms, and Pilatus/Sophias for the SAXS/WAXS measurements, respectively.

For the data analysis, the two-dimensional (2D) scattering intensities obtained without the specimens were subtracted from the intensities obtained with them in consideration of the transmittances of X-rays obtained by the ion chambers installed before and after the specimens. Finally, the intensities were divided by the thickness of the specimens. The thickness during stretching was calculated using the thickness before stretching and Lambert–Beer's law.

4.3 Results and Discussion

4.3.1 S-S Curves

The S-S curves obtained during the USAXS measurements are shown in Figure 4.1. The strain λ is defined as:

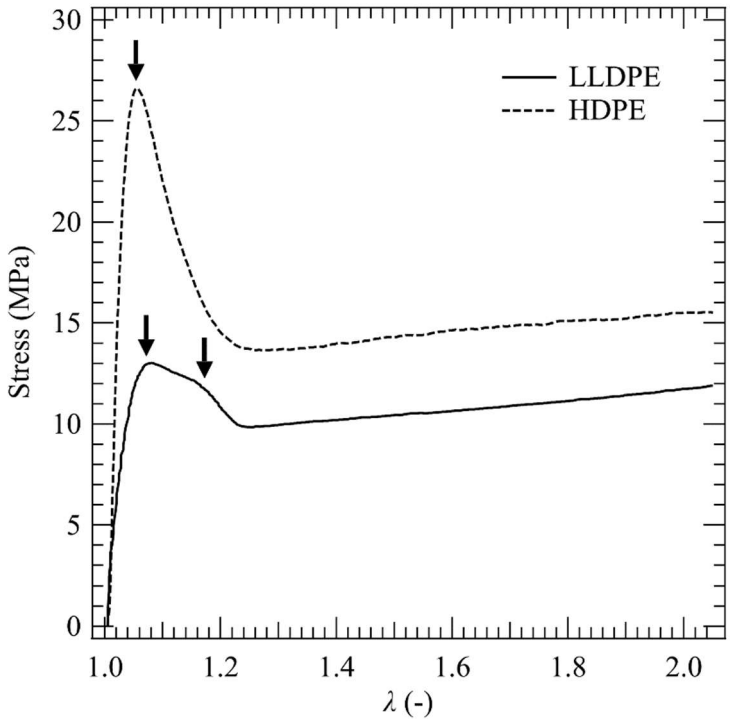

Figure 4.1 S-S curves of the LLDPE and HDPE. The arrows indicate the yield points.

$$\lambda = \frac{L}{L_0} \tag{4.1}$$

where L_0 and L are the chuck distances before and after applying strain, respectively. The stress is the engineering stress. Two yield points at λ = 1.07 and 1.17 were observed for the LLDPE, while one yield point at λ = 1.05 was observed for the HDPE. Necks were generated at the center of the specimens (area irradiated with X-rays) immediately after passing over the 2YP of the LLDPE and the YP of the HDPE. Whitening also occurred in the HDPE at the onset of necking. Owing to the shape of the specimens, the propagation of the necking was very limited and hardly observable on either specimen. The incident X-rays always irradiated the necks after their appearance, so that the scattering patterns reflected the necking process.

4.3.2 Analyses of Hierarchical Structures before Stretching

Figures 4.3(a) and 4.10(a) show the 2D USAXS patterns for the LLDPE and HDPE, respectively, before stretching (λ = 1.00). Both patterns were isotropic, and the 2D SAXS and WAXS patterns for the LLDPE (Figures 4.3(i) and (q), respectively) and HDPE (Figures 4.10(i) and (q), respectively) were also isotropic, indicating that anisotropy in the hierarchical structures was not induced in the preparation processes. I averaged the 2D patterns and estimated characteristic parameters from the obtained scattering profiles. Figure 4.2(a) shows the combined USAXS and SAXS profiles for both specimens. Here, q is the magnitude of the scattering vector $\boldsymbol{q}$ defined by $q = (4\pi/\lambda_{X\text{-}ray})\sin(\theta/2)$, where $\lambda_{X\text{-}ray}$ and θ are the wavelength of the incident X-rays and the scattering angles, respectively.

The profiles in the region of $q < 0.015$ nm^{-1} showed the following power laws: $I(q) \propto q^{-2.7}$ for LLDPE and $I(q) \propto q^{-2.4}$ for HDPE. The results suggest that submicron-scale density fluctuations with mass fractal dimensions (D_m) of 2.7 and 2.4 existed in the LLDPE and HDPE, respectively.

At approximately $q = 0.2$ nm^{-1}, peaks derived from the lamellar structures were observed for both specimens. The peaks from the HDPE were clearer than those from the LLDPE, indicating that the regularity of the lamellar structures in the HDPE was higher than that in the LLDPE. One-dimensional correlation functions were calculated from the scattering profiles for both specimens, and I estimated the long spacing (d_{ac}) and crystal thickness (d_c) from the correlation functions.[15]

In the WAXS profiles (Figure 4.2(b)), reflections from the (110) and (200) lattice planes in the orthorhombic phase were observed, and I calculated the crystallinity (W_c) values. The obtained parameters are listed in Table 4.2. The parameters clarified that the HDPE had a higher crystallinity than the LLDPE.

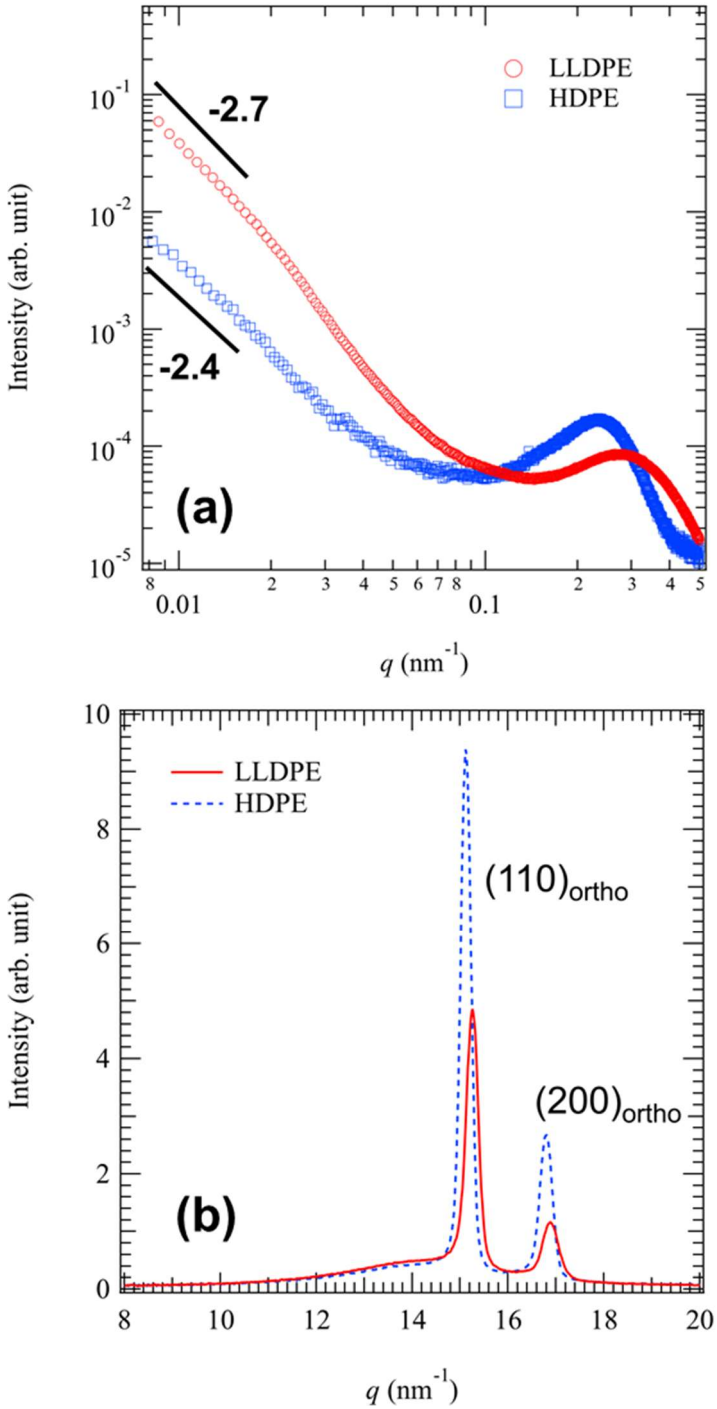

Figure 4.2 (a) Combined USAXS/SAXS profiles and (b) WAXS profiles of the LLDPE and HDPE before stretching (λ = 1.00).

Table 4.2 Characteristic Parameters of the LLDPE and HDPE Before Stretching ($\lambda = 1.00$)

name	D_m (-)	d_{ac} (nm)	d_c (nm)	W_c (wt%)
LLDPE	2.7	15.8	6.21	36.0
HDPE	2.4	22.6	13.4	58.9

4.3.3 Changes in the Hierarchical Structures in the LLDPE

Figure 4.3 shows the changes in the 2D USAXS, SAXS, and WAXS patterns as a function of strain for the LLDPE, and Figure 4.4 shows the combined USAXS and SAXS profiles for the LLDPE along the directions parallel and perpendicular to the stretching axis. The profiles $I_{||}(q)$ along the parallel direction were obtained by sector averages for $85° < \mu < 95°$ and $265° < \mu < 275°$, while the profiles $I_{\perp}(q)$ along the perpendicular direction were for $-5° < \mu < 5°$ and $175° < \mu < 185°$. The definition of the azimuthal angle μ is shown in Figure 4.3(b).

The changes in the scattering patterns with strain can be divided into the following four regions. Region I occurs before the 1YP or when $\lambda < 1.07$, Region II occurs between the 1YP and 2YP or when $1.07 < \lambda < 1.17$, Region III occurs after the 2YP and the formation of necking or when $1.17 < \lambda < 1.30$, and Region IV occurs upon the formation of a fibrillar structure or when $1.30 < \lambda$.

Region I

In Region I ($\lambda < 1.07$), strain induced affine deformation in the hierarchical structure of the LLDPE. The USAXS patterns of the LLDPE (Figures 4.3(a)–(c)) hardly changed with strain; as the same is true for the SAXS patterns (Figures 4.3(i)–(k)) in Region I. In the $q < 0.05$ nm^{-1} region on the combined USAXS and SAXS profiles in Figures 4.4(a) and (e), $I_{||}(q)$ and $I_{\perp}(q)$ shifted to smaller and larger q, respectively, with the strain. The changes in the profiles in the small q-region indicate that the submicron structure was elongated along the parallel direction.

The peak positions of $I_{||}(q)$ and $I_{\perp}(q)$ also shifted toward smaller q and toward

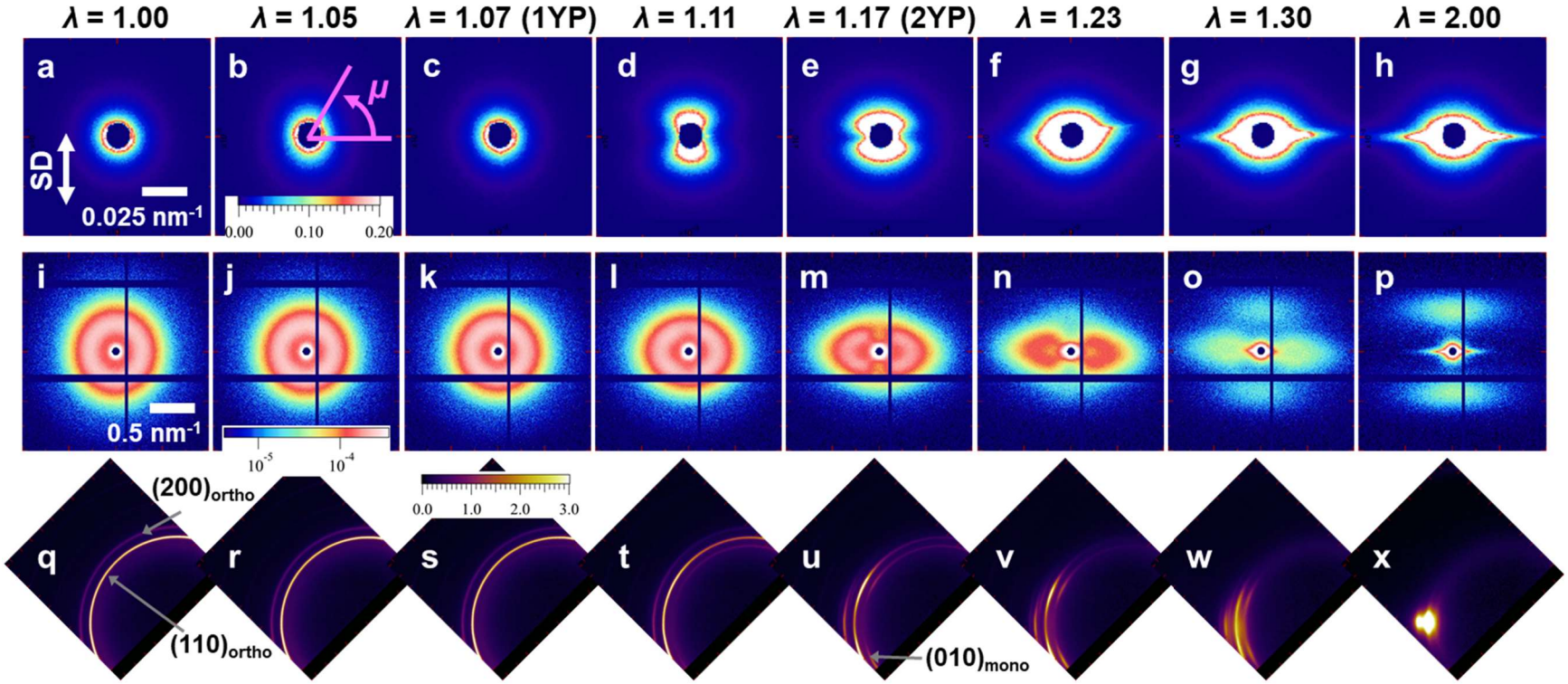

Figure 4.3 (a)-(h) USAXS, (i)-(p)SAXS, and (q)-(x)WAXS 2D patterns of the LLDPE with strain. The arrow in part(a) corresponds to the stretching direction.

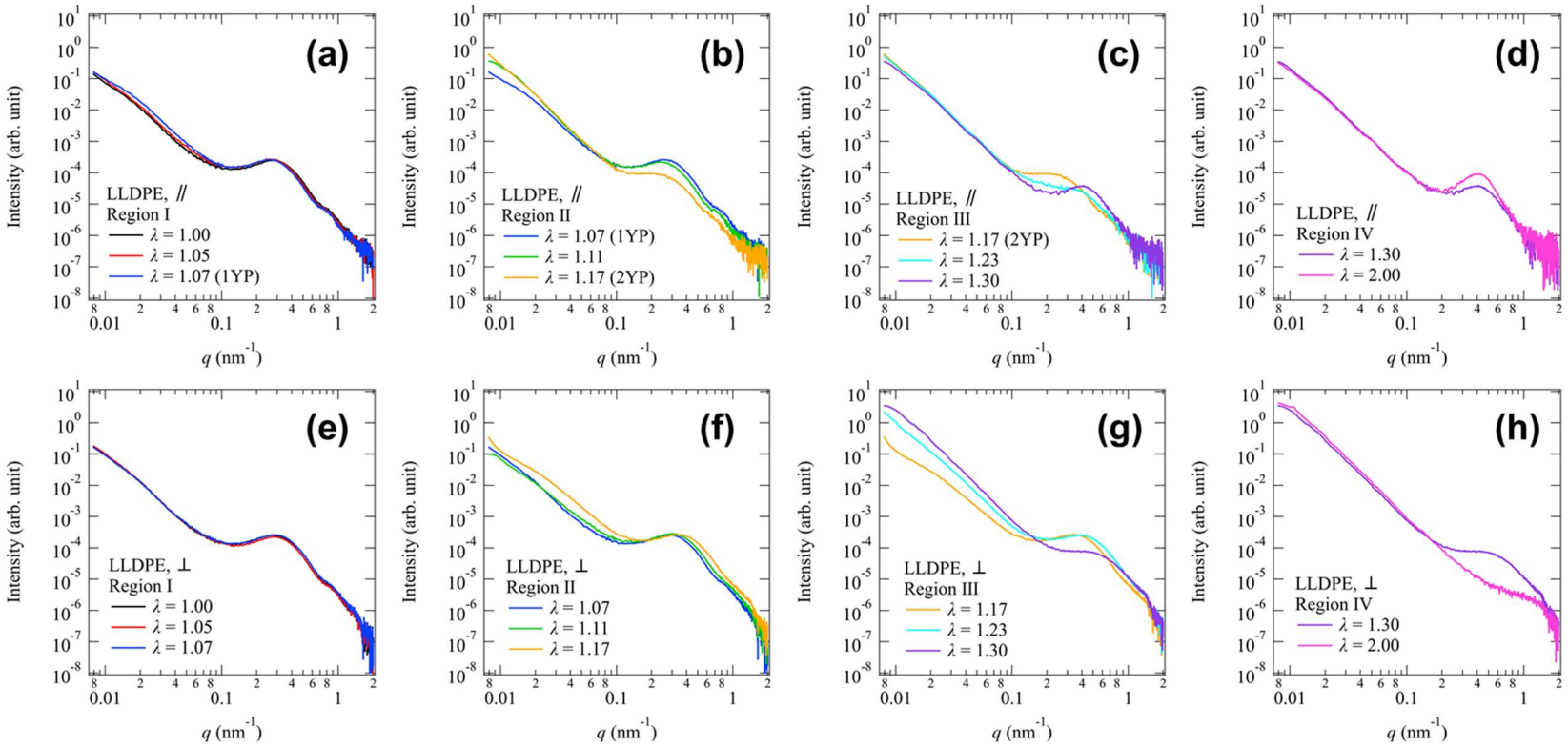

Figure 4.3 Combined USAXS and SAXS profiles of the LLDPE in (a) and (e) Region I, (b) and (f) Region II, (c) and (g) Region III, and (d) and (h) Region IV, respectively. The profiles in (a), (b), (c) and (d) and (e), (f), (g), and (h) correspond to the scattering intensities parallel and perpendicular to the stretching directions, respectively.

larger q, respectively, with the strain. The long spacings along the parallel ($D_{||}$) and perpendicular ($D_{\perp}$) directions were calculated from the following equation:

$$D_i = \frac{2\pi}{q_{\mathrm{m},i}} \quad i = \parallel, \perp \tag{4.2}$$

where $q_{\mathrm{m},||}$ and $q_{\mathrm{m},\perp}$ are the peak positions. I obtained $q_{\mathrm{m},||}$ and $q_{\mathrm{m},\perp}$ by fitting $I_{||}(q)$ and $I_{\perp}(q)$, respectively, to a linear combination of a power law and Gaussian function. The ratios $D_{\mathrm{i}}(\lambda)/D_{\mathrm{i}}(1)$ were plotted against λ in Figure 4.5. The solid and dashed lines in the Figure are calculated by the following equations obeying affine deformation:

$$\frac{D_{\parallel}(\lambda)}{D_{\parallel}(1)} = \lambda \tag{4.3}$$

$$\frac{D_{\perp}(\lambda)}{D_{\perp}(1)} = \lambda^{-\frac{1}{2}} \tag{4.4}$$

As shown in Figure 4.5, the change in the long spacing of the LLDPE followed affine deformation in Region I.

Figure 4.6(a) shows the change in the μ dependence of the reduced peak intensity $I_{\mathrm{m,SAXS}}(\mu, \lambda)/I_{\mathrm{m,SAXS}}(\mu, 1)$ of SAXS patterns in Region I. I fitted sector averages at every 10° to the same function as above and plotted the obtained front factors of the Gaussian function against μ. At first, $I_{\mathrm{m,SAXS}}(\mu, \lambda)/I_{\mathrm{m,SAXS}}(\mu, 1)$ increases around $\mu = 90^{\circ}$ with strain, indicating that the lamellar structures are slightly oriented to the direction perpendicular to the strain direction. Then, the peak at $\mu = 45^{\circ}$ and 135° corresponding to the four-point pattern was observed at the 1YP, suggesting that the chevron-type morphology was formed at 1YP, or $\lambda = 1.07$, and the fragmentation and rotation of the lamellar structures by coarse slip occurred even at 1YP.[16,17] The changes in the crystalline lattice structure are characterized by the μ dependences of the reduced diffraction peak intensity $I_{110,\mathrm{ortho}}(\mu, \lambda)/I_{110,\mathrm{ortho}}(\mu, 1)$ as shown in Figure 4.6(b) in Region I. The figure shows the decrease

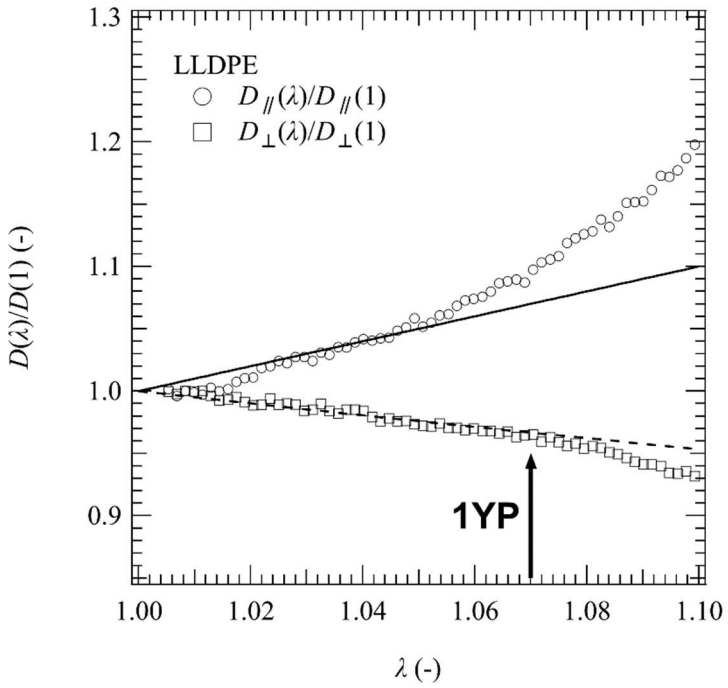

Figure 4.5 λ dependence of $D_{//}(\lambda)/D_{//}(1)$ and $D_{\perp}(\lambda)/D_{\perp}(1)$ of the LLDPE. The solid and dashed lines are the lines calculated by Eqs (5.3) and (5.4) obeying affine deformation.

around $\mu = 90^{\circ}$ and the increase at $\mu = 150^{\circ}$ at $\lambda = 1.07$ (1YP). The increase at $\mu = 150^{\circ}$ in WAXS and at $\mu = 135^{\circ}$ in SAXS implies that fine slip also occurred at the 1YP. Actually, as shown in Figures 4.7(a) and (b), the increase in $(010)_{mono}$ was found at the 1YP, reflecting the formation of monoclinic phase. The monoclinic phase is believed to be transformed by fine slip on the $(110)_{ortho}$ plane.[18] The peak of $(010)_{mono}$ appeared at $\mu = 180^{\circ}$, indicating that the dominant direction of fine slip was perpendicular to the stretching direction. Thus, I concluded that both coarse slip and fine slip occurred at the 1YP.

Region II

In Region II, or the region between the 1YP and 2YP ($1.07 < \lambda < 1.17$), inhomogeneous deformation occurred on the submicron scale, and a chevron-type morphology was developed. In the USAXS patterns (Figures 4.3(c)–(e)), the intensity along the parallel direction increased, and the abnormal butterfly patterns clearly

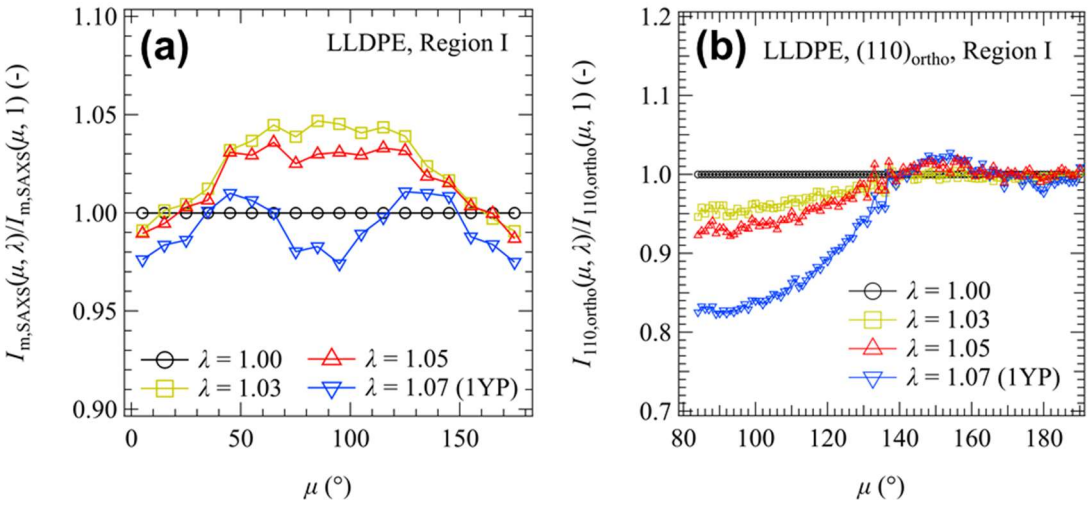

Figure 4.6 μ dependence of (a) the reduced peak intensity $I_{m,SAXS}(\mu, \lambda)/I_{m,SAXS}$ $(\mu, 1)$ of SAXS patterns and (b) $I_{110,ortho}(\mu, \lambda)/I_{110,ortho}(\mu, 1)$ in WAXS patterns in Region I in the LLDPE.

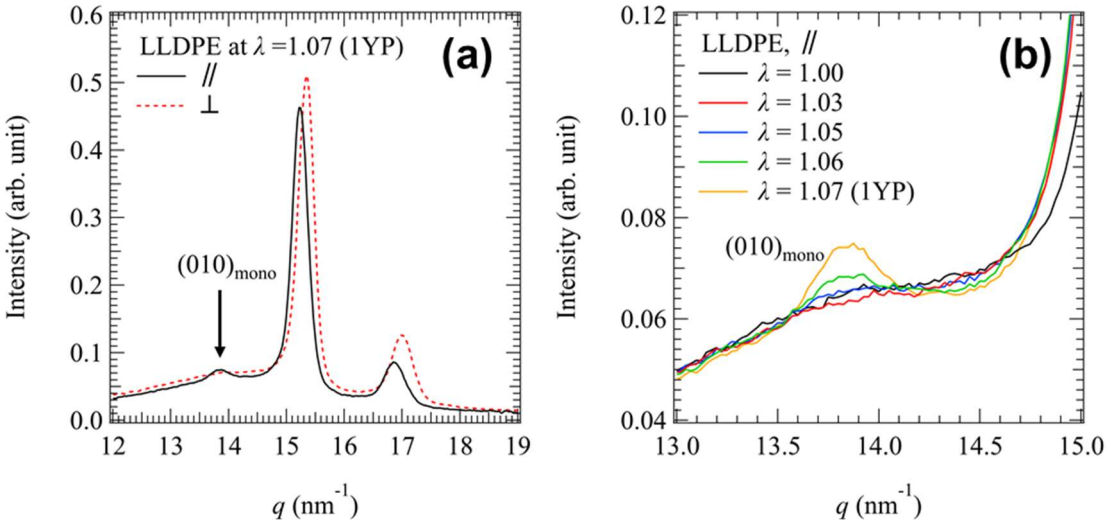

Figure 4.7 (a) WAXS profiles parallel and perpendicular to the stretching directions at λ = 1.07, (b) evolution of the diffraction intensities from the (010) plane in the monoclinic crystals.

appeared. Accordingly, an enhancement in $I_{\parallel}(q)$ was observed in Figure 4.4(b). Abnormal butterfly patterns are observed in materials where internal structures are not deformed homogeneously under uniaxial stretching or simple shear, such as polymer gels[19,20] under uniaxial stretching, semidilute polymer solutions under shearing,[21-24] and rubber filled with inorganic particles under uniaxial stretching.[9-10,25] In the LLDPE case, the interpretation is that the amount of deformation differed between the high-crystallinity region (HCR) and low-crystallinity region (LCR) on the scale of the lamellar branching structures.

On the scale of the lamellar structures (Figures 4.3(k)–(m)), as described above, four-point patterns became distinct with strain. Figure 4.8(a) shows the μ dependence of the peak intensities calculated from the SAXS patterns. Figure 4.8(a) makes it clear that the four-point pattern and the corresponding lamellar fragmentation and rotation were developed after the 1YP. In addition, the intensity of the four-point pattern decreased after the 1YP, indicating that the crystals melted mechanically.[6-7,26]

The $(110)_{ortho}$ peak in the WAXS patterns (Figures 4.3(s)–(u) and 4.8(b)) is also associated with the rotation and oriented in the diagonal direction. On the other hand, the orientation of the $(200)_{ortho}$ peak was developed in the perpendicular directions in Region II, as shown in Figure 4.8(c). The fact that $(200)_{ortho}$ planes were not oriented diagonally but the $(110)_{ortho}$ planes were oriented diagonally indicates that fragmentation occurred on the $(110)_{ortho}$ planes. Also, extra peaks from the $(010)_{mono}$ planes were observed in the smaller q-region. The $(010)_{mono}$ plane was also oriented as with the $(110)_{ortho}$ plane. Thus, the WAXS patterns indicate that both lamellar fragmentation (coarse slip) and fine slip occurred on the $(110)_{ortho}$ plane. The remarkable decrease in the overall intensity after the 1YP in Figures 4.8(b) and (c) also supports the mechanical melting.

Region III

In Region III, voids emerged and elongated along the parallel direction on the submicron scale, and the chevron-type morphology started to transform into a fibrillar

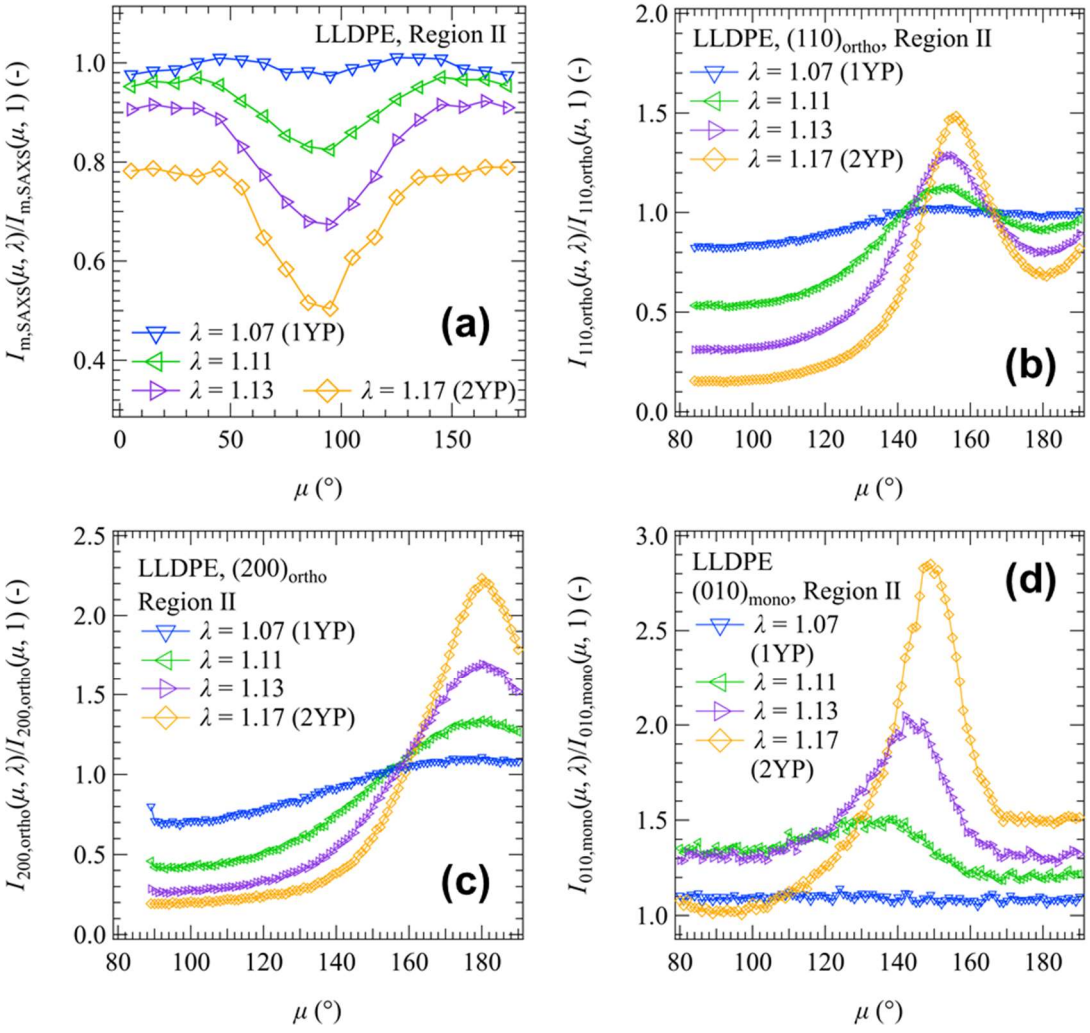

Figure 4.8 μ dependence of (a) the reduced peak intensity $I_{m,SAXS}(\mu, \lambda)/I_{m,SAXS}(\mu, 1)$ of SAXS patterns, (b) $I_{110,ortho}(\mu, \lambda)/I_{110,ortho}(\mu, 1)$, (c) $I_{200,ortho}(\mu, \lambda)/I_{200,ortho}(\mu, 1)$, and (d) $I_{010,mono}(\mu, \lambda)/ I_{010,mono}(\mu, 1)$ in WAXS patterns in Region II in the LLDPE.

structure. In the fibrillar structure, the recrystallized lamellar structure aligned in the parallel direction, and the long spacing was shorter than the original lamellar structures. As shown in Figures 4.3(e)–(g), the USAXS intensity along the perpendicular direction increased, and strong streak scattering appeared along the perpendicular direction. The appearance of voids was clearly observed as an enhancement of $I_{\perp}(q)$ at $0.02 < q < 0.08$ nm^{-1} in Figure 4.4(f). The increase in intensity was observed only in $I_{\perp}(q)$ at $\lambda = 1.17$, so that the shape of the voids is elongated in the strain direction. The elongated voids coarsened in the strain direction by coalescence of the voids, and a string-like shape aligned to the stretching direction was formed, resulting in the appearance of streak scattering. Similar behaviors were observed during the shear-induced phase separation of semidilute polymer solutions by Kume et al.[21] They found a butterfly pattern followed by a streak pattern with increasing shear rate, and their optical microscopy observations clarified that the formation of a string-like structure was the origin of the streak scattering pattern. Since the necking process started at the 2YP, the formation of elongated voids induced it.

At approximately $\lambda = 1.30$ in the SAXS patterns (Figure 4.3(o)), a broad peak appeared at approximately $q = 0.4$ nm^{-1} in the parallel direction, indicating that the recrystallized lamellar structure stacked with short spacings was formed along the parallel direction, as already reported.[4,6,7,17,26-27] The shift of the peak from $q = 0.2$ nm^{-1} of the original lamellar structure to $q = 0.4$ nm^{-1} shown in Figure 4.4(c) originates from the fact that the effective quench depth under strain is smaller than that without strain.

As shown in the WAXS patterns (Figures 4.3(u)–(w)) and μ dependences of the diffraction peaks (Figures 4.9(a) and (b)), the $(110)_{ortho}$ peak corresponding to the four-point pattern decreased while the peak intensity of the $(110)_{ortho}$ and $(200)_{ortho}$ at $\mu = 180°$ increased with strain. The $(010)_{mono}$ reflection also decreased with strain (Figure 4.9(c)). This change also supported the formation of a fibrillar structure.

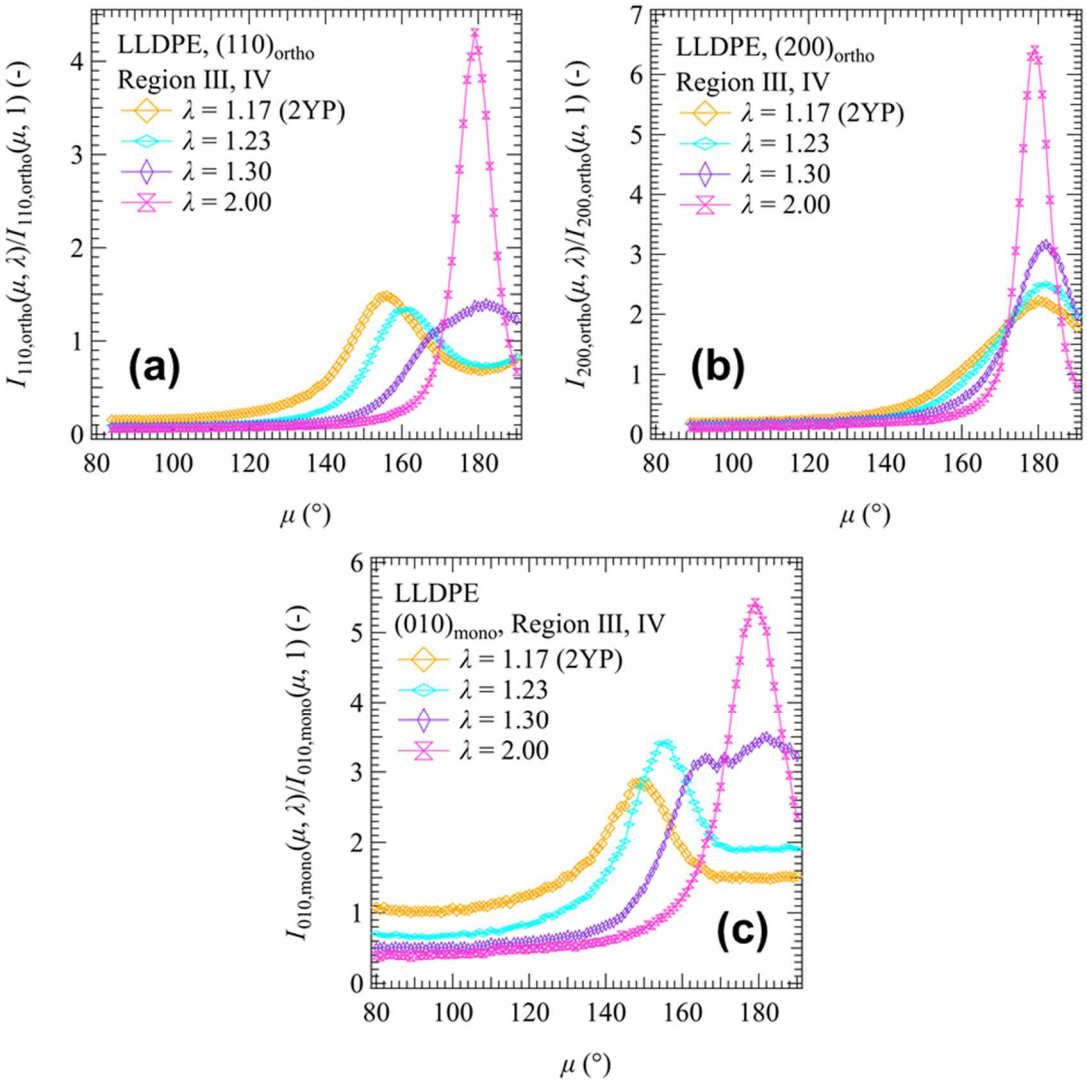

Figure 4.9 μ dependence of (a) $I_{110,ortho}(\mu, \lambda)/I_{110,ortho}(\mu, 1)$, (b) $I_{200,ortho}(\mu, \lambda)/I_{200,ortho}(\mu, 1)$, and (c) $I_{010,mono}(\mu, \lambda)/I_{010,mono}(\mu, 1)$ in WAXS patterns in Regions III and IV in the LLDPE.

Region IV

In Region IV, the USAXS pattern hardly changed with the strain (Figure 4.3(h)), indicating that the elongated voids did not develop substantially. The chevron-type morphology transformed into a fibrillar structure completely. This transition caused the disappearance of the four-point pattern in the SAXS pattern (Figure 4.3(p)). The peaks at μ = 180° in the WAXS patterns increased with the strain, as shown in Figure 4.9, suggesting that the orientation of the lattice structure along the parallel direction progressed with strain.

4.3.4 Changes in the Hierarchical Structures in the HDPE

Figure 4.10 shows the changes in the USAXS, SAXS, and WAXS patterns with strain, and Figure 4.11 shows $I_{\parallel}(q)$ and $I_{\perp}(q)$ for the combined USAXS and SAXS profiles for the HDPE.

The change in the scattering patterns from the HDPE with strain can be divided into the following three regions. Region I contains weak inhomogeneous deformation on the submicron scale and affine deformation of the lamellar structures before the YP or when $\lambda < 1.05$, Region II contains strong inhomogeneous deformation on the submicron scale or when $1.05 < \lambda < 1.21$, and Region III contains formation of the elongated voids and fibrillar structures or when $1.21 < \lambda$.

Region I

In Region I ($\lambda < 1.05$), the strain induced weak inhomogeneous deformation on the submicron scale, while the lamellar structure was deformed with affine deformation.

In the USAXS patterns (Figures 4.10(a)–(c)) and profiles from the HDPE (Figure 4.11(a)), the scattering intensity along the parallel direction increased with strain. The increase in $I_{\parallel}(q)$ in the USAXS region agrees with the inhomogeneous deformation between the HCRs and LCRs, as described above. However, the butterfly pattern was not observed in this region, and the inhomogeneity was not strong. As shown in the SAXS

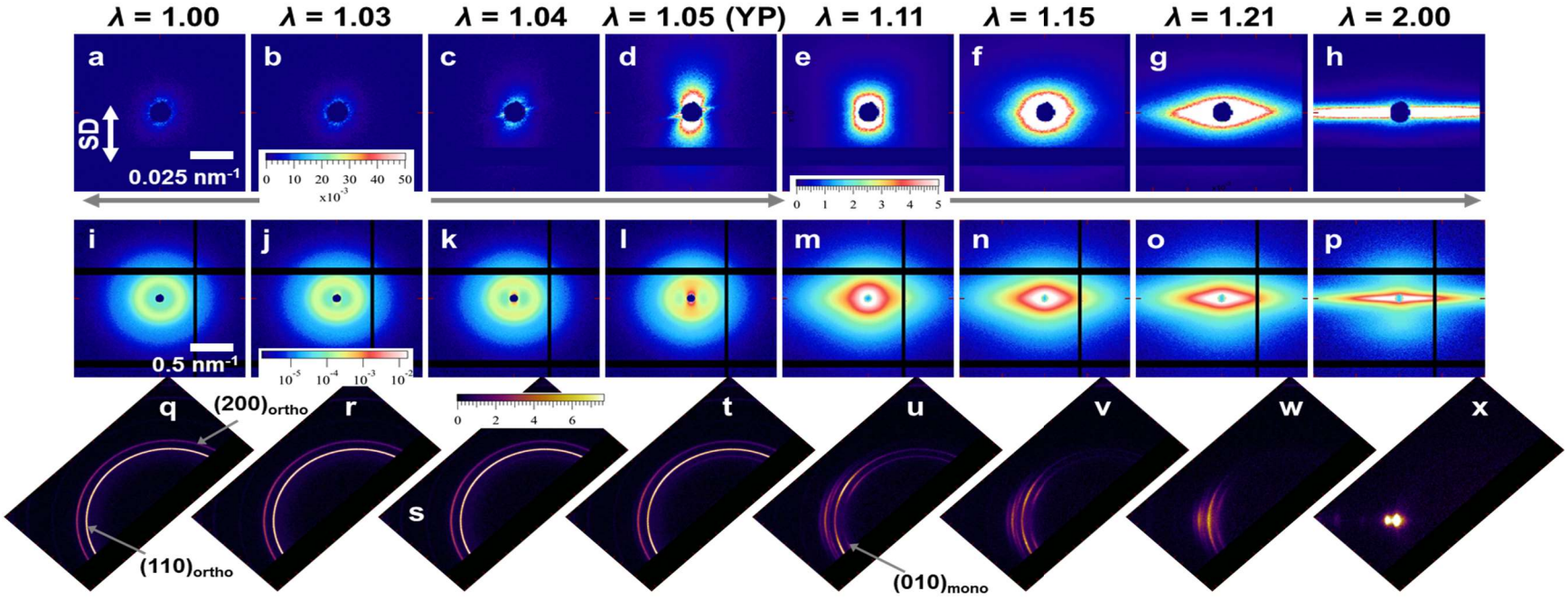

Figure 4.10 (a)–(h) USAXS, (i)–(p)SAXS, and (q)2013(x)WAXS 2D patterns of HDPE with strain. The arrow in part(a) corresponds to the stretching direction.

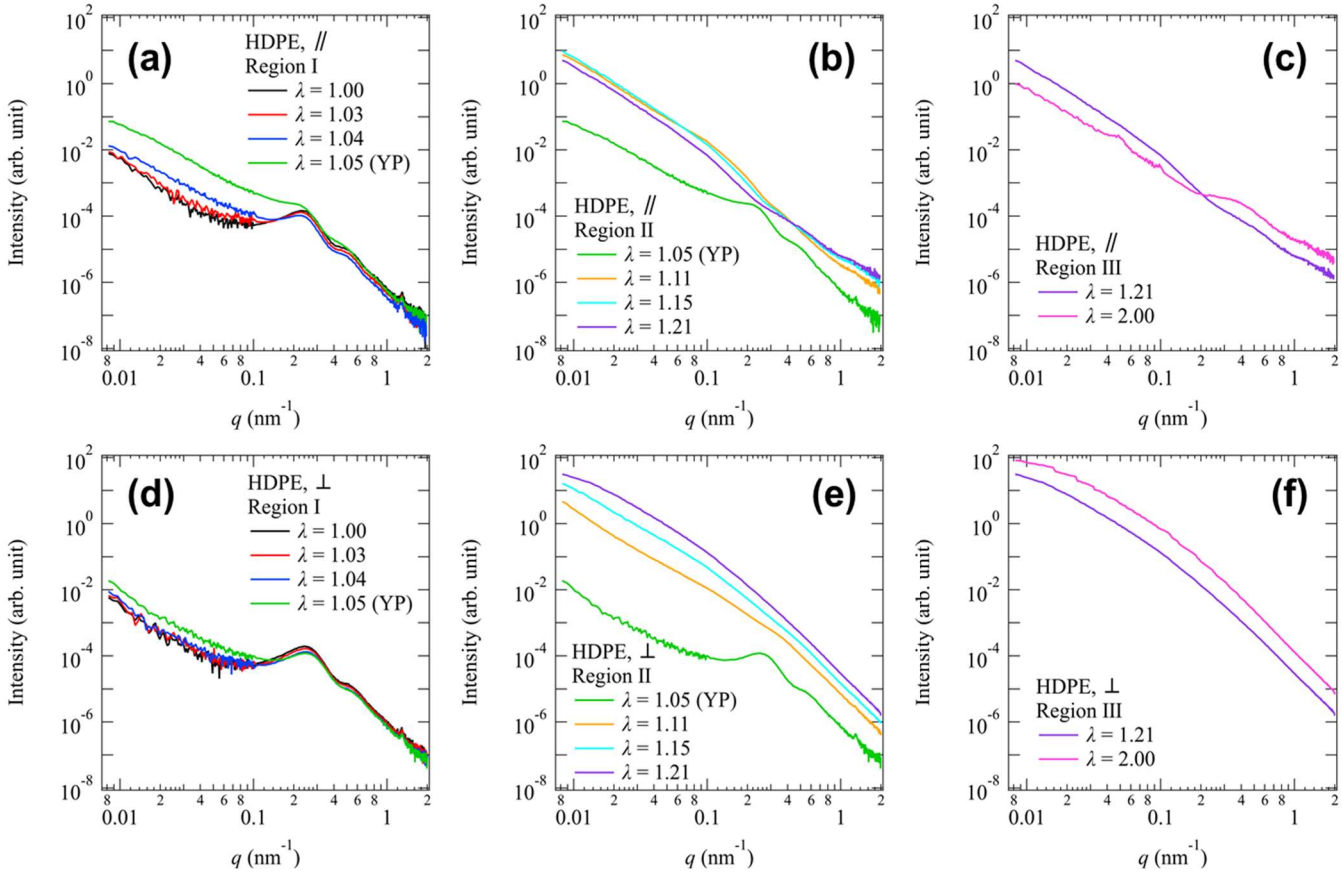

Figure 4.11 Combined USAXS and SAXS profiles from the HDPE in (a) and (d) Region I, (b) and (e) Region II, and (c) and (f) Region III. The profiles in (a), (b), and (c) and (d), (e), and (f) correspond to the scattering intensities parallel and perpendicular to the stretching directions, respectively.

patterns (Figures 4.10(i)–(k)) and profiles (Figure 4.11(a)), the peak positions in $I_{\parallel}(q)$ and $I_{\perp}(q)$ shifted toward smaller q- and larger q-regions, respectively, with strain. The changes in $D_i(\lambda)/D_i(1)$ $(i = \parallel \text{ or } \perp)$ in Figure 4.12 approximately followed the affine deformation. The WAXS patterns (Figures 4.10(q)–(s)) and μ dependences of the diffraction peaks in Figure 4.13 in Region I hardly changed with strain. However, a weak $(010)_{mono}$ reflection was detected in the parallel direction near the YP (Figure 4.10(s)) as well as in the LLDPE.

Thus, inhomogeneous deformation on the submicron scale and affine deformation in the lamellar structure occurred, but the lattice structure was hardly deformed. However, a very small part of the crystals with the orthorhombic phase transformed into those with the monoclinic phase near the YP by fine slip.

Region II

In Region II or when $1.05 < \lambda < 1.21$, inhomogeneous deformation and generation of voids occurred on the submicron scale, and a chevron-type morphology developed. In the USAXS patterns (Figures 4.10(d)–(g)), $I_{\parallel}(q)$ increased, and the butterfly patterns appeared clearly. Accordingly, an enhancement in $I_{\parallel}(q)$ was observed in Figure 4.11(b). The development of the butterfly pattern in the HDPE was much stronger than that in the LLDPE. In addition, $I_{\perp}(q)$ also increased (Figures 4.10(d)-(g) and 11(e)), suggesting the generation of voids immediately after the inhomogeneous deformation by the strong enhancement of the fluctuation. At the YP, necking and whitening occurred, supporting that the large amplitude, namely, the difference in electron density between the HCR and LCR, appeared in this region. The difference was caused by the large inhomogeneity of the stress field that arose from the stability of the crystals in the HDPE, which is discussed later.

The scattering intensity of the inhomogeneous structure dominated even the SAXS region (Figures 4.11(b) and (e)). Because of this overlap, the scattering from the lamellar structure was buried, and I was not able to evaluate its fragmentation. However,

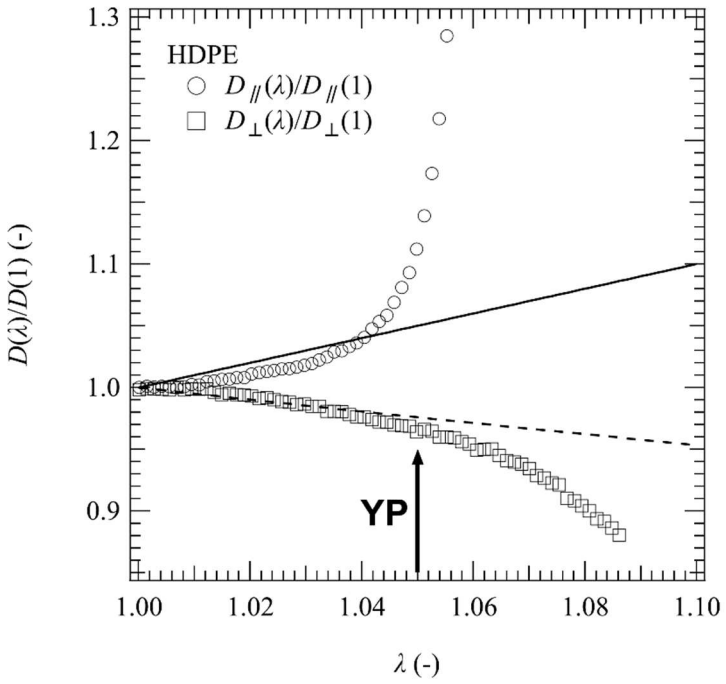

Figure 4.12 λ dependence of $D_{//}(\lambda)/D_{//}(1)$ and $D_{\perp}(\lambda)/D_{\perp}(1)$ in the HDPE. The solid and dashed lines are the lines calculated by Eqs. (5.3) and (5.4) obeying affine deformation.

the WAXS patterns (Figures 4.10(t)–(w)) and μ dependence of the diffraction peaks in Figures 4.13(a) and (c) showed that the $(110)_{ortho}$ and $(010)_{mono}$ peaks in the WAXS patterns were also oriented in the diagonal direction. This change is identical to that in Region II of the LLDPE. Thus, I expect a chevron-type morphology from the fragmentation and rotation of the lamellar structure by coarse slip.

In addition, mechanical melting slightly occurred as well in the HDPE as indicated by the decrease in the overall intensity in Figures 4.13(a) and (b). In contrast to the LLDPE, it started after the void generation and was not involved in the fracture mechanism in the HDPE.

Region III

In Region III, voids or string-like structure elongated along the parallel direction on the submicron scale were observed, and the chevron-type morphology was transformed into a fibrillar structure. The streaking along the perpendicular direction

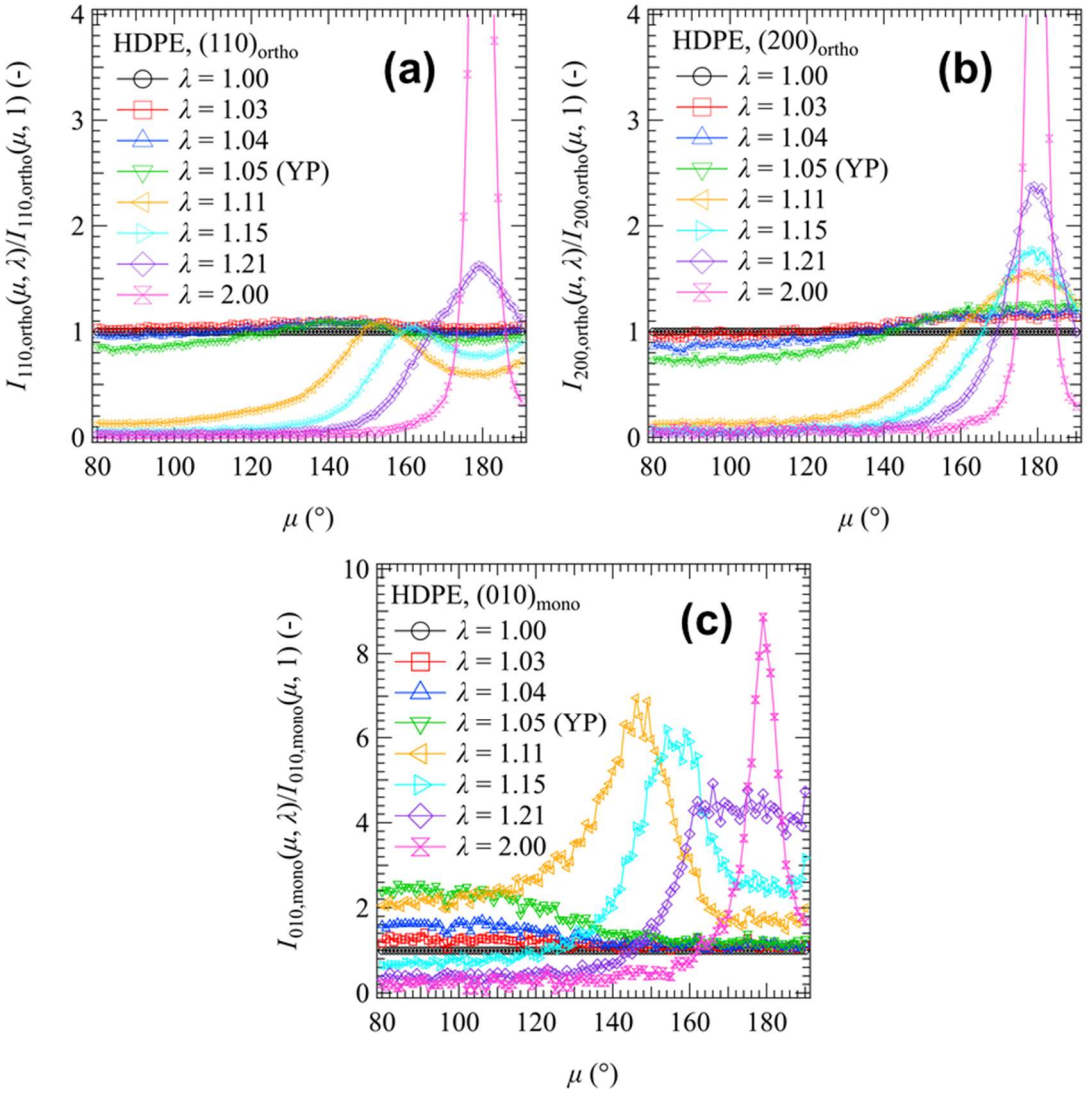

Figure 4.13 μ dependence of (a) $I_{110,ortho}(\mu, \lambda)/I_{110,ortho}(\mu, 1)$, (b) $I_{200,ortho}(\mu, \lambda)/I_{200,ortho}(\mu, 1)$, and (c) $I_{010,mono}(\mu, \lambda)/I_{010,mono}(\mu, 1)$ in WAXS patterns in the HDPE. $I_{110,ortho}(180, 2)/I_{110,ortho}(180, 1) = 10.5$ and $I_{200,ortho}(180, 2)/I_{200,ortho}(180, 1) = 7.60$.

increased with strain, as shown in the USAXS patterns (Figures 4.10(g)–(h)) and profiles (Figure 4.11(f)). They indicate that the string-like structure developed along the parallel direction by the coalescence and elongation of voids associated with the strain, as observed in Region IV for the LLDPE.

Although peaks from the lamellar structure in the SAXS patterns were not distinctly observed (Figures 4.10(o)–(p)), broad peaks around q = 0.4 nm^{-1} along the parallel direction were observed at λ = 2.00 (Figure 4.11(c)). The WAXS patterns and μ dependences of the peak intensities from the $(110)_{ortho}$, $(200)_{ortho}$, and $(010)_{mono}$ planes (Figures 4.11(w), (x) and 4.13) showed that the peaks at μ = 180° increased with strain, indicating the formation of a fibrillar structure.

4.3.5 Schematic Illustrations of the Changes in the Hierarchical Structures under Stretching

Schematic illustrations of the changes in the hierarchical structures in the LLDPE and HDPE were made based on the above discussion and are shown in Figure 4.14.

In both specimens, similar changes were found in each hierarchical structure. On the submicron scale, inhomogeneous deformations characterized by butterfly patterns between the HCRs and LCRs occurred, and the inhomogeneous structures led to the generation of voids. The lamellar structures experienced affine deformation and then transformed into chevron-type morphologies by fragmentation. Subsequently, fibrillar structures with short spacings were formed. According to the changes in the lamellar structures, the lattice structures became oriented in the same directions. However, the correlation between the changes in the hierarchical structures and the yielding behavior of the LLDPE differed from that of the HDPE.

In the LLDPE case, the formation of the chevron-type morphology and the inhomogeneous deformation on the submicron scale started at the 1YP, and the generation

of voids and its elongation started at the 2YP. On the other hand, the HDPE showed one yield point. At the YP, a strong inhomogeneity characterized by butterfly patterns was observed, and generation of voids and its elongation immediately started. This was caused by the difference in the spatial inhomogeneity in the stress fields. Doi and Onuki and Furukawa and Tanaka have theoretically indicated that a spatial inhomogeneity in the stress field enhances the concentration or density fluctuation during deformation.[28,29] According to their theories, the gradient of a stress field is proportional to the flux of the fluctuation. The crystals in the LLDPE were less stable and more likely to mechanical melt than those in the HDPE because they were thinner (Table 4.2) and influenced by comonomers.[30,31] Mechanical melting contributed to decreasing the gradient between the HCR and LCR, suppressing the enhancement of the fluctuation and delaying the generation of voids and necks. In other words, more stress was diffused on the scale of the lamellar structures in the LLDPE than in the HDPE.

In both specimens, the coarse and fine slips occurred as observed in previous studies. However, the structural change on the submicron scale affected the yield behaviors more strongly than the slips. It should be noted that the domination of the structural change on the submicron scale do not always occur in other LLDPE materials because the stability of the crystals may have changed because of crystallinity and comonomers. Even if the structural changes on the scale smaller than the lamellar structure have differed, the inhomogeneous flow affected by those structural changes would have given the universal fracture mechanism for PE. In the next chapter, the effects of crystallinity and comonomers will be quantitatively discussed.

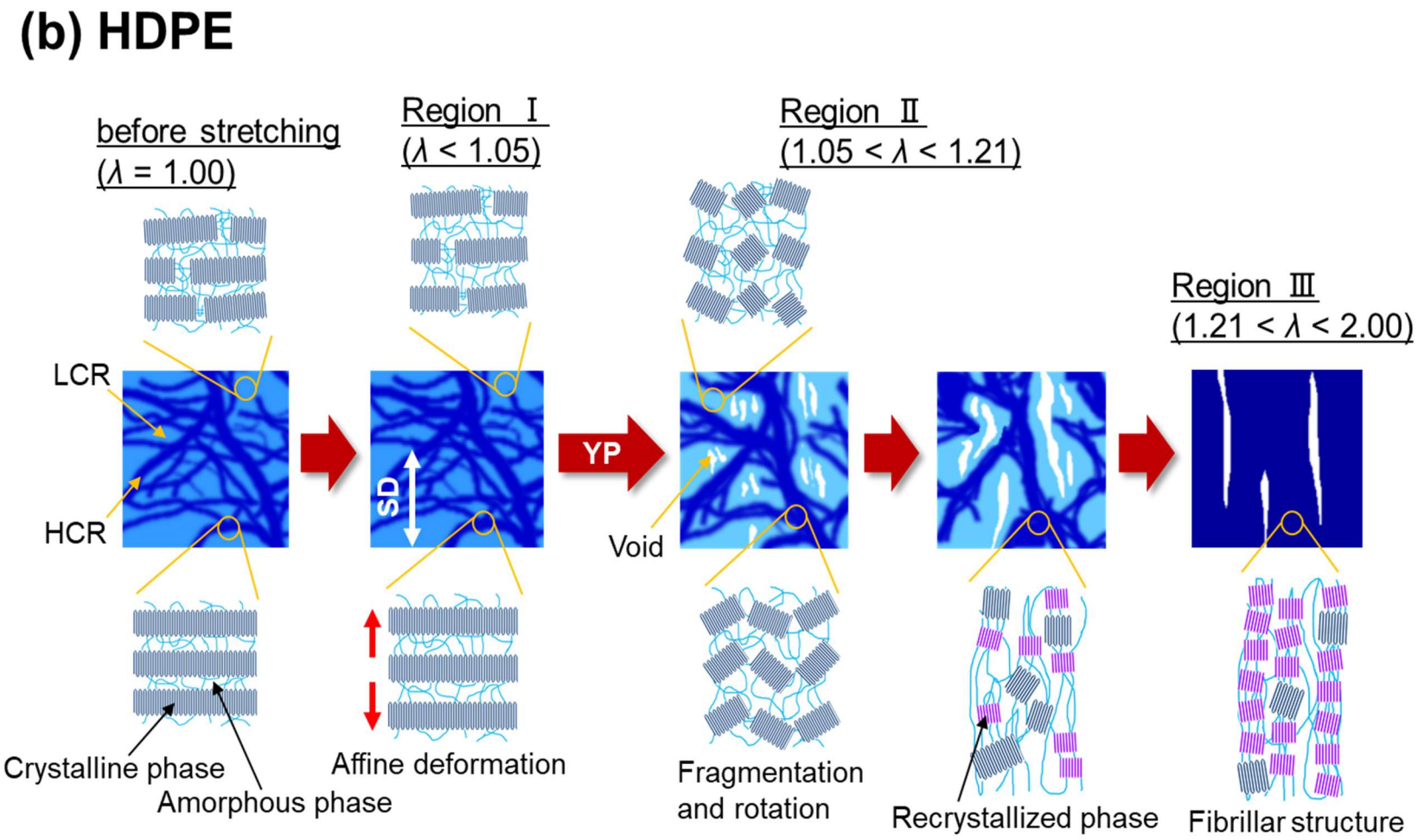

Figure 4.14 Schematic illustrations of the changes in the hierarchical structures in the (a) LLDPE and (b) HDPE during stretching.

(a) LLDPE

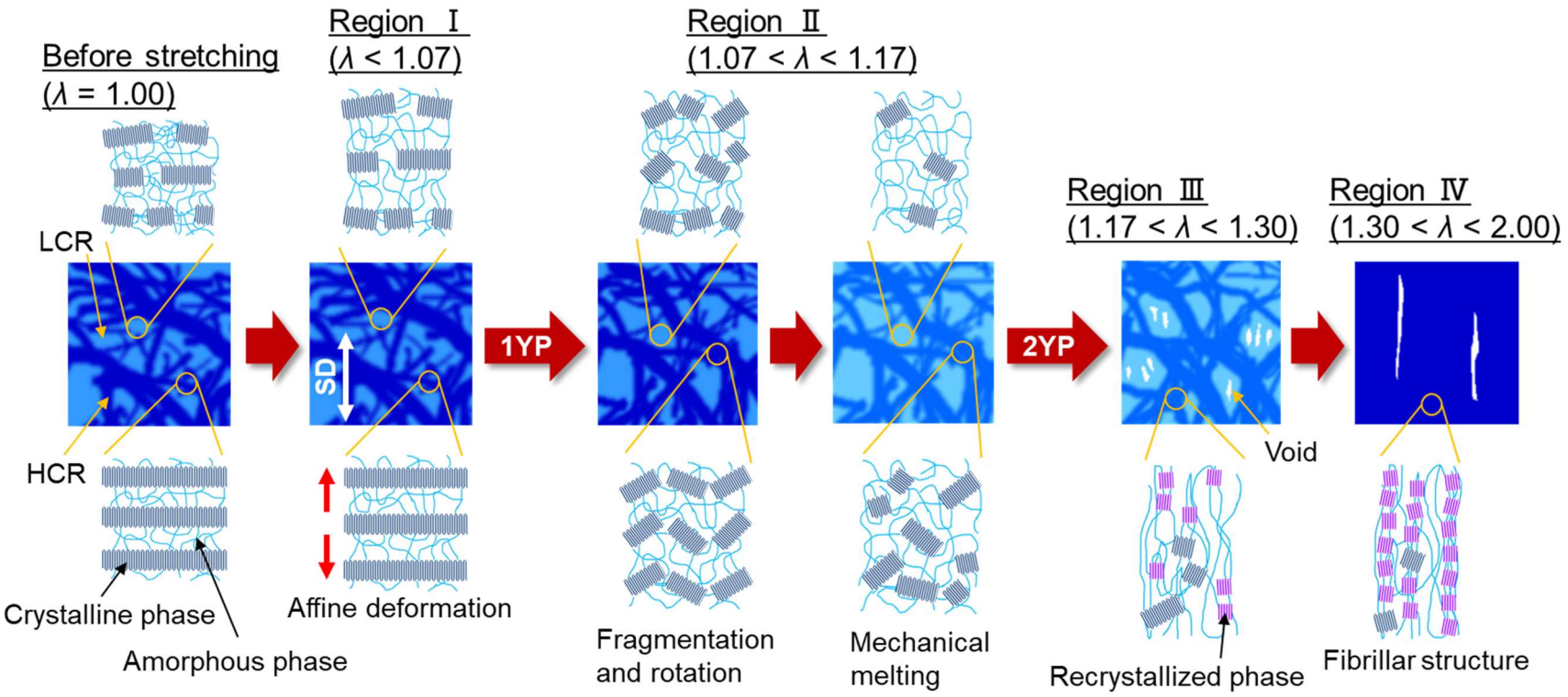
Before stretching
(λ = 1.00)
Region Ⅰ
(λ < 1.07)
Region Ⅱ
(1.07 < λ < 1.17)
Region Ⅲ
(1.17 < λ < 1.30)
Region Ⅳ
(1.30 < λ < 2.00)
LCR
HCR
SD
1YP
2YP
Void
Crystalline phase
Amorphous phase
Affine deformation
Fragmentation
and rotation
Mechanical
melting
Recrystallized phase
Fibrillar structure

4.4 Conclusion

The changes in the hierarchical structures of the LLDPE and HDPE, which showed a morphological transformation from spherulites to a fibrillar structure as a result of different yielding behaviors under uniaxial stretching, were observed using time-resolved USAXS, SAXS, and WAXS.

The S-S curve of LLDPE showed two yield points. Homogeneous deformation occurred in the structure on the submicron scale and in the lamellar structures until the 1YP. After the 1YP, the inhomogeneous deformation on the submicron scale started, and the density fluctuation was enhanced. The enhancement of density fluctuations and the formation of voids are induced by viscoelastic effects. According to the theory on the viscoelastic effect, the spatial inhomogeneity of the stress field causes the enhancement of density fluctuations under strain. Thus, the spatial distribution of the amorphous region plays an important role in the enhancement of density fluctuations and the formation of voids. The coarse slip followed by lamellar fragmentation and rotation produced the chevron-type morphology. The fine slip caused the phase transformation in the lattice structure. The strain also induced mechanical melting of the crystalline structure. After the 2YP, voids emerged and developed into the string-like structure in the LCR, which induced necking. The chevron-type morphology transformed into a fibrillar structure where the original and recrystallized lamellar structures were oriented along the parallel direction.

The HDPE exhibited one yield point on the S-S curve. Weak inhomogeneous deformation was observed on the submicron scale until the YP, while the lamellar structure showed affine deformation. However, a very small part of the crystals started the phase transformation. After the YP, the strong inhomogeneous deformation immediately caused the generation and aggregation of voids, and necking occurred with whitening. The chevron-type morphology was also formed, and then, the transformation to a fibrillar structure was observed, as in LLDPE.

Void formation did not occur at the 1YP but at the 2YP for the LLDPE, while voids were formed at the YP in the HDPE. This difference was caused by the fact that the lamellar structures in the LLDPE were obviously less stable than those in the HDPE. The modulus of the lamellar structure in the LLDPE was lower than that in the HDPE, so the increase in the density fluctuation with strain in the HDPE was much stronger than that in the LLDPE. The stability of the crystals in the LLDPE depended on the comonomer species and contents, so the yield behaviors were strongly affected by those factors. I elucidate the contribution of these factors quantitatively in the next chapter.

References

1. Seguela, R.; Rietsch, F., *J. Mater. Sci. Lett.* **1990,** *9*, 46-47.
2. Gaucher-Miri, V.; Séguéla, R., *Macromolecules* **1997,** *30*, 1158-1167.
3. Brooks, N. W. J.; Unwin, A. P.; Duckett, R. A.; Ward, I. M., *J. Macromol. Sci., Part B* **1995,** *34*, 29-54.
4. Hiss, R.; Hobeika, S.; Lynn, C.; Strobl, G., *Macromolecules* **1999,** *32*, 4390-4403.
5. Bowden, P. B.; Young, R. J., *J. Mater. Sci.* **1974,** *9*, 2034-2051.
6. Butler, M. F.; Donald, A. M.; Ryan, A. J., *Polymer* **1997,** *38*, 5521-5538.
7. Butler, M. F.; Donald, A. M.; Ryan, A. J., *Polymer* **1998,** *39*, 39-52.
8. Yagi, N.; Inoue, K., *J. Appl. Crystallogr.* **2003,** *36*, 783-786.
9. Takenaka, M., *Polym. J.* **2013,** *45*, 10-19.
10. Shinohara, Y.; Kishimoto, H.; Inoue, K.; Suzuki, Y.; Takeuchi, A.; Uesugi, K.; Yagi, N.; Muraoka, K.; Mizogichi, T.; Amemiya, Y., *J. Appl. Crystallogr.* **2007,** *40*, 397-401.
11. Takenaka, M.; Shimizu, H.; Nishitsuji, S., *Phys. Rev. E* **2007,** *75*, 061802.
12. Mita, K.; Fujii, S.; Nishitsuji, S.; Takenaka, M., *Kobunshi Ronbunshu* **2014,** *71*, 573-579.
13. Fujii, S.; Nishitsuji, S.; Takanaka, M.; Hasegawa, H., *Kobunshi Ronbunshu* **2009,** *66*, 612-618.
14. Masunaga, H.; Ogawa, H.; Takano, T.; Sasaki, S.; Goto, S.; Tanaka, T.; Seike, T.; Takahashi, S.; Takeshita, K.; Nariyama, N.; Ohashi, H.; Ohata, T.; Furukawa, Y.; Matsushita, T.; Ishizawa, Y.; Yagi, N.; Takata, M.; Kitamura, H.; Sakurai, K.; Tashiro, K.; Takahara, A.; Amamiya, Y.; Horie, K.; Takenaka, M.; Kanaya, T.; Jinnai, H.; Okuda, H.; Akiba, I.; Takahashi, I.; Yamamoto, K.; Hikosaka, M.; Sakurai, S.; Shinohara, Y.; Okada, A.; Sugihara, Y., *Polym. J.* **2011,** *43*, 471-477.
15. Strobl, G., *The Physics of Polymers*; Springer: Berlin; New York, 2007.
16. Bastide, J.; Leibler, L.; Prost, J., *Macromolecules* **1990,** *23*, 1821-1825.

17. Mendes, E.; Oeser, R.; Hayes, C.; Boué, F.; Bastide, J., *Macromolecules* **1996,** *29*, 5574-5584.
18. Kume, T.; Hattori, T.; Hashimoto, T., *Macromolecules* **1997,** *30*, 427-434.
19. Kume, T.; Hashimoto, T.; Takahashi, T.; Fuller, G. G., *Macromolecules* **1997,** *30*, 7232-7236.
20. Moses, E.; Kume, T.; Hashimoto, T., *Phys. Rev. Lett.* **1994,** *72*, 2037-2040.
21. Hashimoto, T.; Kume, T., *J. Phys. Soc. Jpn.* **1992,** *61*, 1839-1843.
22. Hashimoto, T.; Amino, N.; Nishitsuji, S.; Takenaka, M., *Polym. J.* **2019,** *51*, 109-130.
23. Gerasimov, V. I.; Genin, Y. V.; Tsvankin, D. Y., *J. Polym. Sci.: Polym. Phys. Ed.* **1974,** *12*, 2035-2046.
24. Jiang, Z.; Tang, Y.; Men, Y.; Enderle, H.-F.; Lilge, D.; Roth, S. V.; Gehrke, R.; Rieger, J., *Macromolecules* **2007,** *40*, 7263-7269.
25. Takahashi, Y.; Ishida, T.; Furusaka, M., *J. Polym. Sci. Part B: Polym. Phys.*. **1988,** *26*, 2267-2277.
26. Lucas, J. C.; Failla, M. D.; Smith, F. L.; Mandelkern, L.; Peacock, A. J., *Polym. Eng. Sci.* **1995,** *35*, 1117-1123.
27. Popli, R.; Mandelkern, L., *J. Polym. Sci. Part B: Polym. Phys.*. **1987,** *25*, 441-483.
28. Doi, M.; Onuki, A., *J. Phys.II* **1992,** *2*, 1631-1656.
29. Furukawa, A.; Tanaka, H., *Nat. Mater.* **2009,** *8*, 601-609.
30. Shirayama, K.; Kita, S.; Watabe, H., *Makromol. Chem.* **1972,** *151*, 97-120.
31. Simanke, A. G.; Alamo, R. G.; Galland, G. B.; Mauler, R. S., *Macromolecules* **2001,** *34*, 6959-6971.

Chapter 5
Factors Governing the Strain-Induced Density Fluctuations in PE

5.1 Introduction

Linear low-density Polyethylene (LLDPE) has been used widely in daily life owing to its excellent properties such as high tensile strength, high impact resistance and flexibility, and so on. LLDPE is made by copolymerization of ethylene and α-olefins. The various kinds of LLDPE with different comonomer characteristics such as species and contents have been produced industrially. LLDPE exhibits various mechanical properties depending on the comonomer characteristics so that the LLDPE suitable to the purpose can be selected from them. The variety of the mechanical properties originates from the change in the crystalline structures of the LLDPE with the comonomer characteristics. It is well-known that the crystalline polymers form hierarchical structures including crystalline lattice structures, lamellar structures, and spherulitic structures filled with lamellar branching structures, as shown in Figure 1.1. To understand the effects of the comonomer characteristics on the mechanical properties, the change in the hierarchical structures of the LLDPE having different comonomer characteristics needs to be investigated under stretching.

In Chapter 4, I have investigated how the hierarchical structures affect the mechanical properties of high-density polyethylene (HDPE) and LLDPE during uniaxial

stretching by using time-resolved X-ray scattering methods.[1] Their scattering patterns in ultra-small-angle X-ray scattering (USAXS) region showed the so-called abnormal butterfly patterns after some extent of strain, indicating that the enhancement of the density fluctuations on the order of 100 nm to 1 μm (submicron scale) was induced by strain. The further strain was found to cause the transformation of the density fluctuations into voids. The enhancement or strain-induced density fluctuation (SIDF) originates from the viscoelastic effect found in dynamically asymmetric systems such as gel under stretching and semidilute polymer solution under shear.[2-7] In the systems, concentration or density fluctuations induce the spatial inhomogeneity of the stress fields and the gradient of the stress fields enhances the spatial inhomogeneity of concentration or density fluctuations under deformation.[8,9] In the cases of the HDPE and LLDPE, the spatial inhomogeneity of the stress field originating from the spatial inhomogeneity of the crystallinity exists as an initial state and the gradient of the stress fields enhances the spatial inhomogeneity of the crystallinity under uniaxial stretching. The strength of the SIDF in the LLDPE was found to be weaker than that in the HDPE, reflecting that the spatial inhomogeneity of the stress field of the LLDPE was smaller than that of the HDPE. According to the theory of the viscoelastic effects,[8,9] the driving force of the SIDF is proportional to the gradient of the stress field. Thus, if melting of crystalline structures occurs associating with the application of the strain, the spatial inhomogeneity and the gradient of the stress field decrease and the SIDF may be suppressed. Melting of the crystalline phase in the LLDPE associating with the application of the strain was found to be more remarkable than that in the HDPE. The spatial inhomogeneity of the stress field and the SIDF in the LLDPE are, thus, less pronounced than those in the HDPE. It is worth mentioning that a number of deformation models below the scale of 100 nm have

been proposed based on time-resolved SAXS and WAXS measurements. Some of the models were mentioned in the introduction of Chapter 4.[1]

It is well-known that the stability of crystalline structures in LLPDE depends on comonomer characteristics.[10,11] I anticipated that the SIDF behaviors in LLDPE are affected by the comonomer characteristics. In this chapter, thus, I investigated how the comonomer characteristics affect the SIDF behaviors and clarified the factors governing the SIDF in the comonomer characteristics of the LLDPE.

5.2 Experimental Section

5.2.1 Characterization of Materials

30 wt% LLDPE/o-dichlorobenzene-d_4 solution was prepared for four types of LLDPE as shown in Table 5.1. Pulsed Fourier transform ^{13}C nuclear magnetic resonance (FT-^{13}C-NMR) measurements were performed at 130°C using a Bruker Avance III 600 MHz spectrometer. The proton decoupling was achieved only during acquisition to suppress the nuclear Overhauser effect. Because the longest spin-lattice relaxation time T_1 in the LLDPE was 3.6 sec, which would be derived from methyl carbons, the delay time between pulses was set to 20 sec ($> 5T_1$). The comonomer species and contents were determined by the method of Pooter et al from the obtained spectra.[12] The results are shown in Table 5.1 as well as the analysis of the molecular weight and its distribution.

5.2.2 Sample Preparation

The sheets of them in a 2 mm-thick were made by using press machines (MINI TEST PRESS-10, TOYOSEIKI). The LLDPE pellets were melted in the machines at 180˚C, and molded into sheets with 10 MPa for 10 min. Subsequently, they were

quenched by transferring them on the plate at 20 °C. Sandglass-shaped specimens with a center width of 2 mm were punched out from the sheets. The density and crystallinity W_c calculated from the density of the sheets are listed in Table 5.1. Here, I assumed a two-phase system consisting of a crystalline and amorphous phase, with the density of 1.00 g/cm^3 and 0.855 g/cm^3, respectively.[13]

Table 5.1 Characterization of the Materials Used Herein

name	comonomer species	comonomer content (mol%)	M_w[a]	M_w/M_n[a]	density of the sheet at 20 °C[b]	W_c (wt%)
H920	4-methylpentene-1	3.00	2.0×10^5	4.2	0.919 g/cm^3	48
H935	4-methylpentene-1	0.80	2.1×10^5	5.3	0.937 g/cm^3	60
B920	butene-1	3.46	2.2×10^5	3.2	0.920 g/cm^3	49
B935	butene-1	1.93	2.2×10^5	4.7	0.933 g/cm^3	58

a. Determined by gel permeation chromatography (Viscotek Triple Detector HT-GPC Model-SG system, Malvern Instruments Ltd.) to be polystyrene-equivalent values at Northeastern Industrial Research Center of Shiga Prefecture, Shiga, Japan.
b. Measured by helium pycnometer (AccuPyc 1330, Shimadzu).

5.2.3 USAXS, SAXS, and WAXS Measurements

In-situ X-ray scattering measurements under tensile tests were performed by using a homemade tensile tester with the tensile speed being 1 mm/min. Stress-strain (S-S) curves were obtained simultaneously during the in-situ X-ray scattering experiments. The USAXS measurements were performed at the second hutch of beamline BL03XU, SPring-8, Hyogo, Japan.[14,15] The camera length and the wavelength of the incident beam were, respectively, 7.5 m and 2.0 Å, and thus the wavenumber q-range of USAXS was $0.0075 < q < 0.5$ nm^{-1}. Here, q is the magnitude of the scattering vector $\boldsymbol{q}$ defined by $q = (4\pi/\lambda_{X\text{-ray}})\sin(\theta/2)$, where $\lambda_{X\text{-ray}}$ and θ are the wavelength of the incident X-rays and the scattering angles, respectively. Pilatus 1M (DECTRIS) was used as a detector, and the

exposure time for each measurement was 850 ms. The simultaneous SAXS and WAXS measurements were also performed at the same beamline as used in USAXS measurements. The wavelength of the incident X-ray for SAXS and WAXS was 1.0 Å. Pilatus 1M and Flat Panel Detector were used as a detector for SAXS and WAXS, respectively. The camera lengths for the SAXS and WAXS were 2.4 m and 120 mm, 670 ms and 570 ms, respectively. The q-ranges of SAXS and WAXS were $0.06 < q < 1.3$ nm^{-1} and $4 < q < 26$ nm^{-1}, respectively. I corrected the two-dimensional (2D) scattering patterns of USAXS, SAXS, and WAXS for the background, transmittance, and thickness.

5.3 Results and Discussion

5.3.1 Hierarchical structures of LLDPE before stretching

I confirmed by NMR that H920 and H935 contain 4-methylpentene-1 (4MP1) and B920 and B935 contain butene-1 as a comonomer, respectively. H920 and B920 show higher comonomer content and lower crystallinity than H935 and B935, which proves that the increase in the comonomer contents decreases the crystallinity of the sheets. In addition, H920, which has slightly lower density than B920, contains smaller comonomer content than B920. It indicates that 4MP1, or the bulkier comonomer destabilize the lamellar structures by the accumulation near the crystalline surface.[10,11] Note that H935 is the same as the LLDPE in Chapter 4.

I analyzed the USAXS, SAXS, and WAXS patterns before stretching and obtained the characteristic parameters of the hierarchical structures of the LLDPE samples. The scattering patterns of USAXS, SAXS, and WAXS for all LLDPE samples before stretching are shown in Figure 5.1. All USAXS, SAXS, and WAXS patterns were isotropic and there were no peaks in the patterns in all USAXS patterns. The scattering

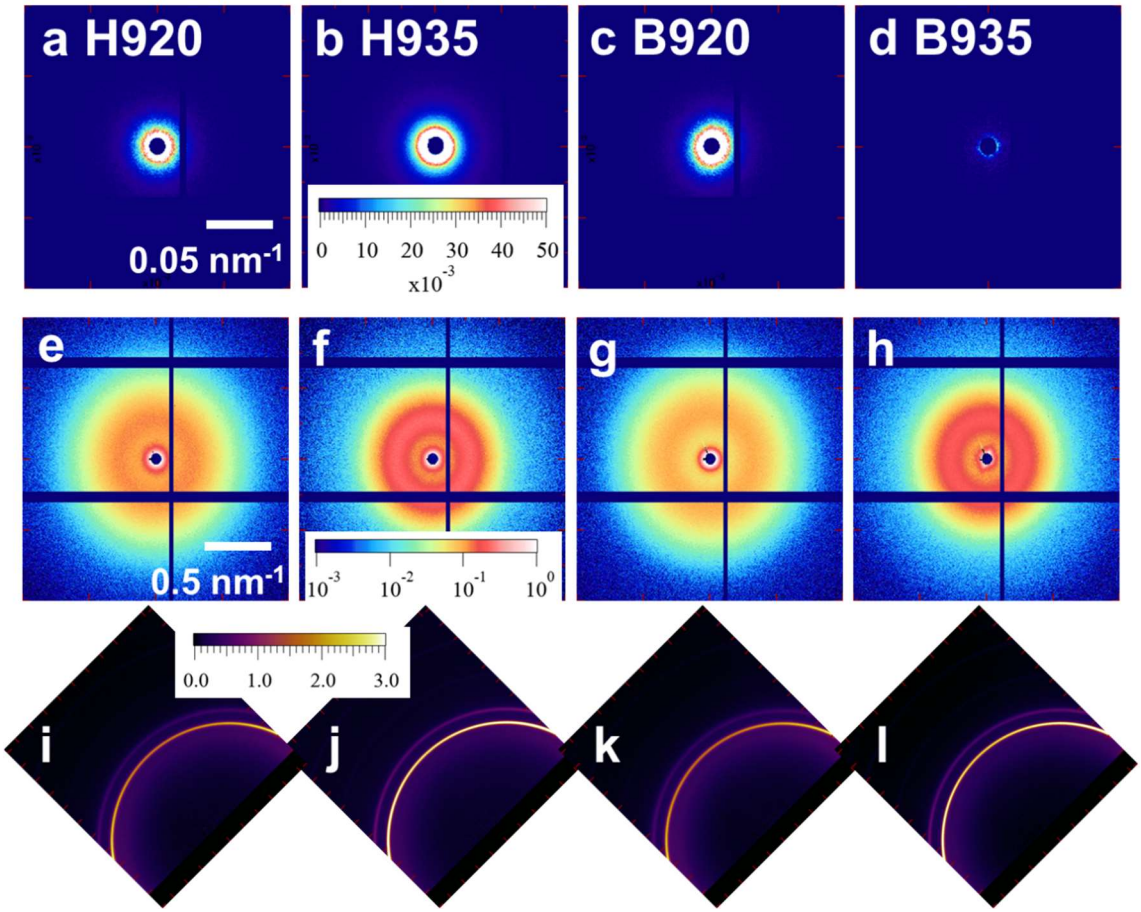

Figure 5.1 (a)–(d) USAXS, (e)–(h)SAXS, and (e)–(h)WAXS 2D patterns of all LLDPE samples before the application of strain. (a)(e)(i), (b)(f)(j), (c)(g)(k), and (d)(h)(l) correspond to the scattering patterns of H920, H935, B920, and B935, respectively.

peak originating from the periodicity of lamellar structures was observed in all SAXS patterns. All WAXS patterns exhibited isotropic peaks of the lattice structures of LLDPE. I calculated the scattering profiles by averaging the 2D patterns circularly.

Figure 5.2 shows the combined USAXS and SAXS profiles and WAXS profiles for the LLDPE samples. I quantitatively evaluated the inhomogeneity on the submicron scale by calculating the invariant ($Q_{\mathrm{U,iso}}$) defined as:

$$Q_{\mathrm{U,iso}} = 4\pi \int_{0.0075}^{0.0628} q^2 I(q) dq \tag{5.1}$$

The calculated $Q_{\mathrm{U,iso}}$ values are listed in Table 5.2. The degree of spatial inhomogeneity on the submicron scale decreased with comonomer content in both comonomer types. The change in the degree with comonomer content for LLDPE with 1-butene, or B-series was greater than that for LLDPE with 4MP1, or H-series. B920 was most inhomogeneous while B935 was most homogeneous among all the samples.

I also attempted to estimate the characteristic lengths of the inhomogeneous structures on the submicron scale. In the case of H935, H920, and B920, $I(q)$ at $q < 0.06$ nm^{-1} was expressed by the Debye-Bueche function:[16]

$$I(q) = \frac{I(0)}{[1+(q\Xi)^2]^2} \tag{5.2}$$

where Ξ and $I(0)$ are, respectively, the correlation length of the inhomogeneous structure

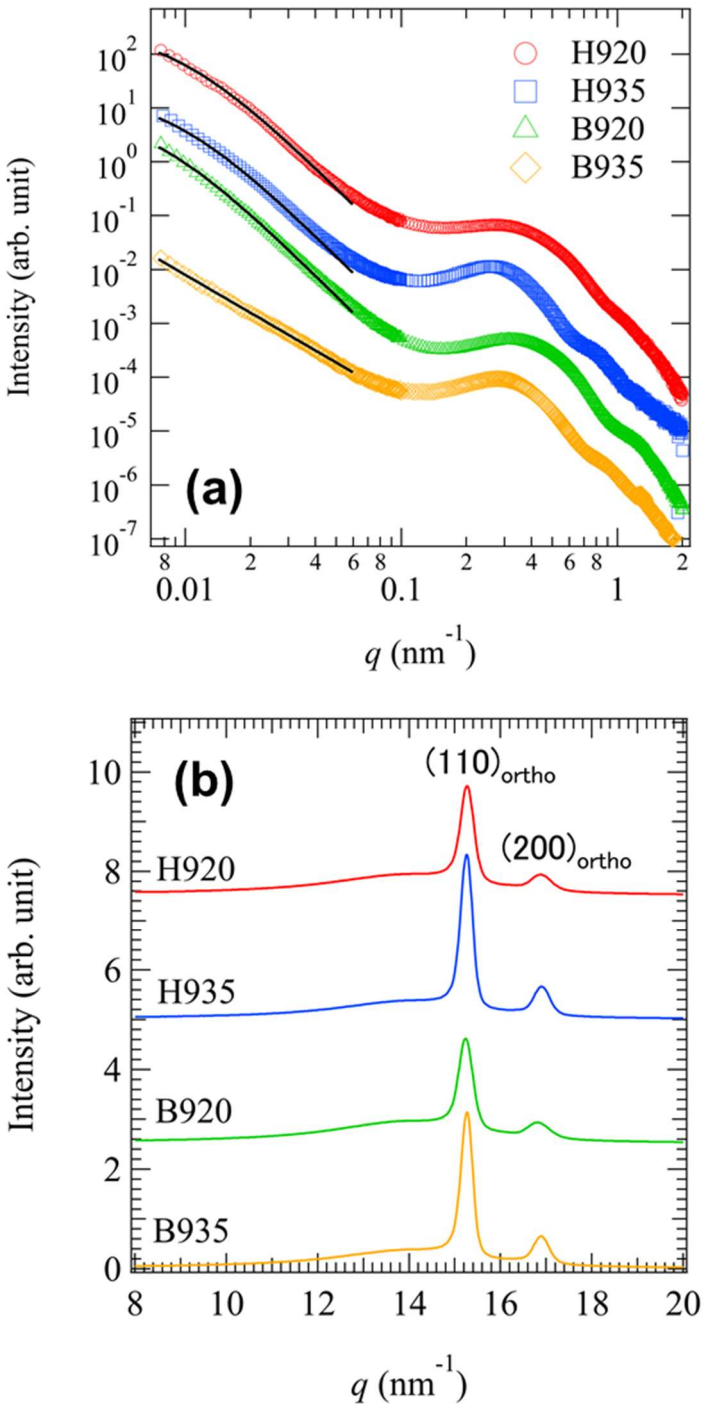

Figure 5.2 (a) Combined USAXS/SAXS profiles and (b) WAXS profiles of all samples before the application of strain. The solid lines in part(a) indicate the fitting curves. Each profile is shifted vertically for clarity.

and $I(q)$ at $q = 0$. The values of Ξ and $I(0)$ are also listed in Table 5.2. The values of Ξ seemed to be insensitive to the comonomer characteristic. After the polymerization, comonomers turn into the short branches. Since the crystalline phase regards the short branches as impurities, the short branches ejected from the crystalline phase during the crystallization process would induce the inhomogeneous structure. The fact that the USAXS profiles can be fitted with Debye-Bueche function suggests that the inhomogeneous structure is similar to a phase-separated structure. In the case of B935, $I(q)$ at $q < 0.05$ nm^{-1} was expressed by the following power-law behavior:

$$I(q) = I_{\mathrm{f}} q^{-n_{\mathrm{f}}} \tag{5.3}$$

where I_{f} and n_{f} are the front factor and mass fractal dimension, respectively. We could not find the characteristic length for B935. The density fluctuation associated with the mass fractal-like inhomogeneous structure existed in the spherulites of B935.[17] The value of n_{f} for B935 was 2.3 and B935 exhibited more homogeneous structure than the other samples.

In $I(q)$ at $q > 0.06$ nm^{-1}, I found the peaks originating from the lamellar structures around $q = 0.3$ nm^{-1}. I estimated the long spacing of the lamellar structures (d_{ac}) after Lorentz correction.[18] The obtained values were listed in Table 5.2.

I observed reflections from the (110) and (200) lattice planes in the orthorhombic phase in the WAXS profiles (Figure 5.2(b)).

Table 5.2 Evaluated Parameters in This Section

name	$Q_{U,iso}$ (a.u.)	$I(0)$ (a.u.)	Ξ (nm)	d_{ac} (nm)
H920	1.62×10^{-6}	0.295	109	12.0
H935	9.92×10^{-7}	0.199	112	15.8
B920	1.94×10^{-6}	0.884	144	11.7
B935	3.86×10^{-7}	-	-	14.9

5.3.2 S-S curves

S-S curves for the LLDPE samples are shown in Figure 5.3. Here, the vertical axis represents the engineering stress, and the horizontal axis represents the draw ratio λ defined as:

$$\lambda = \frac{L}{L_0} \tag{5.4}$$

with L_0 and L being the initial length of the samples and the length of the samples during stretching, respectively. Two yield points were observed in all LLDPE samples. I call the yield points at the smaller and larger λ 1YP and 2YP, respectively. Note that necking occurred in all the samples from the 2YP and that the scattering results reflected necking.

I analyzed the changes in each hierarchical structure of the LLDPE samples with strain by using USAXS, SAXS, and WAXS as I did in Chapter 4. The changes were able to be divided into several strain regions. First, I describe the details of the analyses in each region (5.3.3–5.3.5). Then, I describe the analyses focusing on the SIDF (5.3.6–5.3.7). For the changes in the hierarchical structures of H935, see the results of the LLDPE in Chapter 4.

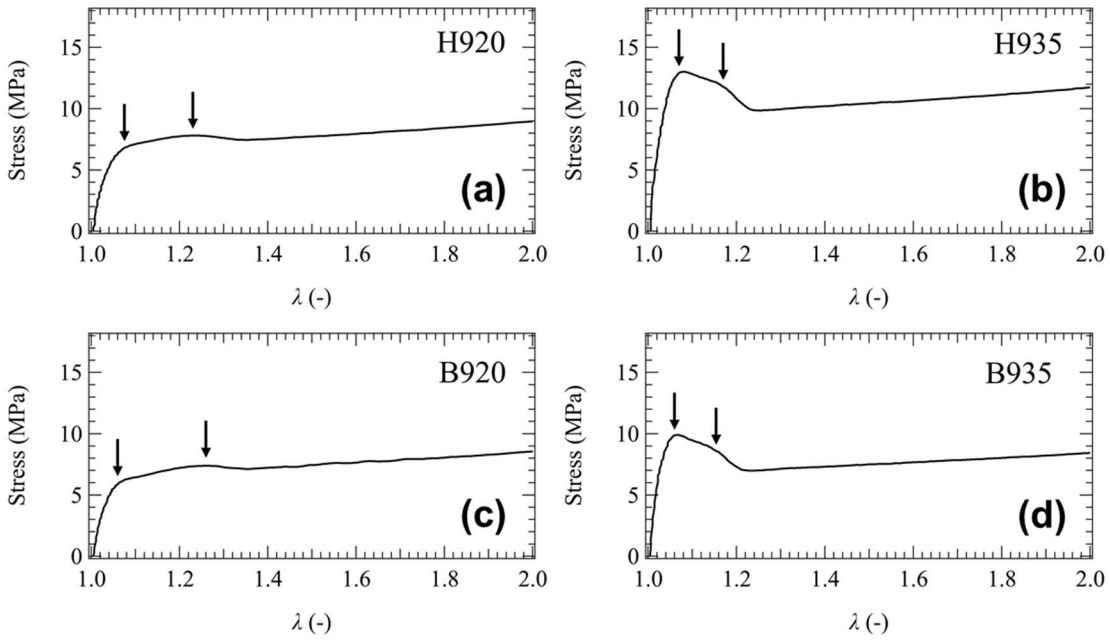

Figure 5.3 S-S curves of all samples. The arrows indicate the yield points.

5.3.3 Changes in the Hierarchical Structures of H920

Figure 5.4 shows the changes in the 2D USAXS, SAXS, and WAXS patterns as a function of the strain for H920. I also show the combined USAXS and SAXS profiles along with the directions parallel and perpendicular to the stretching axis for H920 in Figure 5.5. Here, the profiles $I_{\parallel}(q)$ along the parallel direction were obtained by sector averages for $85^{\circ} < \mu < 95^{\circ}$ and $265^{\circ} < \mu < 275^{\circ}$, while the profiles $I_{\perp}(q)$ along the perpendicular direction were for $-5^{\circ} < \mu < 5^{\circ}$ and $175^{\circ} < \mu < 185^{\circ}$. The definition of the azimuthal angle μ is shown in Figure 5.21(b).

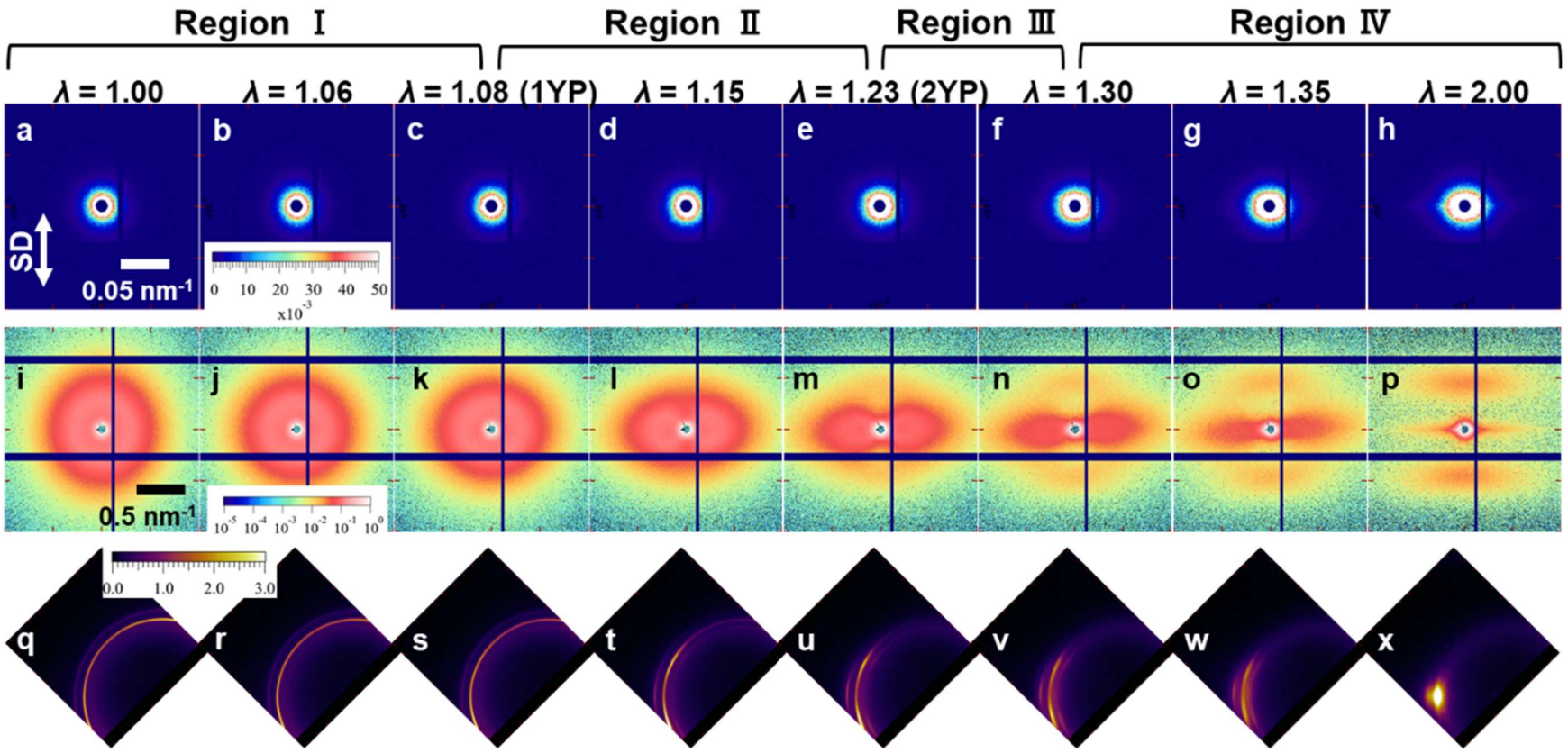

Figure 5.4 (a)–(h) USAXS, (i)–(p)SAXS, and (q)–(x)WAXS 2D patterns of H920 with strain. The arrow in part(a) corresponds to the stretching direction.

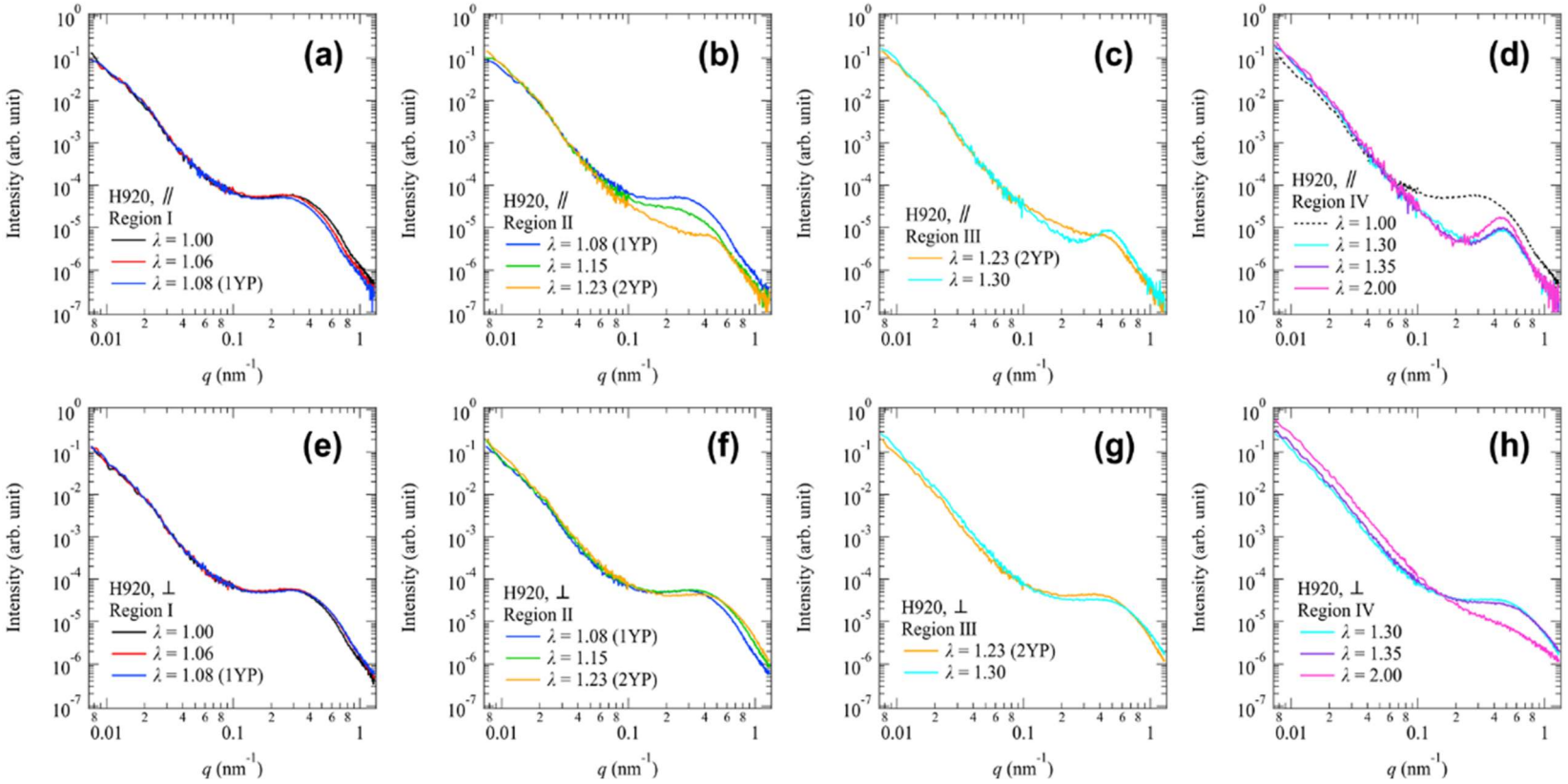

Figure 5.5 Combined USAXS and SAXS profiles from H920 in (a) and (e) Region I, (b) and (f) Region II, (c) and (g) Region III, and (d) and (h) Region IV, respectively. The profiles in (a), (b), (c), and (d) and (e), (f), (g), and (h) correspond to the scattering intensities parallel and perpendicular to the stretching directions, respectively.

The changes in the scattering patterns with strain can be classified into the following 4 regions. Region I: strain domain before the 1YP or at $\lambda < 1.08$, Region II: strain domain between the 1YP and 2YP or at $1.08 < \lambda < 1.23$, Region III: strain domain after the 2YP or at $1.23 < \lambda < 1.30$, and Region IV: strain domain at $1.30 < \lambda$.

Region I (H920)

In Region I ($\lambda < 1.08$), the strain induced the deformation and mechanical melting of the lamellar structures. The USAXS patterns of the LLDPE (Figures 5.4(a)–(c)) hardly changed with strain. Both $I_{\parallel}(q)$ (Figure 5.5(a)) and $I_{\perp}(q)$ (Figure 5.5(e)) at $q < 0.05$ nm^{-1} did not change with strain. The changes in the profiles in the small q-region indicate that the submicron structure was not deformed in this region. Contrary to the results of USAXS, the SAXS pattern (Figures 5.4(i)–(k)) was slightly elongated to the direction perpendicular to the stretching direction. The peak positions of $I_{\parallel}(q)$ and $I_{\perp}(q)$ shifted toward smaller q and larger q, respectively, with the strain. I estimated the long spacings along the parallel ($D_{\parallel}$) and perpendicular ($D_{\perp}$) directions by using the following equation:

$$D_i = \frac{2\pi}{q_{\mathrm{m},i}} \quad i = \parallel, \perp \tag{5.5}$$

where $q_{\mathrm{m},i}$ is the peak position. I obtained $q_{\mathrm{m},\parallel}$ and $q_{\mathrm{m},\perp}$ by fitting $I_{\parallel}(q)$ and $I_{\perp}(q)$, respectively, to a linear combination of a power law and Gaussian function. I plotted the ratios $D_i(\lambda)/D_i(1)$ as a function λ in Figure 5.6(a). The solid and dashed lines obtained by the following equations assuming affine deformation:[15]

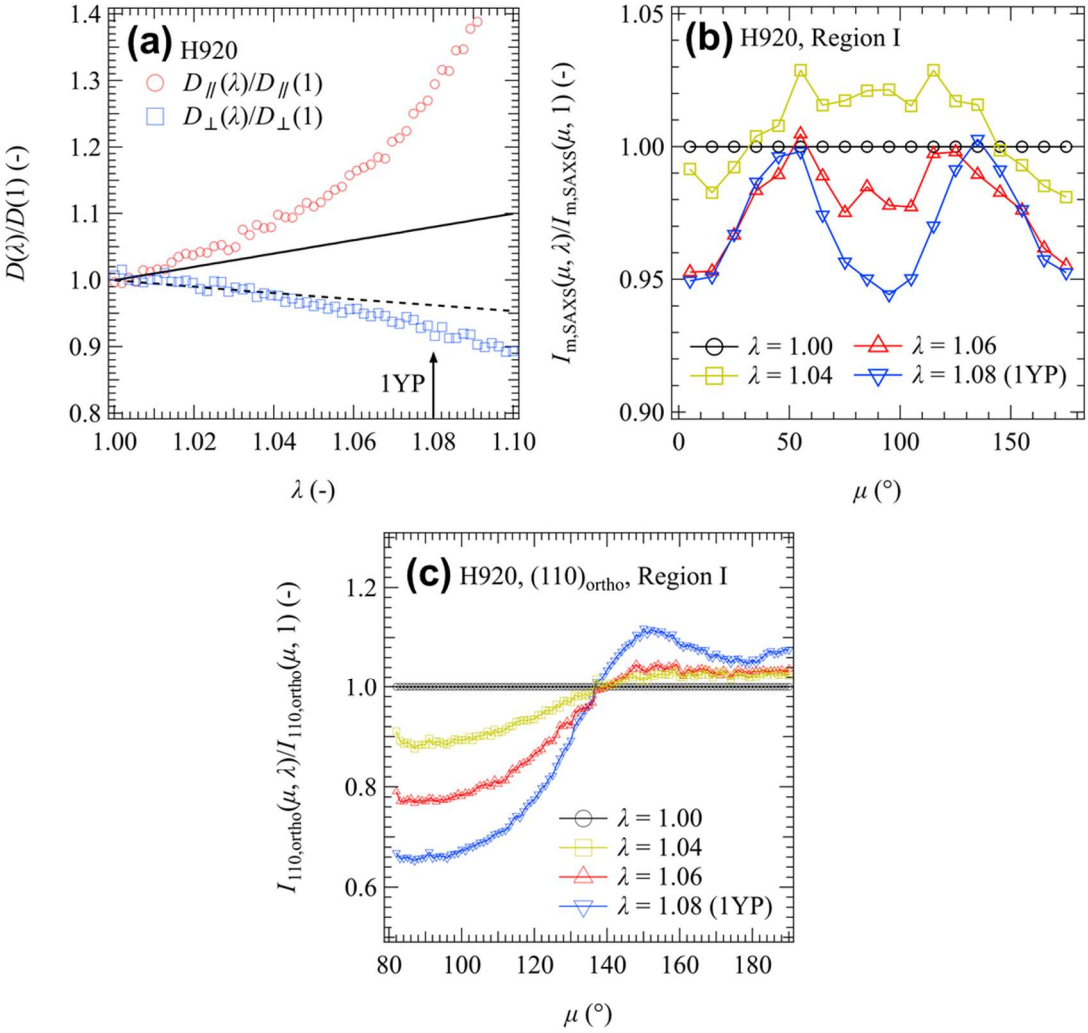

Figure 5.6 (a) λ dependence of $D_{//}(\lambda)/D_{//}(1)$ and $D_{\perp}(\lambda)/D_{\perp}(1)$ of H920. The solid and dashed lines are the lines calculated by Eqs. (5.6) and (5.7) obeying affine deformation. (b) μ dependence of the reduced peak intensity $I_{m,SAXS}(\mu, \lambda)/I_{m,SAXS}$ (μ, 1) of SAXS patterns and (c) $I_{110,ortho}(\mu, \lambda)/I_{110,ortho}(\mu, 1)$ in WAXS patterns in Region I in H920.

$$\frac{D_{\parallel}(\lambda)}{D_{\parallel}(1)} = \lambda \tag{5.6}$$

$$\frac{D_{\perp}(\lambda)}{D_{\perp}(1)} = \lambda^{-\frac{1}{2}} \tag{5.7}$$

The amount of the deformation parallel to the stretching direction is larger than that estimated under the assumption of affine deformation. Mechanical melting enhanced the increase in the long spacing. Figure 5.6(b) shows the μ dependence of the peak intensities of the SAXS patterns. I fitted sector averages at every 10˚ to a linear combination of a power law and Gaussian function and plotted the obtained front factors of the Gaussian function against μ. Figure 5.6(b) shows that overall intensity decreased with strain. The result indicates that mechanical melting started in this region. Figure 5.6(c) shows the μ dependence of the WAXS intensity from $(110)_{ortho}$ reflection. The reflection at μ = 90 ° decreased with strain, suggesting that the crystalline structure stacked along the perpendicular direction was more favorable for mechanical melting than that stacked along the parallel direction. Figure 5.6(b) shows that two peaks appeared at $0 < \mu < 180°$ around the 1YP, indicating the formation of diagonal pattern, or so-called four-point pattern. The patterns attributed to the chevron-type morphology induced by the fragmentation and rotation of the lamellar structures. As shown in Figure 5.6(c), The μ dependence of the WAXS intensity from $(110)_{ortho}$ reflection also split around the 1YP. The changes in SAXS and WAXS patterns indicate lamellar fragmentation and rotation started around the 1YP. After the 1YP, the small peak from (010) plane in the monoclinic phase appeared along the parallel direction (Figure 5.7). This transformation was also

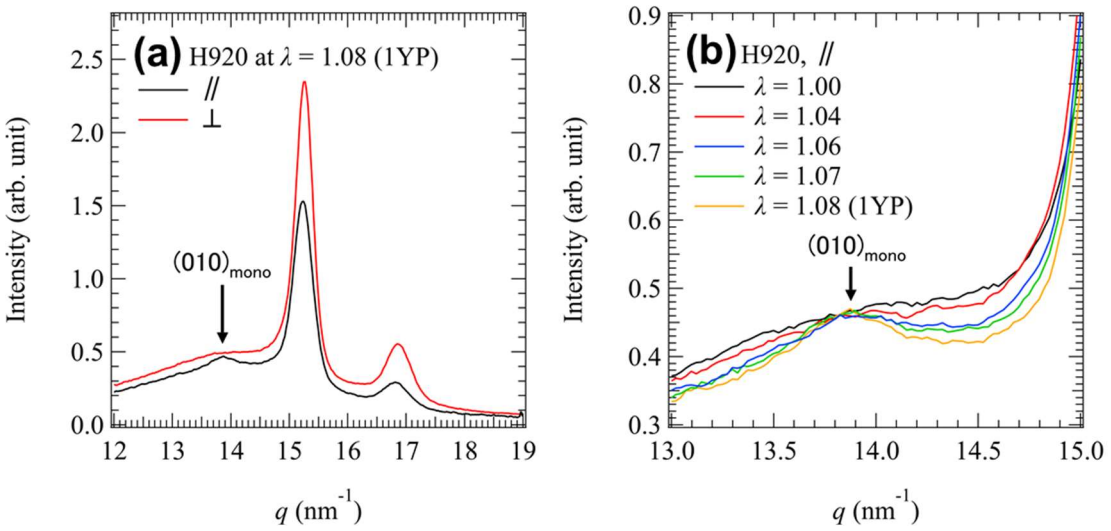

Figure 5.7 (a) WAXS profiles parallel and perpendicular to the stretching directions at λ = 1.08 and (b) evolution of the diffraction intensities from the (010) plane in the monoclinic crystals.

observed in H935. The fine slip on the $(110)_{ortho}$ plane causes the transformation into the monoclinic phase.

Region II (H920)

In Region II ($1.08 < \lambda < 1.23$), the inhomogeneous structure on the submicron scale hardly changed with strain, and a chevron-type morphology was developed. The USAXS patterns (Figures 5.4(c)–(e)) hardly changed with strain. In the profiles of USAXS region, I found the shift of the profiles to smaller q-region, indicating that the elongation of the inhomogeneous structure along the parallel direction might occur with strain. In SAXS patterns (Figures 5.4(k)–(m)), the four-point patterns were clearly observed, reflecting the rotation and orientation in the diagonal direction of lamellar structures. The $(110)_{ortho}$ peak in the WAXS patterns (Figures 5.4(s)–(u)) was also oriented in the diagonal direction. The μ dependence (Figure 5.8(a)) clearly shows the change in

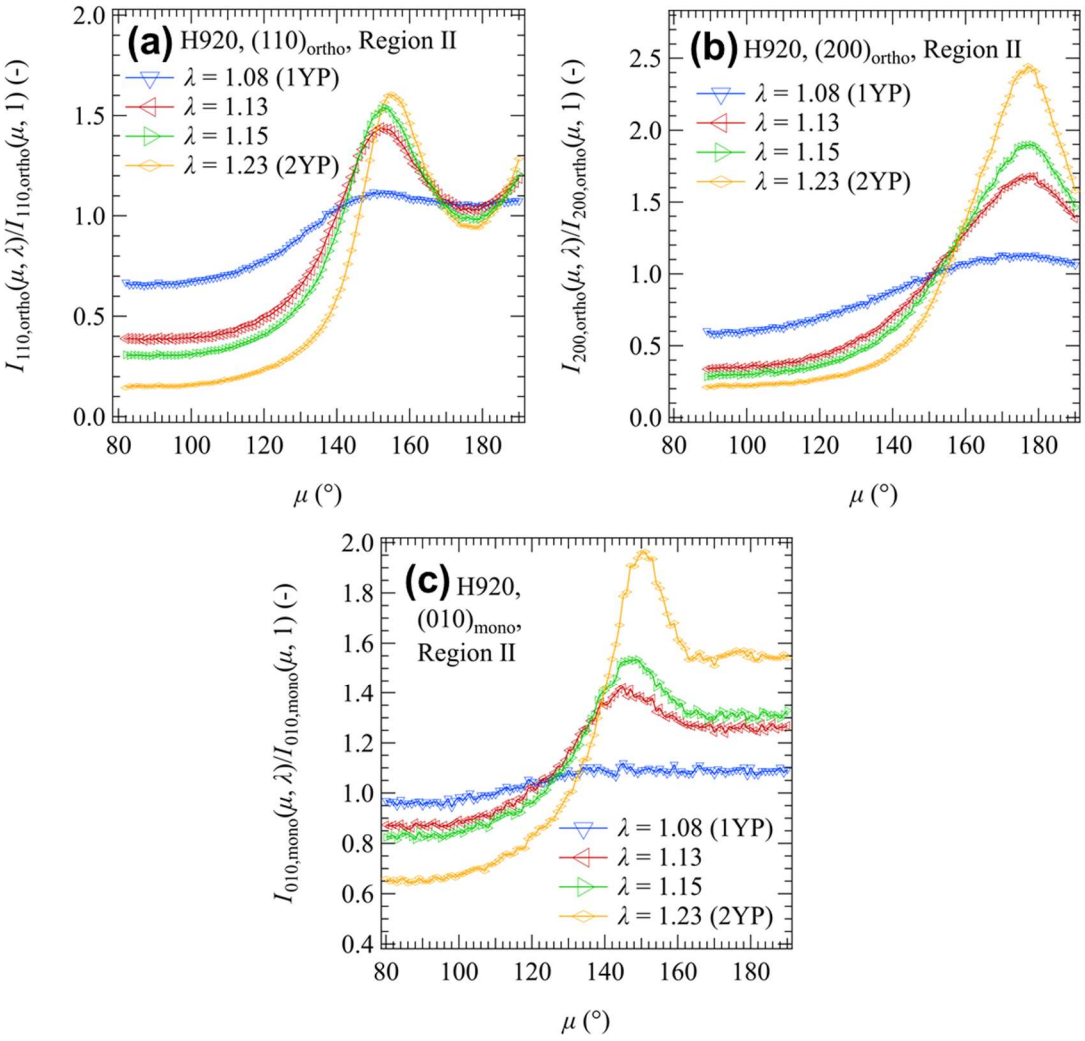

Figure 5.8 μ dependence of (a) $I_{110,ortho}(\mu, \lambda)/I_{110,ortho}(\mu, 1)$, (b) $I_{200,ortho}(\mu, \lambda)/I_{200,ortho}(\mu, 1)$, and (c) $I_{010,mono}(\mu, \lambda)/ I_{010,mono}(\mu, 1)$ in WAXS patterns in Region II in H920.

the orientation. The $(200)_{ortho}$ peak developed in the perpendicular directions (Figure 5.8(b)). The perpendicular orientation of $(200)_{ortho}$ planes and the diagonal orientation of the $(110)_{ortho}$ planes indicate that fragmentation occurred on the $(110)_{ortho}$ planes. Moreover, the $(010)_{mono}$ planes oriented along with the $(110)_{ortho}$ plane (Figure 5.8(c)). Thus, the WAXS patterns indicate that both lamellar fragmentation (coarse slip) and fine slip occurred on the $(110)_{ortho}$ plane.

Region III (H920)

In Region III, the inhomogeneous structure on the submicron scale elongated along the parallel direction, and the chevron-type morphology transformed into a fibrillar structure. The fibrillar structure included the recrystallized lamellar structure aligned in the parallel direction. The long spacing of the recrystallized lamellar structure was shorter than the original lamellar structures. As shown in Figures 5.4(e) and (f), the USAXS intensity elongated to the perpendicular direction. Thus, the inhomogeneous structures elongated to the direction parallel to the stretching direction. The SAXS patterns (Figures 5.4(m) and (n)) showed the decrease in the four-point pattern with strain, associating with mechanical melting. At approximately $\lambda = 1.30$, a broad peak appeared at approximately $q = 0.4$ nm^{-1} in the parallel direction. This peak reflects the recrystallized lamellar structure stacked with short spacings along the parallel direction. The WAXS patterns (Figures 5.4(u) and (v)) and μ dependences of the diffraction peaks (Figure 5.9 (a)) show the $(110)_{ortho}$ peak corresponding to the four-point pattern decreased while the peak intensity at μ =180° increased with strain, indicating the formation of a fibrillar structure.

Region IV (H920)

In Region IV, I observed the streak in the USAXS pattern (Figure 5.4(h)), indicating that the elongated voids appeared. The chevron-type morphology transformed

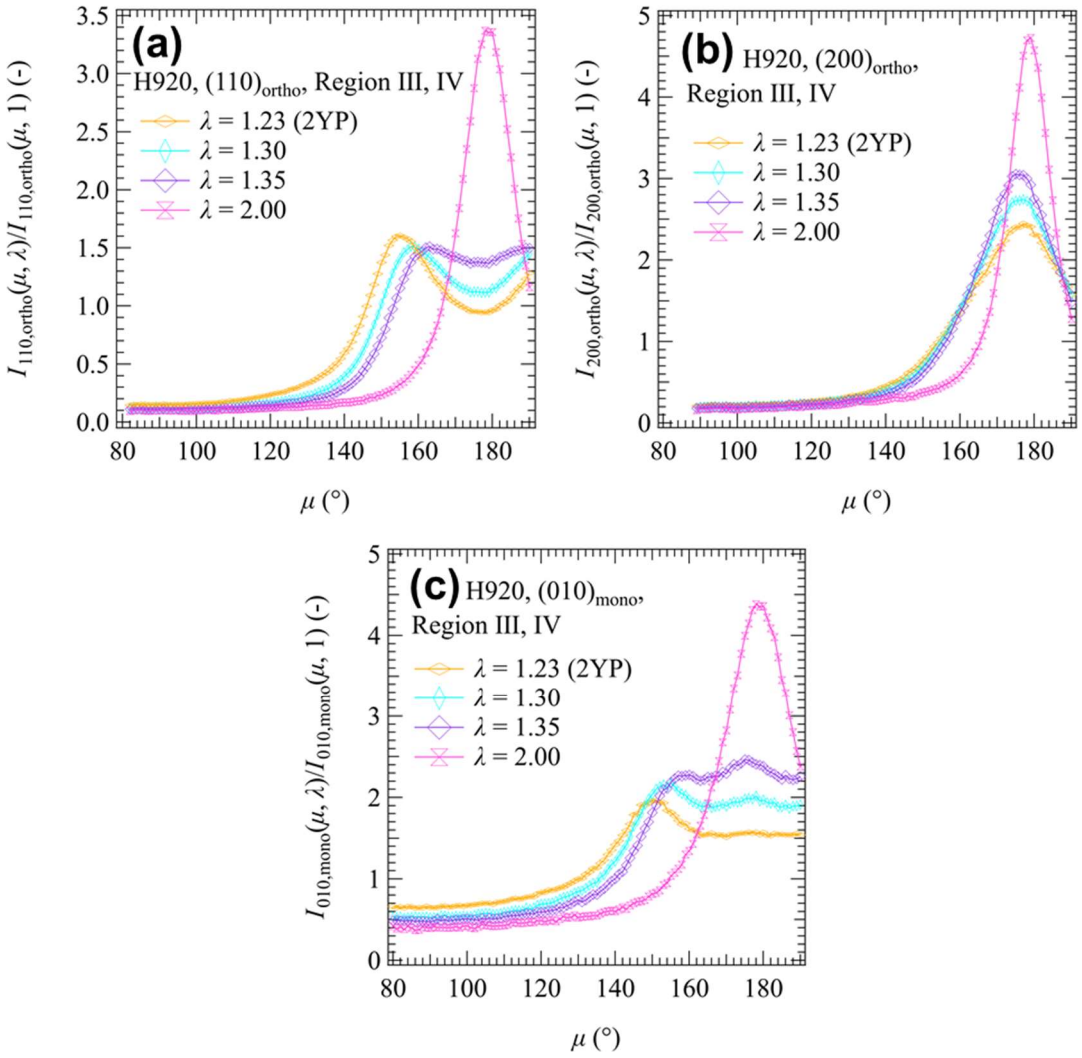

Figure 5.9 μ dependence of (a) $I_{110,ortho}(\mu, \lambda)/I_{110,ortho}(\mu, 1)$, (b) $I_{200,ortho}(\mu, \lambda)/I_{200,ortho}(\mu, 1)$, and (c) $I_{010,mono}(\mu, \lambda)/I_{010,mono}(\mu, 1)$ in WAXS patterns in Region III and IV in H920.

into a fibrillar structure completely, which was shown in the disappearance of the four-point pattern in the SAXS pattern (Figure 5.4(p)). The peaks at μ =180° in the WAXS patterns increased with the strain, as shown in Figure 5.9, suggesting that the orientation of the lattice structure along the parallel direction progressed with the strain.

5.3.4 Changes in the Hierarchical Structures of B920

The 2D USAXS, SAXS, and WAXS patterns are shown in Figures 5.10 and 5.15 as a function of the strain for the B920 and B935, respectively. I also show the combined USAXS and SAXS profiles along with the directions parallel and perpendicular to the stretching axis for the B920 and B935 in Figures 5.11 and 5.16, respectively.

The changes in the scattering patterns with strain can be classified into the following 3 regions. Region I: strain domain at $\lambda < 1.04$ ($\lambda = 1.04$ is not at 1YP), Region II: strain domain at $1.04 < \lambda < 1.26$ (2YP), Region III: strain domain after the 2YP or at $1.26 < \lambda$.

Region I (B920)

In Region I ($\lambda < 1.04$), the strain induced the inhomogeneous deformation on the submicron scale as well as the deformation of the lamellar structures. In the USAXS patterns (Figures 5.10(a)–(c)), the intensity along the parallel direction increased with strain. The increase along stretching direction indicates the inhomogeneous deformation between the high-crystallinity region (HCR) and the low-crystallinity region (LCR), but a clear butterfly pattern was not observed. The plot of $D_i(\lambda)/D_i(1)$ vs λ in Figure 5.12(a) deviated from affine deformation even smaller λ in Region I as in the case of H920. On the other hand, mechanical melting did not occur in B920 in contrast to in H920 (see Figure 5.12(b)). The reason for the deviation from affine deformation was the inhomogen-

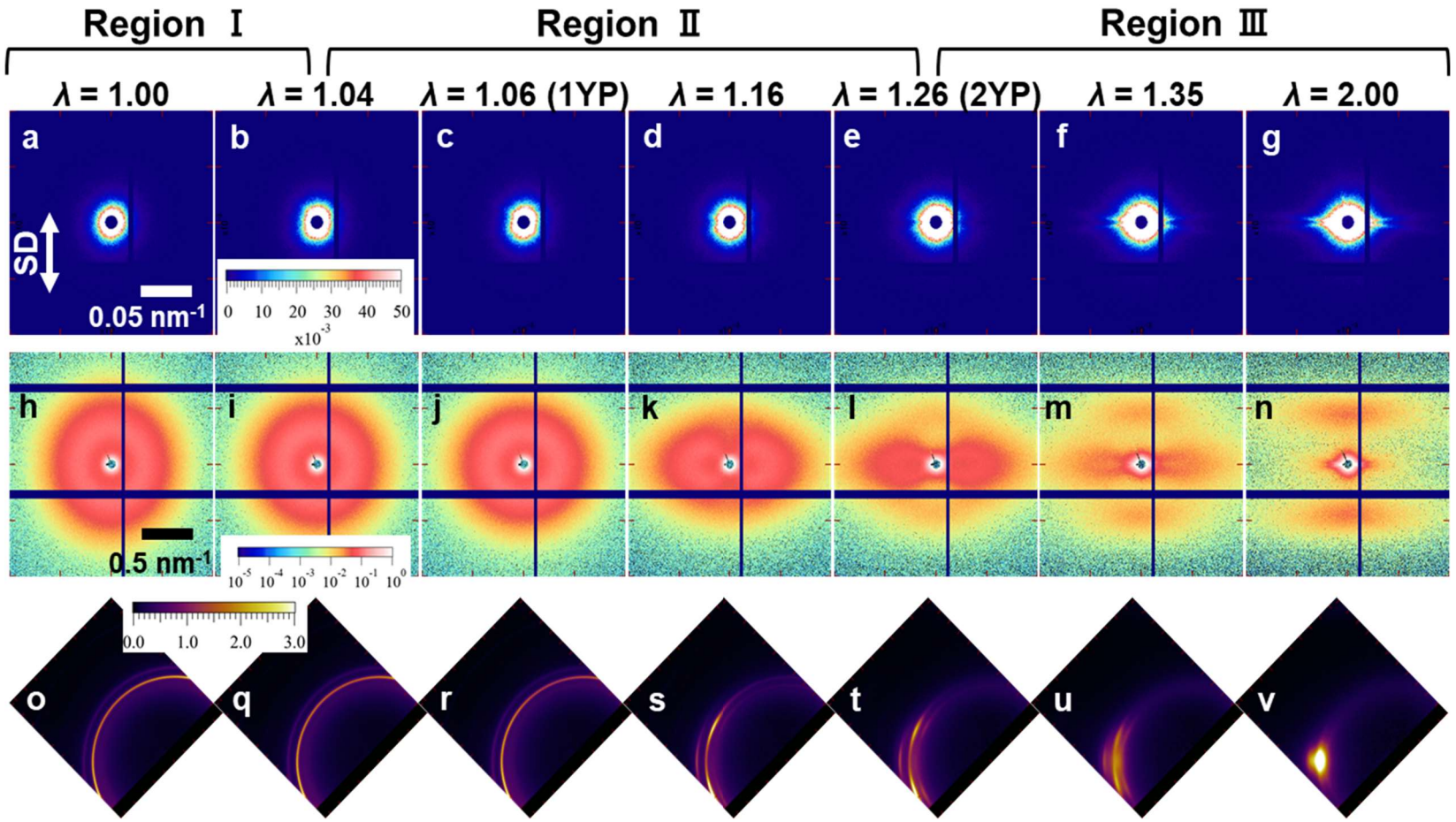

Figure 5.10 (a)–(h) USAXS, (i)–(p)SAXS, and (q)–(x)WAXS 2D patterns of B920 with strain. The arrow in part(a) corresponds to the stretching direction.

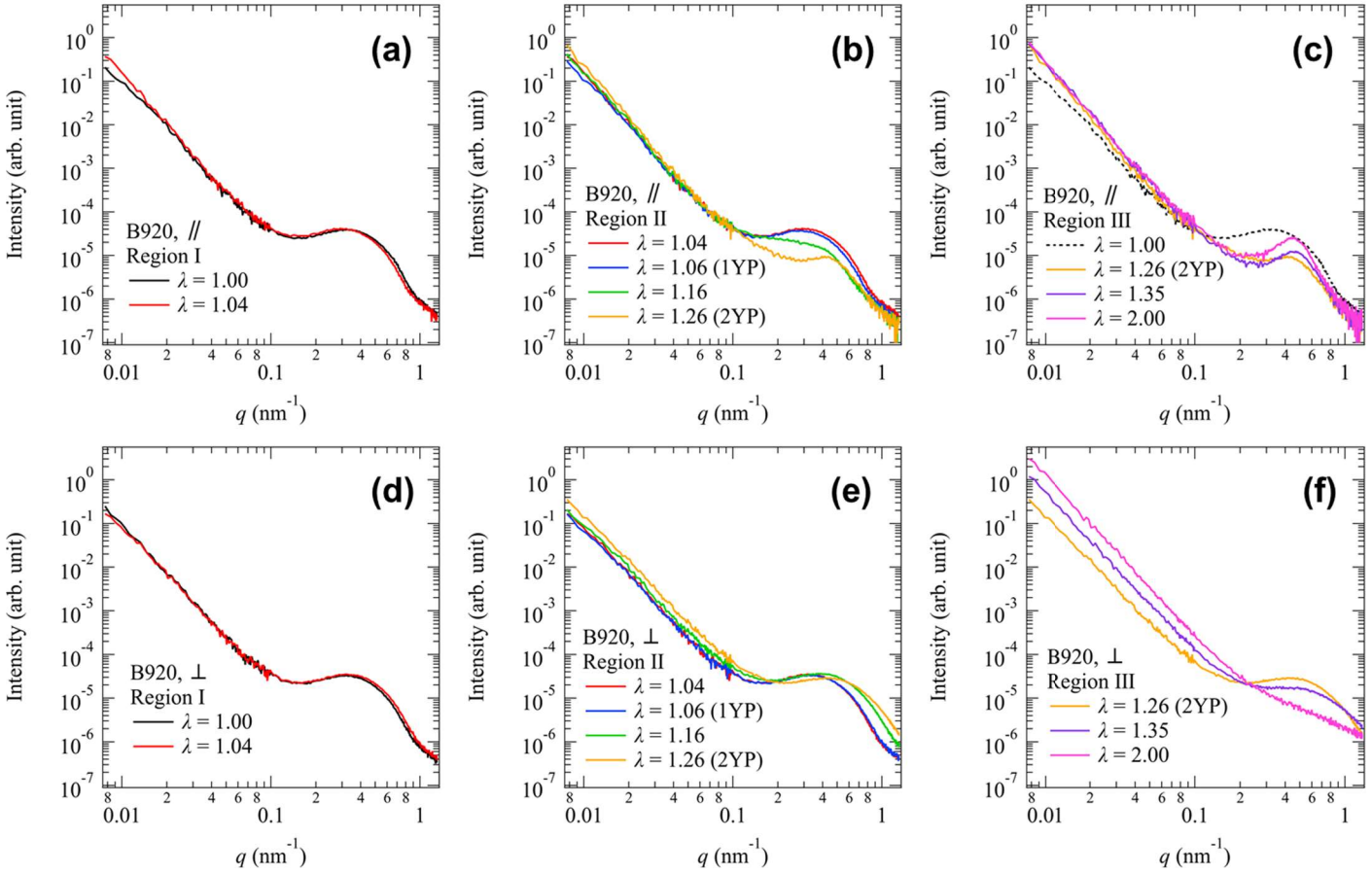

Figure 5.11 Combined USAXS and SAXS profiles from B920 in (a) and (d) Region I, (b) and (e) Region II, and (c) and (f) Region III, respectively. The profiles in (a), (b), and (c) and (d), (e), and (f) correspond to the scattering intensities parallel and perpendicular to the stretching directions, respectively.

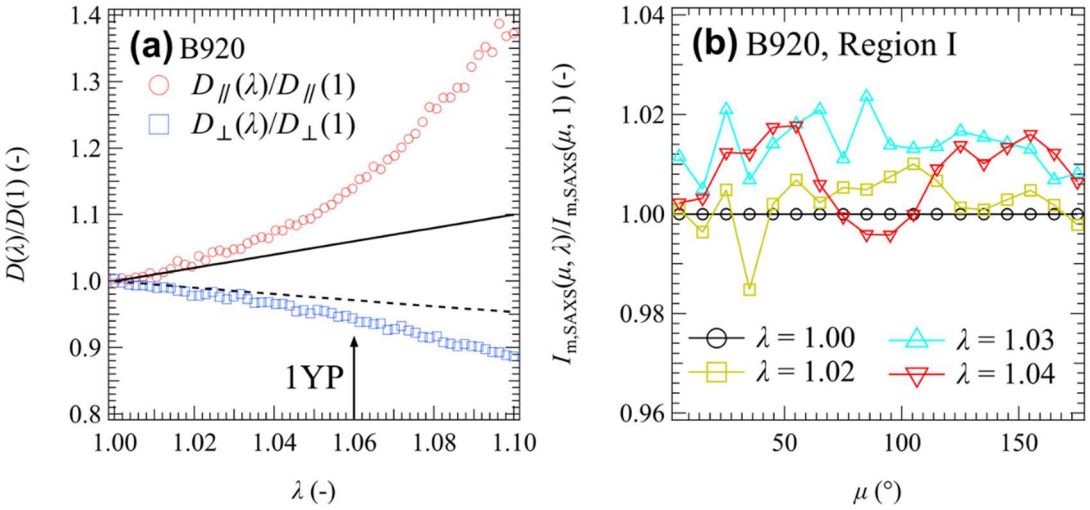

Figure 5.12 (a) λ dependence of $D_{//}(\lambda)/D_{//}(1)$ and $D_{\perp}(\lambda)/D_{\perp}(1)$ of B920. The solid and dashed lines are the lines calculated by Eqs. (5.6) and (5.7) obeying affine deformation. (b) μ dependence of the reduced peak intensity $I_{m,SAXS}(\mu, \lambda)/I_{m,SAXS}(\mu, 1)$ of SAXS patterns in Region I in B920.

eous deformation. The lamellar structures in the LCR deformed larger than that in the HCR, and the deviation reflected the lamellar structures in the LCR.

Region II (B920)

In Region II ($1.04 < \lambda < 1.26$ (2YP)), the strain developed a chevron-type morphology and enhanced the density fluctuations on the submicron scale. The abnormal butterfly patterns were observed in USAXS patterns and profiles (Figures 5.10(c)–(e) and 5.11(b)), originating from the inhomogeneous deformation as described above. In the SAXS pattern (Figures 5.10(j)–(l)), the four-point patterns characterizing the lamellar fragmentation and rotation developed. Besides, the azimuthal dependence of the SAXS peak in Figure 5.13(a) indicates that mechanical melting occurred in Region II. The WAXS peaks (Figures 5.10(r)–(t)) were also split and the $(110)_{ortho}$ and $(010)_{mono}$ planes oriented diagonally (Figures 5.13(b) and (d)) according to

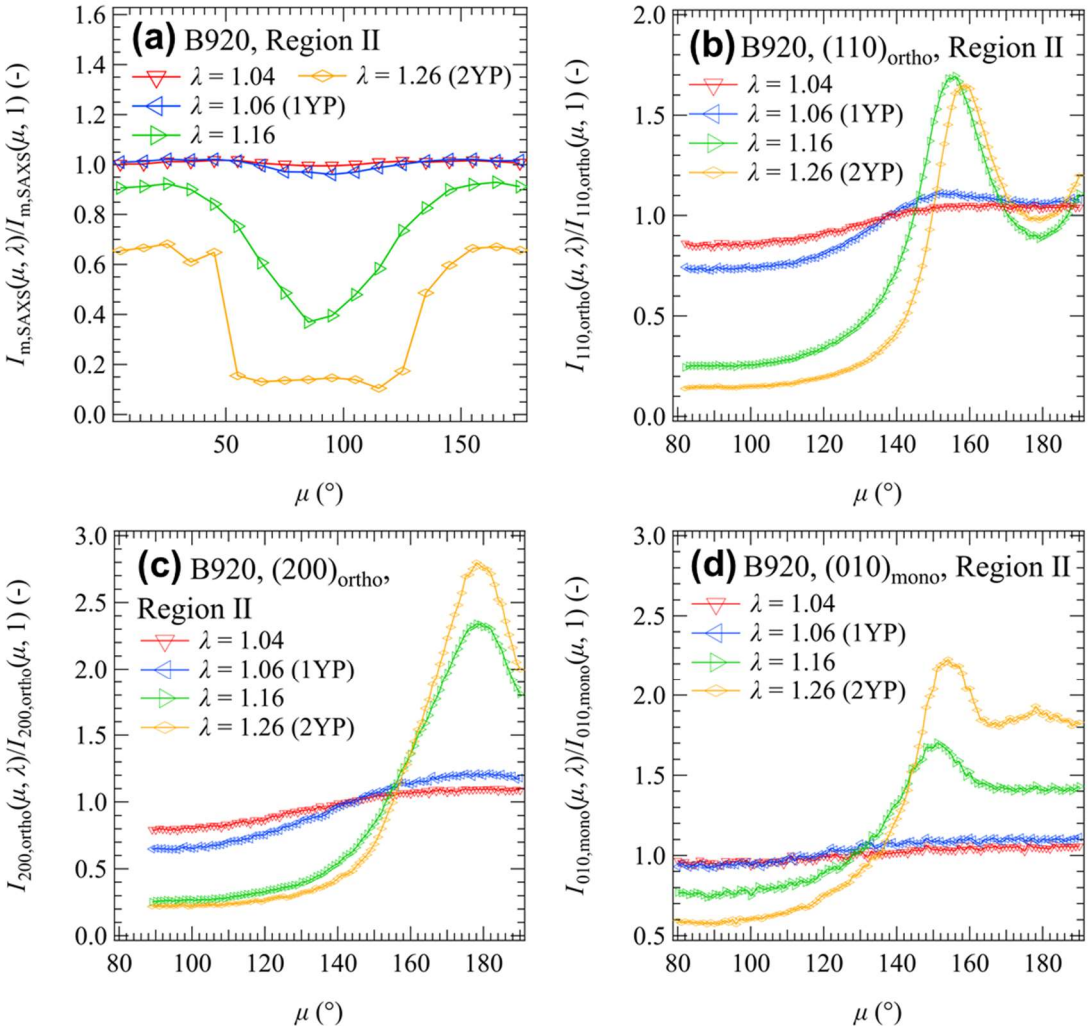

Figure 5.13 μ dependence of (a) the reduced peak intensity $I_{m,SAXS}(\mu, \lambda)/I_{m,SAXS}$ (μ, 1) of SAXS patterns, (b) $I_{110,ortho}(\mu, \lambda)/I_{110,ortho}(\mu, 1)$, (c) $I_{200,ortho}(\mu, \lambda)/I_{200,ortho}(\mu, 1)$, and (d) $I_{010,mono}(\mu, \lambda)/ I_{010,mono}(\mu, 1)$ in WAXS patterns in Region II in B920.

the development of the chevron-type morphology. In contrast, the orientation of the $(200)_{ortho}$ plane in μ = 180˚ progressed (Figure 5.13(c)) as in H920, reflecting the realignment of the polymer chains in the mechanically melted region.

Region III (B920)

In Region III, inhomogeneous structure or voids on the submicron scale elongated along the parallel direction, and the chevron-type morphology transformed into a fibrillar structure. The streaks elongated to the perpendicular direction were found in USAXS patterns as shown in Figures 5.10(e)–(g), and profiles in Figure 5.11(f). The change in the USAXS pattern indicates the inhomogeneous structures or voids elongated to the direction parallel to the stretching direction. In the SAXS patterns (Figures 5.10(l)–(n)), the four-point pattern decreased with strain, associating with mechanical melting. At the 2YP, a broad peak increased at approximately q = 0.4 nm^{-1} in the parallel direction with strain, supporting the formation of the fibrillar structure. The WAXS patterns (Figures 5.10(t)–(v)) and μ dependences of the diffraction peaks (Figures 5.14(a) and (c)) show the $(110)_{ortho}$ and $(010)_{mono}$ peaks corresponding to the four-point pattern decreased while the peak intensity at μ = 180° increased with strain. The μ dependence of the $(200)_{ortho}$ peak (Figure 5.14(b)) was not split and the intensity at μ = 180° monotonically increased with strain. These changes in the WAXS patterns also supported the formation of the fibrillar structure.

5.3.5 Changes in the Hierarchical Structures of B935

The changes in the scattering patterns with strain can be classified into the following 4 regions. Region I: strain domain before the 1YP or at λ < 1.07 (1YP), Region II: strain domain at 1.07 (1YP) < λ < 1.15 (2YP), Region III: strain domain after the 2YP

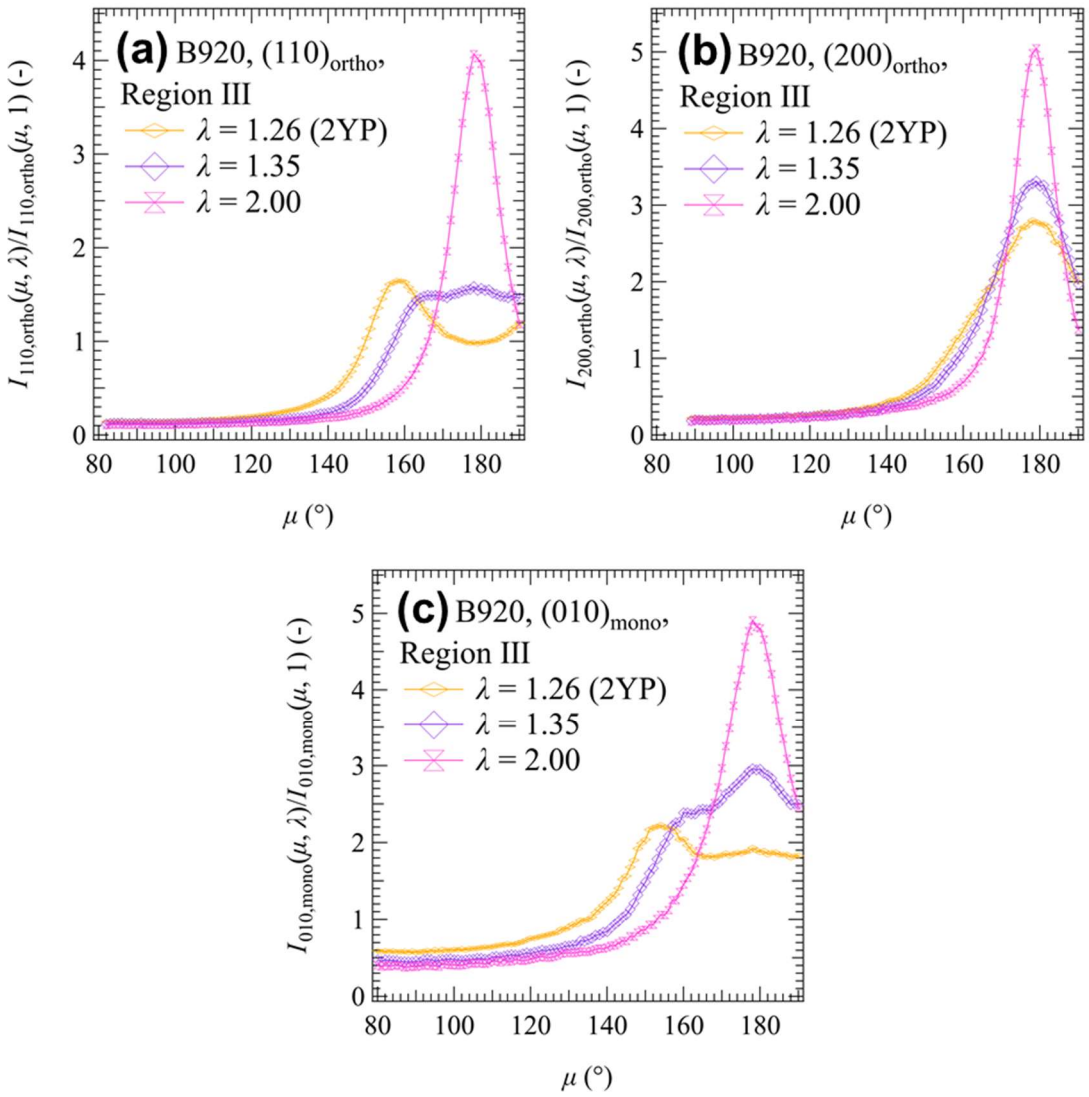

Figure 5.14 μ dependence of (a) $I_{110,ortho}(\mu, \lambda)/I_{110,ortho}(\mu, 1)$, (b) $I_{200,ortho}(\mu, \lambda)/I_{200,ortho}(\mu, 1)$, and (c) $I_{010,mono}(\mu, \lambda)/I_{010,mono}(\mu, 1)$ in WAXS patterns in Region III in B920.

or at 1.15 < λ <1.40, and Region IV: strain domain at 1.40 < λ.

Region I (B935)

In Region I (λ < 1.07 (1YP)), strain induced affine deformation in lamellar structures and elongation of the inhomogeneous structures on the submicron scale. Little change was observed in USAXS (Figures 5.15(a) and (b)) and SAXS patterns (Figures 5.15(i) and (j)) with strain in Region I. However, I was able to find the changes in $I_{\parallel}(q)$ and $I_{\perp}(q)$ (Figures 5.16(a) and (e)). $I_{\perp}(q)$ in the USAXS region increased with strain while $I_{\parallel}(q)$ in the USAXS region did not change, suggesting that the affine deformation occurred on the submicron scale. As shown in Figure 5.17(a), the changes in $D_{\parallel}$ and $D_{\perp}$ showed the affine deformation in the SAXS region as well. The μ dependence of the SAXS peak intensities (Figure 5.17(b)) did not show the four-point pattern while it had a maximum at μ = 90°. Hence, the lamellar fragmentation did not occur in this region. The peak at μ = 90° in Figure 5.17(b) probably reflects the increase in the volume of the lamellar structure associated with the change in $D_{\parallel}$ (Figure 5.17(a)). The μ dependences of the diffraction peak intensities from the $(110)_{ortho}$ and $(200)_{ortho}$ planes in Figures 5.17(c) and (d), respectively, show the orientation of the lattice structure did not change much with the strain. The slight decrease in the intensities at μ = 90° indicates that mechanical melting hardly occurred in this region.

Region II (B935)

In Region II (1.07 (1YP) < λ < 1.15 (2YP)), The little change in the SAXS patterns with strain was observed in Figures 5.15(k) and (l). The profiles in Figures 5.16 (b) and (f) did not show the change clearly. The peak position did not shift with strain (Figure 5.17(a)) and the deformation of the lamellar structure did not follow the affine deformation. Contrary to the case of H920 and B920 with lower crystallinity, the deforma-

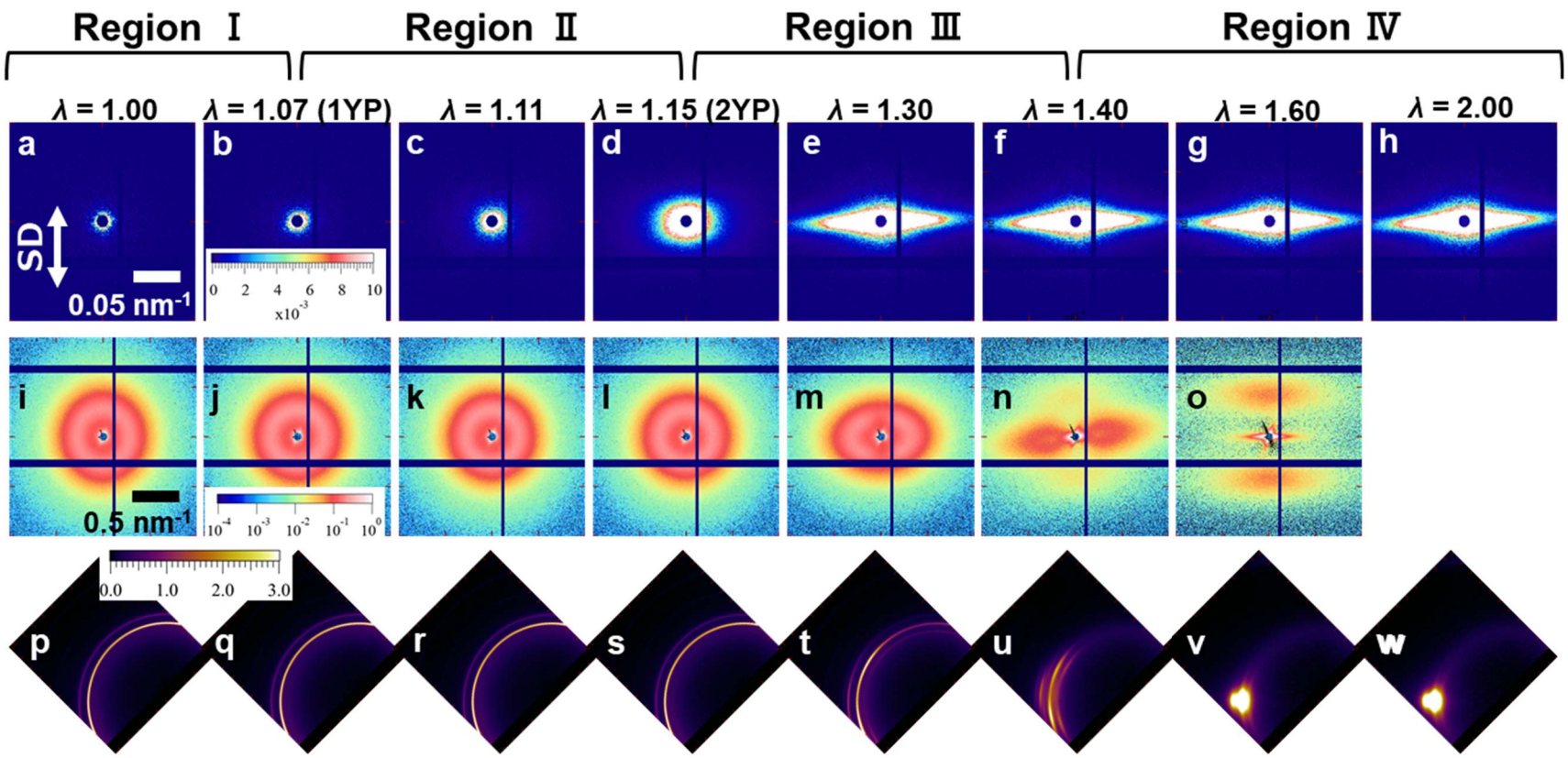

Figure 5.15 (a)–(h) USAXS, (i)–(p)SAXS, and (q)–(x)WAXS 2D patterns of B935 with strain. The arrow in part(a) corresponds to the stretching direction.

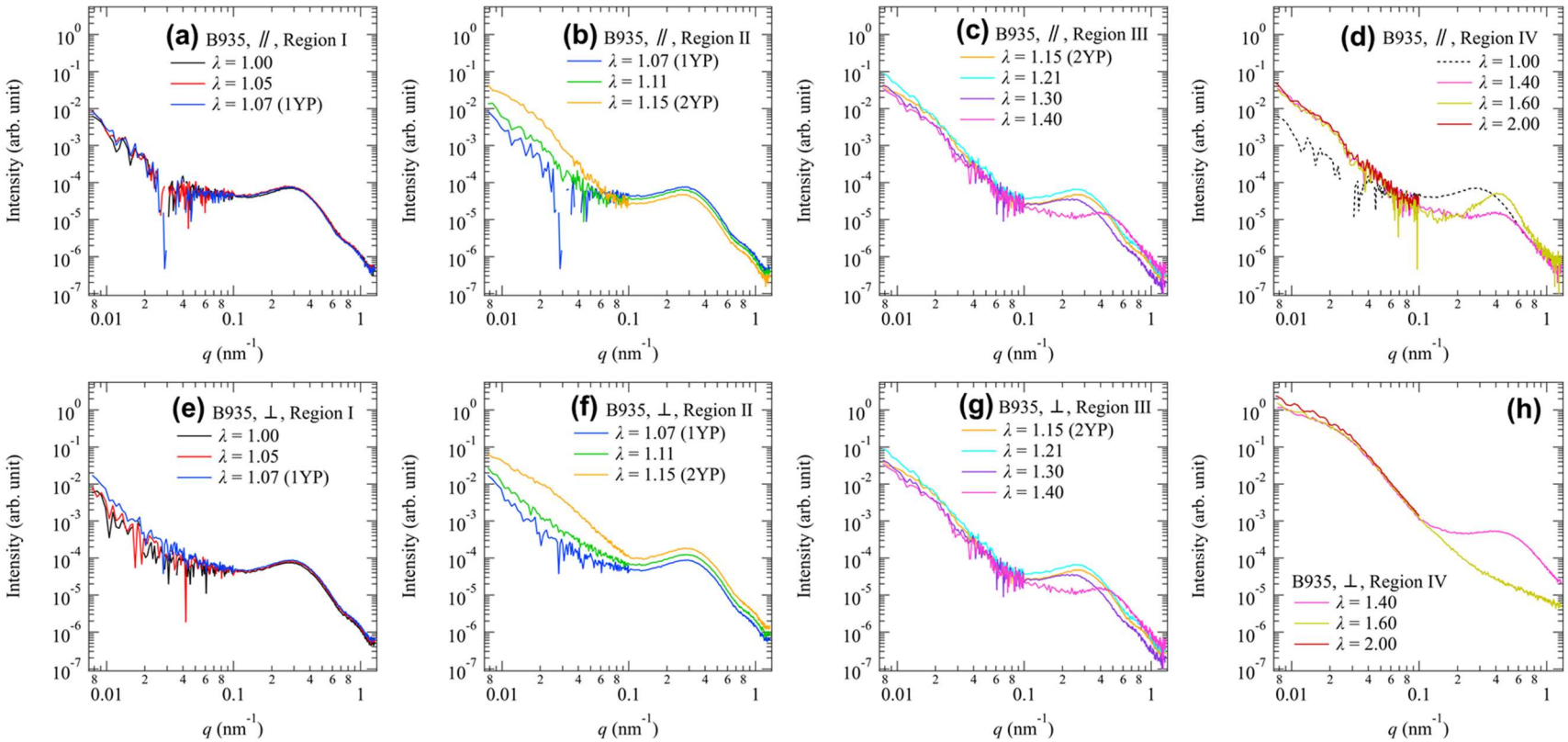

Figure 5.16 Combined USAXS and SAXS profiles from B935 in (a) and (e) Region I, (b) and (f) Region II, (c) and (g) Region III, and (d) and (h) Region IV, respectively. The profiles in (a), (b), (c), and (d) and (e), (f), (g), and (h) correspond to the scattering intensities parallel and perpendicular to the stretching directions, respectively.

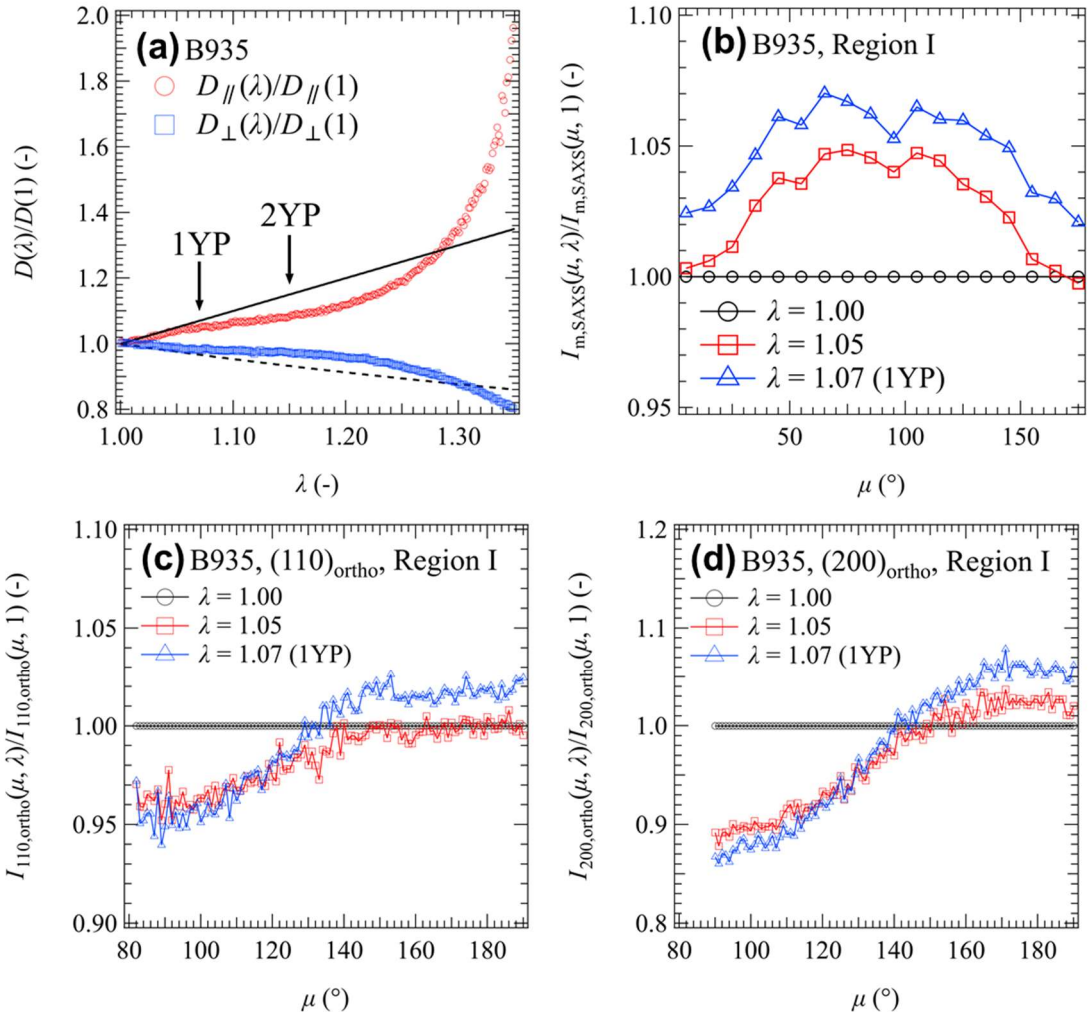

Figure 5.17 (a) λ dependence of $D_{//}(\lambda)/D_{//}(1)$ and $D_{\perp}(\lambda)/D_{\perp}(1)$ of B935. The solid and dashed lines are the lines calculated by Eqs. (5.6) and (5.7) obeying affine deformation. μ dependence of (b) the reduced peak intensity $I_{m,SAXS}(\mu, \lambda)/I_{m,SAXS}(\mu, 1)$ of SAXS, (c) $I_{110,ortho}(\mu, \lambda)/I_{110,ortho}(\mu, 1)$, and (d) $I_{200,ortho}(\mu, \lambda)/I_{200,ortho}(\mu, 1)$ in WAXS patterns in Region I in B935.

tion was much suppressed. Figure 5.18(a) showed that lamellar fragmentation started and slowly proceeded in this region. The diffraction peak intensities from the $(110)_{ortho}$ and $(200)_{ortho}$ planes in Figures 5.18(b) and (c) did not change much with the strain. On the other hand, the increase in the intensity in the USAXS pattern was observed in Figures 5.15(c) and (d). The patterns were elongated to the direction perpendicular to the stretching direction. The orientation of the scattering pattern was different from those observed in H935 and B920, which contributed to suppressing the enhancement. As described above, the strength of enhancement depends on the amplitude of the initial inhomogeneity of the density fluctuations. I think that the voids in B935 appeared at the defects in the sample and elongated with strain.

Region III (B935)

In Region III or 2YP or at $1.15 < \lambda < 1.40$, the voids were strongly elongated to the stretching direction and a chevron-type morphology was developed. In the USAXS patterns (Figures 5.15(d)–(f)), the elongated patterns became the streak patterns. The intensity increased drastically, indicating that the elongated voids were formed in this region. On the scale of the lamellar structures (Figures 5.15(m) and (n)), the diagonal characteristic patterns were observed referred to as four-point patterns, attributing to the lamellar fragmentation and rotation. Figures 5.19(a) makes it clear the formation of the four-point pattern. The diagonal orientation of the $(110)_{ortho}$ and $(010)_{mono}$ peaks in the WAXS patterns (Figures 5.15(t) and (u) and Figures 5.19(b) and (d)) supports the chevron-type morphology and the increase in the $(200)_{ortho}$ peak oriented to the perpendicular direction reflects the realignment of the melted chains (Figures 5.19(c)).

Region IV (B935)

In Region IV or $1.40 < \lambda$, the void grew with strain on the submicron scale and

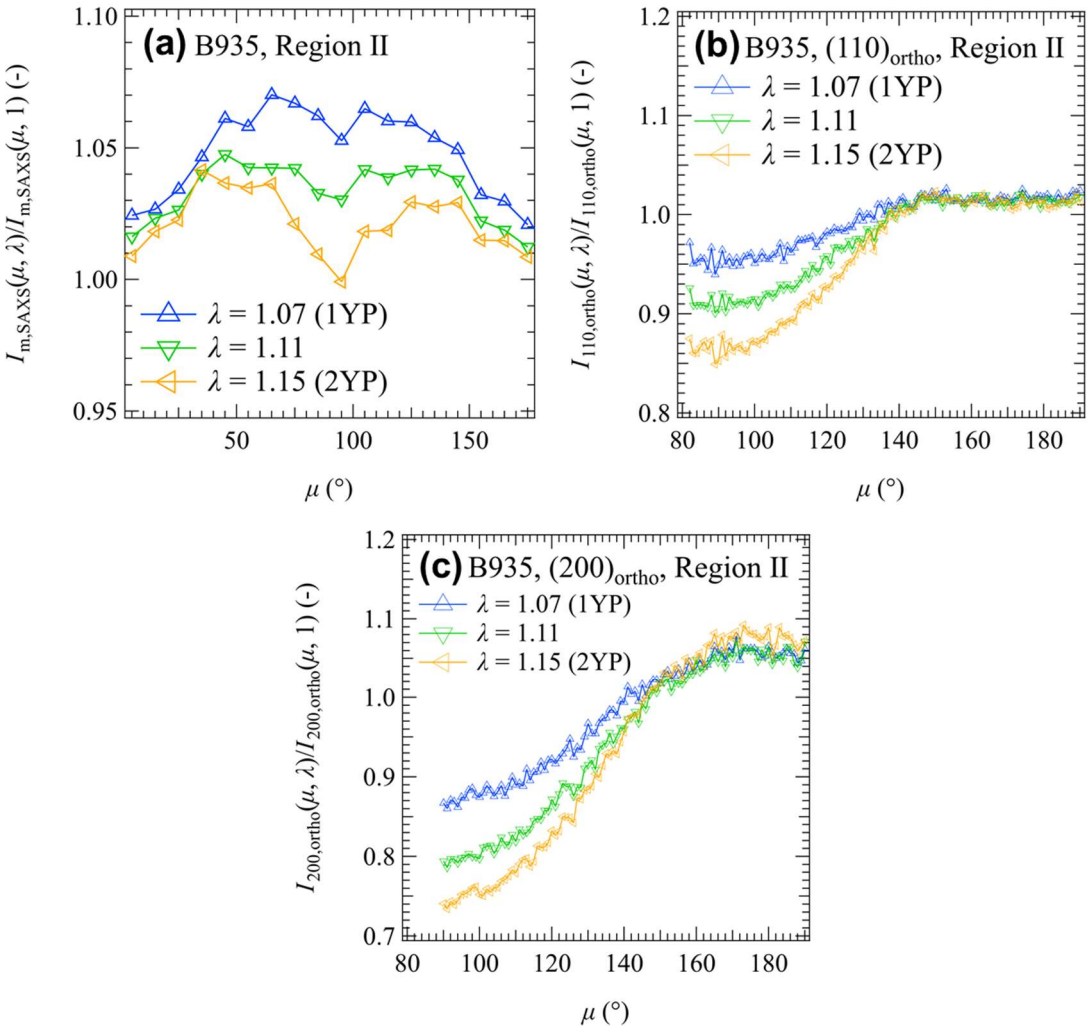

Figure 5.18 μ dependence of (a) the reduced peak intensity $I_{m,SAXS}(\mu, \lambda)/I_{m,SAXS}(\mu, 1)$ of SAXS patterns, (b) $I_{110,ortho}(\mu, \lambda)/I_{110,ortho}(\mu, 1)$, and (c) $I_{200,ortho}(\mu, \lambda)/I_{200,ortho}(\mu, 1)$ in WAXS patterns in Region II in B935.

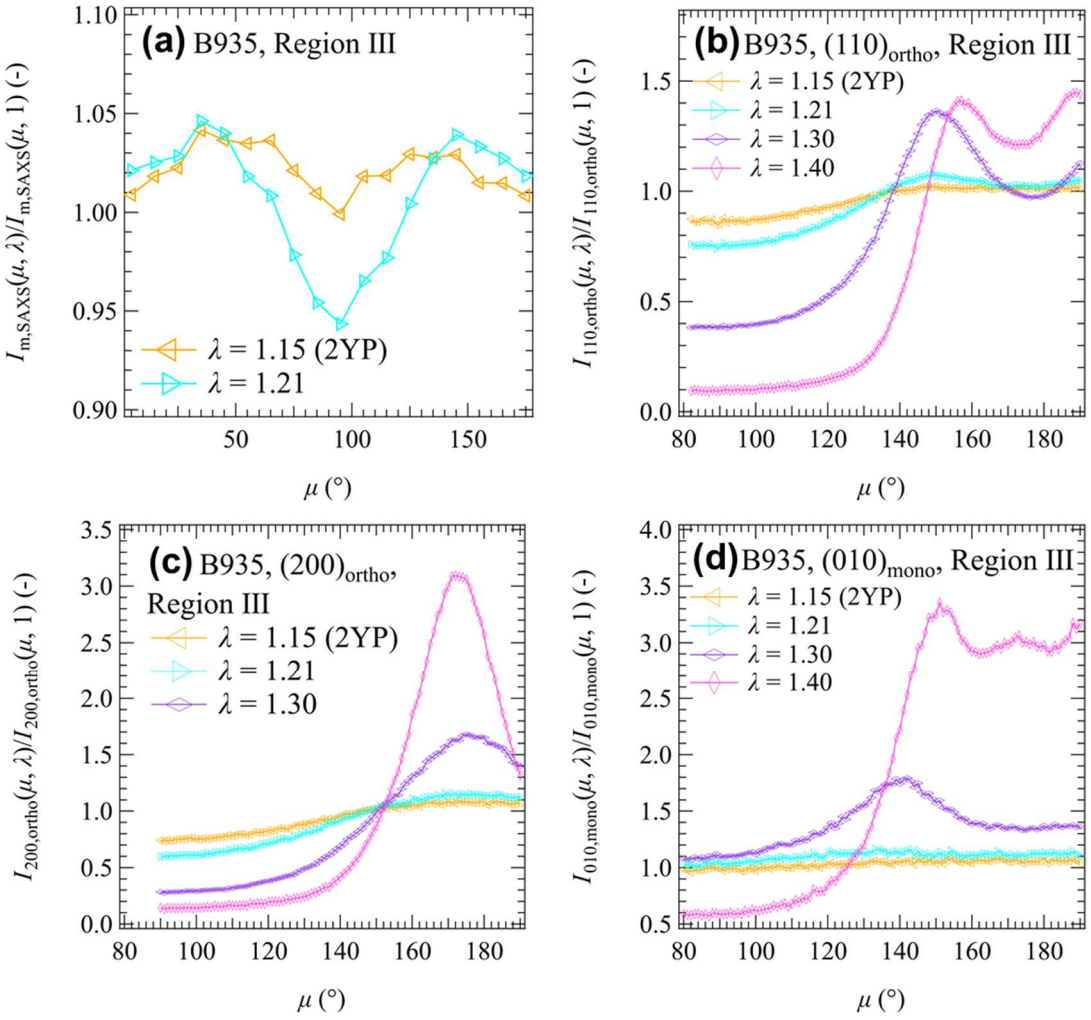

Figure 5.19 μ dependence of (a) the reduced peak intensity $I_{m,SAXS}(\mu, \lambda)/I_{m,SAXS}(\mu, 1)$ of SAXS patterns, (b) $I_{110,ortho}(\mu, \lambda)/I_{110,ortho}(\mu, 1)$, (c) $I_{200,ortho}(\mu, \lambda)/I_{200,ortho}(\mu, 1)$, and (d) $I_{010,mono}(\mu, \lambda)/ I_{010,mono}(\mu, 1)$ in WAXS patterns in Region III in B935.

the chevron-type morphology transformed into a fibrillar structure. The streak patterns in the USAXS (Figures 5.15(f)–(h)) increased with strain, reflecting the growth of the voids. In the SAXS patterns (Figures 5.15(n) and (o)), the gradual fading of the four-point pattern and the appearance of the broad peaks were observed at approximately q = 0.4 nm^{-1} in the parallel direction, indicating the formation of the fibrillar structure. As shown in the WAXS patterns (Figures 5.15(u)–(w)) and μ dependences of the diffraction peaks (Figures 5.20(a) and (c)), the $(110)_{ortho}$ and $(010)_{mono}$ peaks corresponding to the four-point pattern decreased while the peak intensity at μ = 180° increased with strain. The μ dependence of the $(200)_{ortho}$ peak (Figure 5.20(b)) also shows that the intensity at μ = 180° increased with strain. These changes also support the formation of a fibrillar structure.

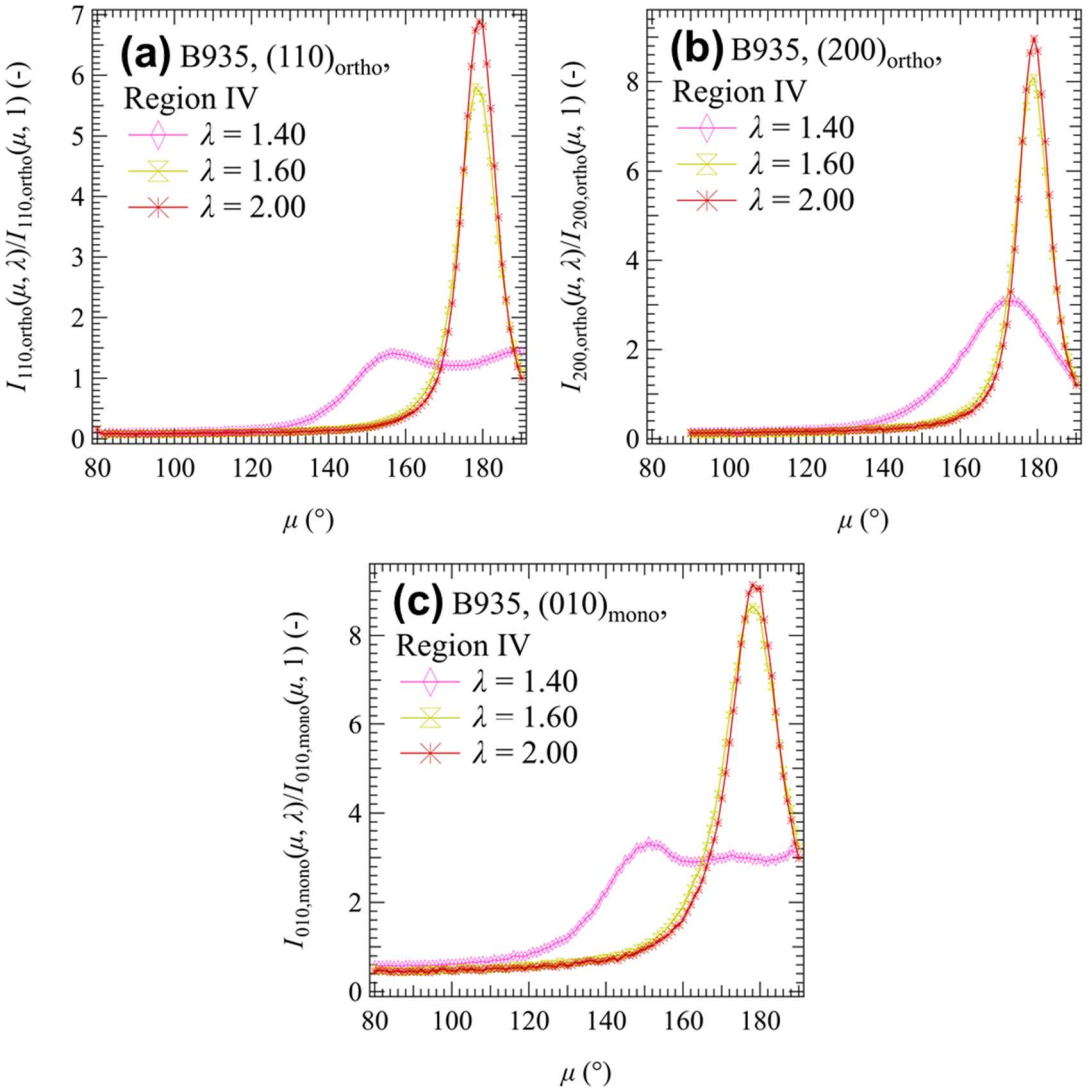

Figure 5.20 μ dependence of (a) $I_{110,ortho}(\mu, \lambda)/I_{110,ortho}(\mu, 1)$, (b) $I_{200,ortho}(\mu, \lambda)/I_{200,ortho}(\mu, 1)$, and (c) $I_{010,mono}(\mu, \lambda)/I_{010,mono}(\mu, 1)$ in WAXS patterns in Region IV in B935.

5.3.6 Effects of the comonomer characteristics on strain-induced density fluctuations in LLDPE

In this section, I focus on the change in USAXS patterns and clarify how the comonomer characteristic affects the SIDF behaviors. The USAXS patterns and profiles parallel and perpendicular to the stretching direction of H920, B920, and B935 with strain are shown in Figures 5.21 and 5.22.

First, I briefly describe the structural changes observed in H935 by USAXS as described in Chapter 4. H935 exhibited the abnormal butterfly pattern that characterizes the SIDF after the 1YP as shown in Figure 5.21(g). The appearance of the abnormal butterfly pattern originates from the inhomogeneous deformation as observed in other systems.[2-7,19-21] In the case of polyethylene, this pattern reflects the difference in the amount of deformation between the HCR and LCR on the scale of the lamellar branching structure. The butterfly pattern finally transformed into the streak pattern after 2YP as shown in Figure 5.21(h), indicating that the density fluctuations were transformed into the voids elongated to the parallel direction at 2YP.

In contrast to H935, H920 did not exhibit the butterfly pattern as shown in Figures 5.21(a)–(c). The profiles in Figures 5.22(a) and (b) also indicate that the changes in the submicron structure did not occur with strain. At large strain region, very weak streak scattering appeared as seen in Figure 5.21(d), suggesting that a much smaller number or size of voids were generated in H920 than in H935.

In the case of B920, the butterfly pattern appeared with strain in Figures 5.21(j) and (k). The $I_{\parallel}(q)$ in Figure 5.22(e) also increased with strain. Finally, the streak pattern (Figure 5.21(l)) and the corresponding enhancement in the $I_{\perp}(q)$ (Figure 5.22(f)) were observed. These results support the emergence of the voids associating with the SIDF.

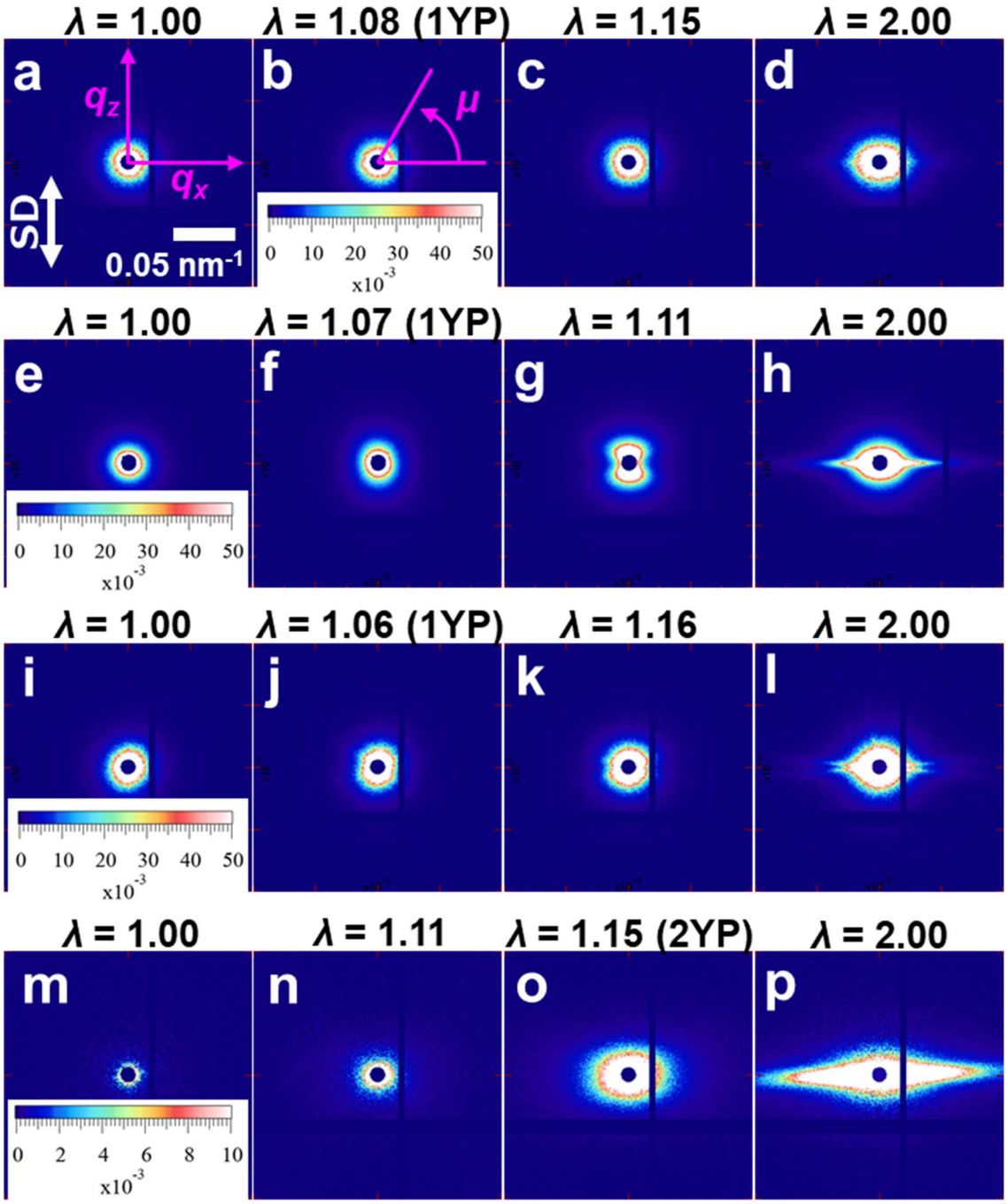

Figure 5.21 Representative USAXS 2D patterns of (a)–(d)H920, (e)–(h)H935, (i)–(l)B920, and (m)–(p)B935 with strain, respectively. The q_y-axis is parallel to the incident beam, that is, normal to these scattering patterns. SD in part(a) is short for the stretching direction.

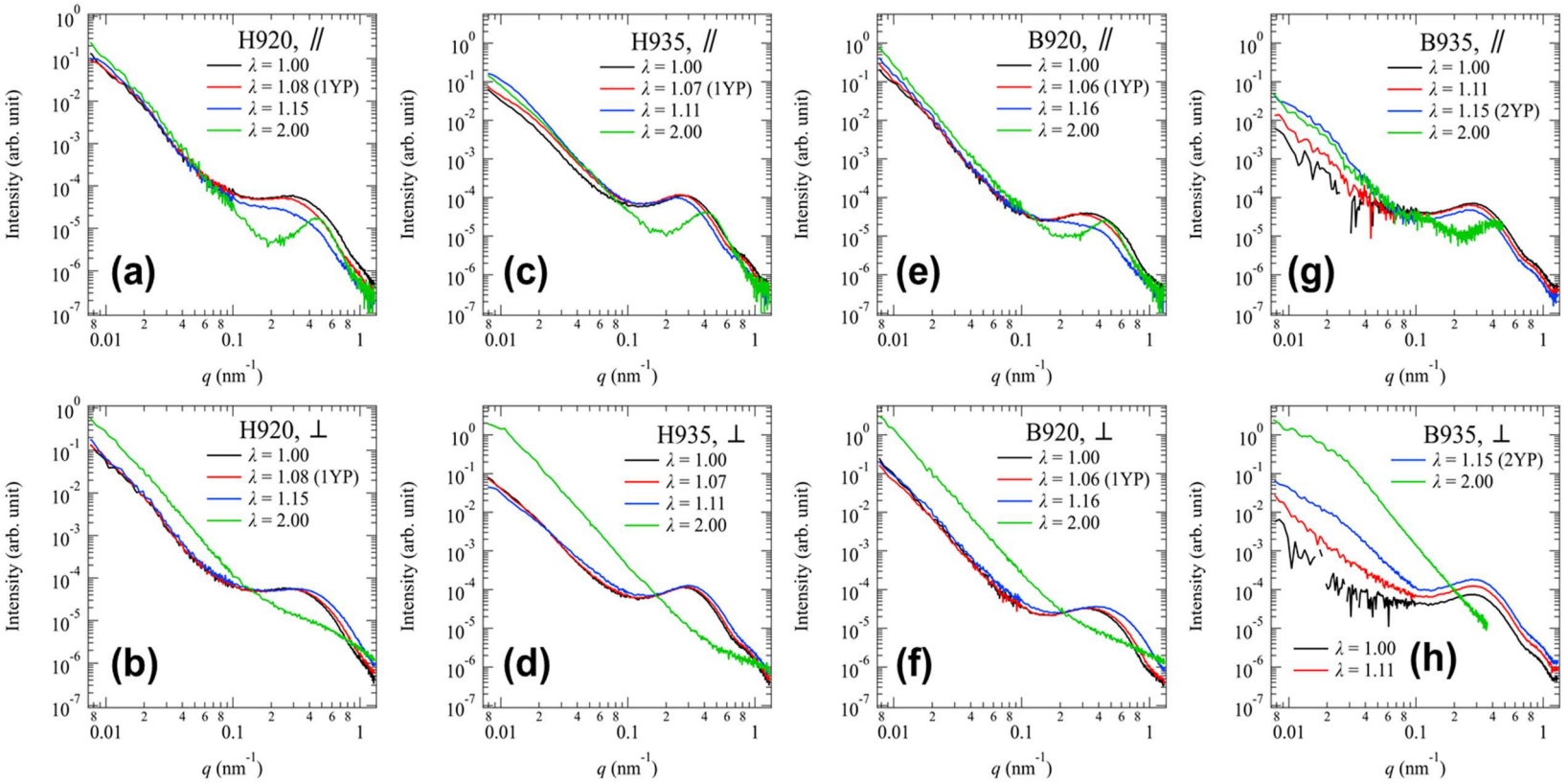

Figure 5.22 Combined USAXS and SAXS profiles for (a)(b)H920, (c)(d)H935, (e)(f)B920, and (g)(h)B935. The profiles in (a)(c)(e)(g) and (b)(d)(f)(h) correspond to the scattering intensities parallel and perpendicular to the stretching directions, respectively.

In the case of B935, the butterfly pattern did not appear, but an elliptical pattern with a major axis perpendicular to the stretching direction developed until the 2YP in Figures 5.21(m)–(o). After the 2YP, the strong streak scattering appeared along the direction perpendicular to the stretching direction (Figure 5.21(p)). These results suggest that the SIDF did not occur with strain. Instead, the initial density fluctuations on the submicron scale were elongated to the stretching direction and the elongated fluctuations became voids.

To analyze the behaviors of the SIDF quantitatively, I calculated the changes in the invariant during stretching. I assumed the scattering intensity distribution is symmetrical along the q_z-axis or the stretching axis under uniaxial stretching and calculated the invariant on the submicron scale during uniaxial stretching ($Q_{\mathrm{U,uni}}$) from the USAXS patterns by using

$$Q_{\mathrm{U,uni}}(\lambda) = -2\pi \int_{\mu=\frac{5}{12}\pi}^{\frac{7}{12}\pi} \int_{q=0.0075}^{0.0628} qI(q,\mu,\lambda)\cos\mu \,\mathrm{d}q\mathrm{d}\mu \tag{5.8}$$

Figure 5.23 shows the changes in the $Q_{\mathrm{U,uni}}(\lambda)$ with strain. The drastic increase in $Q_{\mathrm{U,uni}}(\lambda)$ was found in H935 and B920 exhibiting the butterfly patterns while $Q_{\mathrm{U,uni}}(\lambda)$ became almost constant with strain at $\lambda < 1.15$ for H920. The $Q_{\mathrm{U,uni}}(\lambda)$ upturned in association with the butterfly patterns approximately from $\lambda = 1.03$ in B920 and from $\lambda = 1.06$ in H935, respectively. The growth rates were indicated by broken lines in Figure 5.23. The growth rate of H935 was larger than that in B920, suggesting the SIDF of H935 was more distinct than that of B920. As for the case of B935, the increase in $Q_{\mathrm{U,uni}}(\lambda)$ was observed approximately from $\lambda = 1.11$. However, this increase was caused by the

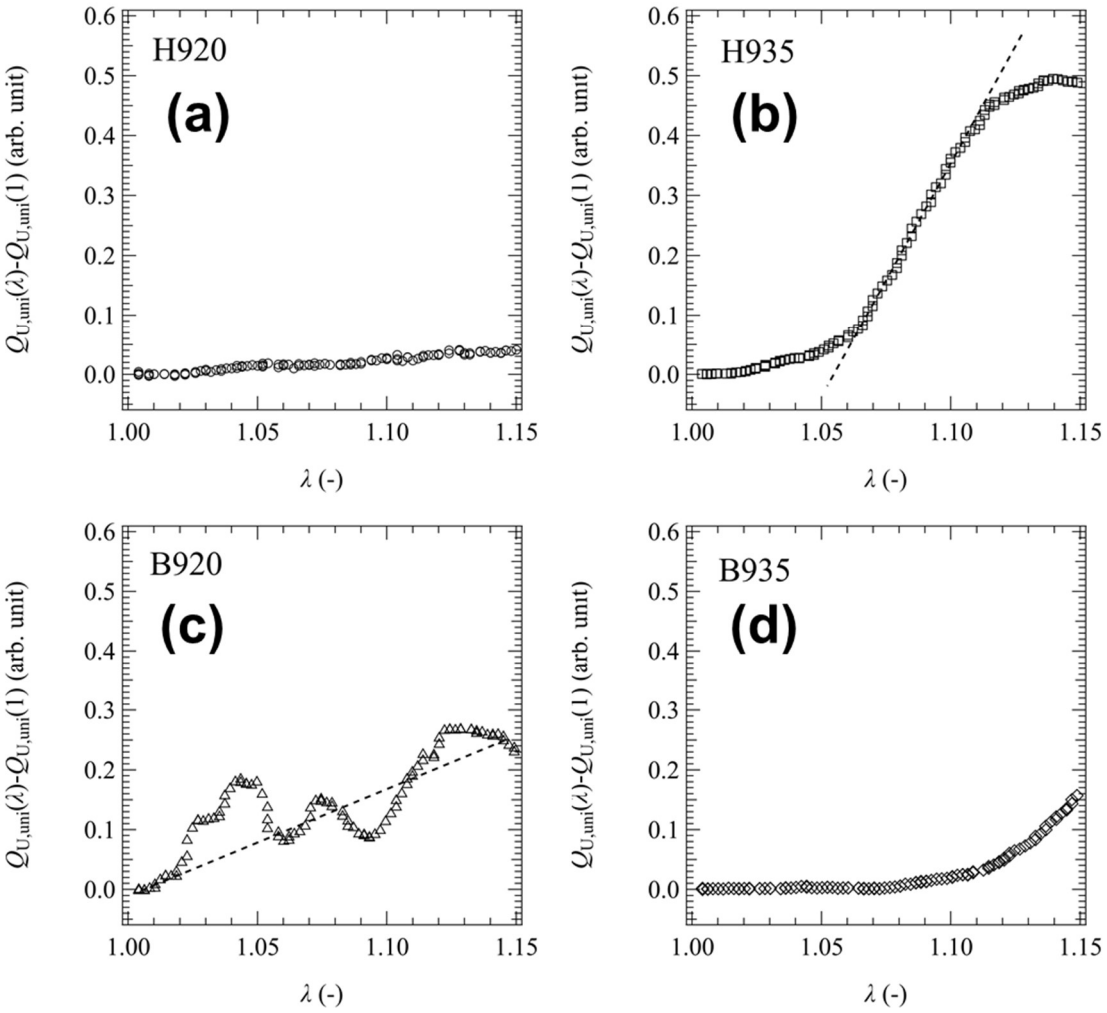

Figure 5.23 Evolution of the SIDF characterized by the invariant during uniaxial stretching in (a)H935 and (b)B920, respectively. The broken lines are guides to the

formation of the voids and the origin of the increase was not the SIDF as described before.

As shown in Figure 5.23, the SIDF occurred in H935 and B920 while H920 and B935 did not show the SIDF behaviors. The SIDF in H935 was stronger than that in B920. As described previously, the driving force is proportional to the gradient of the stress fields and increases with the inhomogeneity or the invariant at the initial state. Thus, the absence of the SIDF in B935 is attributed to the homogeneous submicron structure at the initial state. However, we cannot explain the following facts: (i) H920 did not show the SIDF though the invariant at the initial state is large, (ii) the SIDF of H935 is stronger than that of B920 even though the invariant at the initial state is small. These facts indicate that the stress fields changed during stretching. The destruction of the crystalline structures associating with strain might induce the homogenization of the stress field and cause the suppression of the SIDF. The decrease in the crystallinity with strain, or mechanical melting was first proposed by Flory and Yoon.[22] Since then, mechanical melting behavior has been discussed not only in polyethylene but also in other polymers.[23-25] I investigated the behaviors of mechanical melting during stretching to clarify whether the homogenization occurs with the destruction.

5.3.7 Mechanical Melting during Stretching

To quantitatively analyze the mechanical melting behavior, I calculated the changes in the crystallinity with strain from WAXS data. The crystallinity of LLDPE during uniaxial stretching ($W_{\mathrm{c,uni}}$) is given by

$$W_{\mathrm{c,uni}}(\lambda) = \frac{W_{\mathrm{c},110}(\lambda)+W_{\mathrm{c},200}(\lambda)}{W_{\mathrm{c},110}(\lambda)+W_{\mathrm{c},200}(\lambda)+W_{\mathrm{a}}(\lambda)} \tag{5.9}$$

where $W_{c,110,}$ and $W_{c,200}$ characterize the weight of the crystalline lattice structure estimated from $(110)_{ortho}$ and $(200)_{ortho}$ reflection, respectively, and W_a characterizes the weight of the amorphous region. To obtain these terms, I calculated sector averages at every 5˚ in the μ range from 90˚ to 180˚ from the WAXS patterns and fitted them to a linear combination of three Gaussian functions and a constant (background). The three Gaussian functions correspond to the amorphous halo, $(110)_{otho}$ reflection, and $(200)_{ortho}$ reflection, respectively. Similar to the calculation of $Q_{U,uni}$, assuming that the scattering intensity distribution is symmetrical along the q_z-axis, the weight of the lattice structure estimated from (hkl) reflection ($W_{c,hkl}$) and W_a are defined as

$$W_{c,hkl}(\lambda) = -4\pi \int_{\frac{\pi}{2}}^{\pi} q_{hkl}(\lambda,\mu) I_{hkl}(\lambda,\mu) w_{hkl}(\lambda,\mu) \cos\mu \, d\mu \tag{5.10}$$

$$W_a(\lambda) = -4\pi \int_{\frac{\pi}{2}}^{\pi} q_a(\lambda,\mu) I_a(\lambda,\mu) w_a(\lambda,\mu) \cos\mu \, d\mu \tag{5.11}$$

where q_{hkl}, I_{hkl}, and w_{hkl} are, respectively, the position, intensity, and width of the peak from (hkl) reflection on the profiles, and q_a, I_a, and w_a are the position, intensity, and width of the amorphous halo.

Figure 5.24 shows the reduced crystallinity $W_{c,uni}(\lambda)/W_{c,uni}(1)$ plotted as a function of strain. $W_{c,uni}(\lambda)/W_{c,uni}(1)$ of H920 started decreasing after the onset of stretching, reflecting that mechanical melting started immediately by the application of strain. Mechanical melting reduced the fluctuations of the stress fields in the sample so that the SIDF did not occur in H920. On the other hand, the crystallinity of B935 became

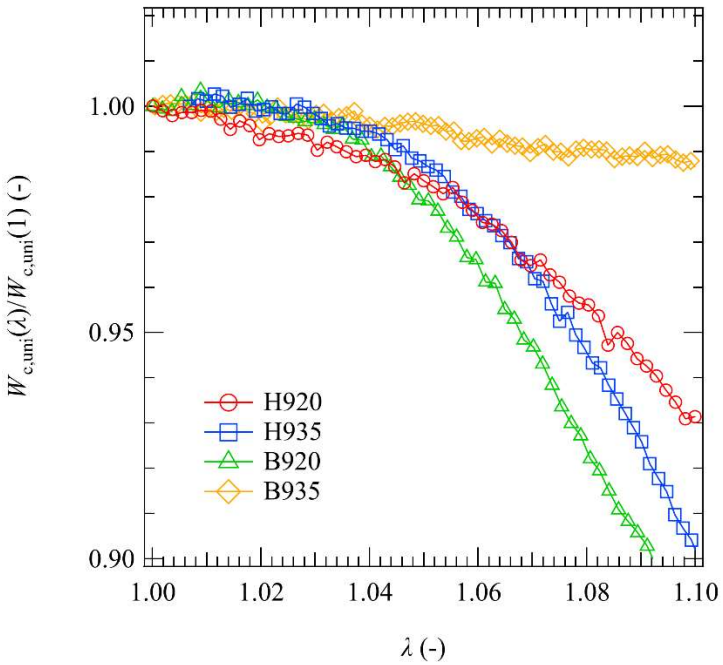

Figure 5.24 λ dependence of $W_{c,uni}(\lambda)/W_{c,uni}(1)$ of all samples.

constant with strain and the lamellar structures did not change with strain at $\lambda < 1.1$ as shown in Figure 5.17(a). These results indicate that the increase in USAXS intensity was caused by the formation of the void originating from the defect.

In the case of H935 and B920, the crystallinity becomes almost constant in the early stage of the stretching process or $\lambda < 1.05$. The SIDF occurred because the relaxation of the stress field was not induced by mechanical melting. However, in the later stage or $\lambda > 1.05$, mechanical melting occurred in both H935 and B920. The decrease in the crystallinity of B920 is more pronounced than that of H935. Thus, the SIDF in H935 was stronger than that in B920. These melting behaviors depended on the species and contents of the comonomer. The bulky comonomer and the large comonomer content induce melting during stretching.

5.4 Conclusion

To clarify the factors governing the SIDF in crystalline materials, I have investigated the changes in the submicron structures of LLDPE with different comonomer species and contents during uniaxial stretching by time-resolved USAXS as well as changes in the lamellar structures and lattice structures by time-resolved SAXS and WAXS.

The changes in the hierarchical structures in all samples were classified into the following three cases. (i) The case in which the sample had the homogeneous structure on the submicron scale before stretching (i.e. B935), (ii) the case in which the sample had the inhomogeneous submicron structure at the initial state but the crystalline structure melted with strain at the early stage of stretching (i.e. H920), and (iii) the case in which the sample had the inhomogeneous submicron structure at the initial state and mechanical melting started at the later stage of stretching (i.e. H935 and B920). In the cases of (i) and (ii), the butterfly pattern, which characterizes the occurrence of the SIDF was not observed. In the case of (iii), The sample exhibited the butterfly pattern and the intensity was governed by the degree of mechanical melting. The degree of mechanical melting depends on the species and contents of the comonomer. On the other hand, the inhomogeneity of the submicron structure at the initial state would depend not only on the comonomer characteristics but also on the crystallization condition.

References

1. Kishimoto, M.; Mita, K.; Ogawa, H.; Takenaka, M., *Macromolecules* **2020,** *53*, 9097-9107.
2. Bastide, J.; Leibler, L.; Prost, J., *Macromolecules* **1990,** *23*, 1821-1825.
3. Mendes, E.; Oeser, R.; Hayes, C.; Boué, F.; Bastide, J., *Macromolecules* **1996,** *29*, 5574-5584.
4. Kume, T.; Hattori, T.; Hashimoto, T., *Macromolecules* **1997,** *30*, 427-434.
5. Kume, T.; Hashimoto, T.; Takahashi, T.; Fuller, G. G., *Macromolecules* **1997,** *30*, 7232-7236.
6. Moses, E.; Kume, T.; Hashimoto, T., *Phys. Rev. Lett.* **1994,** *72*, 2037-2040.
7. Hashimoto, T.; Kume, T., *J. Phys. Soc. Jpn.* **1992,** *61*, 1839-1843.
8. Doi, M.; Onuki, A., *J. Phys. II* **1992,** *2*, 1631-1656.
9. Furukawa, A.; Tanaka, H., *Nat. Mater.* **2009,** *8*, 601-609.
10. Shirayama, K.; Kita, S. I.; Watabe, H., *Makromol. Chem.* **1972,** *151*, 97-120.
11. Simanke, A. G.; Alamo, R. G.; Galland, G. B.; Mauler, R. S., *Macromolecules* **2001,** *34*, 6959-6971.
12. De Pooter, M.; Smith, P. B.; Dohrer, K. K.; Bennett, K. F.; Meadows, M. D.; Smith, C. G.; Schouwenaars, H. P.; Geerards, R. A., *J. Appl. Polym. Sci.* **1991,** *42*, 399-408.
13. Brandrup, J.; Immergut, E. H.; Grulke, E. A.; Abe, A.; Bloch, D. R., *Polym. handbook*. Wiley New York: 1999; Vol. 89.
14. Masunaga, H.; Ogawa, H.; Takano, T.; Sasaki, S.; Goto, S.; Tanaka, T.; Seike, T.; Takahashi, S.; Takeshita, K.; Nariyama, N.; Ohashi, H.; Ohata, T.; Furukawa, Y.; Matsushita, T.; Ishizawa, Y.; Yagi, N.; Takata, M.; Kitamura, H.; Sakurai, K.;

Tashiro, K.; Takahara, A.; Amamiya, Y.; Horie, K.; Takenaka, M.; Kanaya, T.; Jinnai, H.; Okuda, H.; Akiba, I.; Takahashi, I.; Yamamoto, K.; Hikosaka, M.; Sakurai, S.; Shinohara, Y.; Okada, A.; Sugihara, Y., *Polym. J.* **2011,** *43*, 471-477.

15. Kishimoto, M.; Mita, K.; Jang, J.; Takahashi, N.; Ogawa, H.; Nishida, K.; Kanaya, T.; Takenaka, M., *Polym. J.* **2019,** *51*, 173-182.
16. Debye, P.; Bueche, A. M., *J. Appl. Phys.* **1949,** *20*, 518-525.
17. Takenaka, M.; Shimizu, H.; Nishitsuji, S., *Phys. Rev. E* **2007,** *75*, 061802.
18. Strobl, G., The Physics of Polymers. *Springer-Verlag Berlin Heidelberg* **2007**.
19. Shinohara, Y.; Kishimoto, H.; Inoue, K.; Suzuki, Y.; Takeuchi, A.; Uesugi, K.; Yagi, N.; Muraoka, K.; Mizogichi, T.; Amemiya, Y., *J. Appl. Crystallogr.* **2007,** *40*, 397-401.
20. Takenaka, M., *Polym. J.* **2013,** *45*, 10-19.
21. Hashimoto, T.; Amino, N.; Nishitsuji, S.; Takenaka, M., *Polym. J.* **2019,** *51*, 109-130.
22. Flory, P. J.; Yoon, D. Y., *Nature* **1978,** *27*, 226-229.
23. Lucas, J. C.; Failla, M. D.; Smith, F. L.; Mandelkern, L.; Peacock, A. J., *Polym. Eng. & Sci.* **1995,** *35*, 1117-1123.
24. Butler, M. F.; Donald, A. M.; Ryan, A. J., *Polymer* **1997,** *38*, 5521-5538.
25. De Rosa, C.; Auriemma, F.; Ruiz de Ballesteros, O.; Resconi, L.; Camurati, I., *Chem. Mater.* **2007,** *19*, 5122-5130.

Chapter 6
Spatial Inhomogeneity of Chain Orientation Associated with the Strain-Induced Density Fluctuations in PE

6.1 Introduction

Polyethylene (PE) is one of the most widely used polymer materials in daily life due to its excellent mechanical properties and formability. PE is a crystalline polymer and forms a hierarchical structure, as shown in Figure 1.1. Its hierarchical structure includes a crystalline lattice structure in which molecular chains are regularly folded, a lamellar structure in which the crystalline and amorphous phases are alternately stacked, a fibril structure formed by the growing lamellar structure, and a spherulitic structure formed by the filling of the fibril structure. Many studies have been carried out to clarify the correlation between the hierarchical structure and physical properties of PE.[1-4] In Chapter 4[5], I showed that the structure on the submicron scale has a significant effect on mechanical properties during uniaxial tensile testing by observing the submicron-scale structure with ultra-small-angle X-ray scattering (USAXS), of which the q-range is 0.008 to 0.06 nm^{-1}. Here, q is the magnitude of the scattering vector. I observed the appearance of a butterfly pattern in USAXS at the stress overshoot in the stress-strain curve during uniaxial tensile testing. The butterfly pattern reflects the development of density fluctuations induced by strain. The enhancement of the scattered intensity along the strain

direction indicates that a strong correlation in density fluctuations appears along the stretching direction. The characteristic length of the density fluctuations along the stretching direction is on the order of 100 nm. Induction by strain occurs in dynamically asymmetric systems where the spatial inhomogeneity of the stress field or spatial inhomogeneity of the modulus is associated with density fluctuations[6-7]. In the case of PE used here, the modulus or stress field varies with the density fluctuations associated with the spatial distribution of crystallinity. Doi and Onuki and Furukawa and Tanaka[6,7] theoretically proved that the gradient of the stress field induces the enhancement of the density fluctuations under deformation. The induction of density or concentration fluctuations has been reported in semi-dilute solutions of polymers under simple shear, gels under uniaxial elongational deformation, and metallic glasses.[7-10] Further tensile testing causes the transformation of lower-density regions into voids during uniaxial tensile testing in PE.

The orientation of polymer chains is also affected by the strain as well as the density fluctuations. Small-angle X-ray scattering (SAXS) and wide-angle X-ray diffraction (WAXS) are useful to evaluate the orientation change of lamellar structures and crystal lattice structures, respectively. However, these methods provide only average information within the irradiated volume, which depends on the incident X-ray beam size (typically μm to mm) and sample thickness, so the orientation fluctuations on the submicron scale cannot be investigated. To observe the orientation of polymer chains, I employed scanning transmission X-ray microscopy (STXM). By using STXM, near-edge X-ray absorption fine structure (NEXAFS) spectra with a spatial resolution of 20–100 nm can be obtained.[11-13] NEXAFS data of C–C and C–H bonds vary with the angles of C–C and C–H bonds and the polarized direction of X-rays. The difference between the

NEXAFS data observed with horizontally and vertically polarized X-rays or the anisotropy of the NEXAFS data is induced by the anisotropic distribution of C–C and C–H bonds. Since the spatial resolution of STXM is typically 20–100 nm, the anisotropy of the NEXAFS data in the STXM experiment originates not only from the orientation of the fine structure or crystalline phase but also from the orientation of lamellar stacks. In the amorphous phase, the aligned chains affect the anisotropy of the NEXAFS data. All the abovementioned anisotropic factors accompany the anisotropy of the chain orientation. Thus, the anisotropy of the NEXAFS data of STXM reflects the chain orientation on the submicron scale. In this chapter, I observed the anisotropy of the chain orientation as well as density fluctuations on the submicron scale in stretched PE by using STXM and clarified how the anisotropy is developed by strain.

6.2 Experimental Section

6.2.1 Sample Preparation

I used high-density polyethylene (HDPE) with a polystyrene-equivalent M_w of 2.3×10^5 and M_w/M_n of 11.9, as determined by gel permeation chromatography (GPC). The molding conditions were as follows: Two presses (manufactured by Toyo Seiki) were used. One press was set at 180 °C, which is above the melting point of PE, and the PE was pressed for 10 minutes in a 2-mm-thick mold for melting and then transferred to the other press machine set at 25 °C for cooling. Although transfer took 5 sec, the temperature of the sample was kept above the crystallization temperature. A dumbbell specimen with a center width of 2 mm was punched from the resulting press sheet. The specimen was stretched at 15 mm/min up to an elongation ratio L/L_0 = 1.09 at room temperature by using a homemade tensile testing machine and studied the specimen with X-ray scattering.

Here, L_0 and L are the lengths of the sample before and after applying strain, respectively. For the STXM measurement, ultrathin sections with a thickness of approximately 100 nm were prepared from the specimen using a Leica EM UC7 microtome. The sample was cut in the stretching direction.

6.2.2 USAXS, SAXS, and WAXS Measurements

USAXS measurements were carried out at BL03XU in SPring-8.[14] The USAXS data were obtained using PILATUS 1M (DECTRIS) with 981 × 1043 pixels of 172 × 172 μm (horizontal × vertical) pixel size. The camera length was 7.9 m. The exposure time was set to 900 msec. The wavelength of incident X-rays was 0.2 nm. The X-ray beam size at the sample position (horizontal × vertical) was 200 μm × 100 μm. X-rays were incident perpendicular to the stretching direction, and the two-dimensional (2D) scattering patterns were detected. The obtained 2D data were corrected for the absorption of the sample, subtracted air and background scattering.

Simultaneous SAXS/WAXS measurements were also performed at BL03XU. The incident X-ray wavelength was 0.08 nm. The camera length, exposure time and detectors were set to 2.4 m/120 mm, 670 msec/570 msec and PILATUS/SOPHIAS for SAXS/WAXS, respectively. The X-ray beam size at the sample position was the same as that in the USAXS measurement. X-rays were incident perpendicular to the sample, and scattered X-rays on the backside were detected. The WAXS detector was placed diagonally to avoid interfering with the SAXS detector[14]. The obtained 2D data were corrected in the same way as they were for USAXS.

6.2.3 STXM Observations

STXM measurements were performed at BL-19A at the Photon Factory of the High Energy Accelerator Research Organization (KEK-PF: Tsukuba, Japan). X-rays were incident perpendicular to the surface of the ultrathin section. The incident X-ray energy range used here was 280–320 eV, which is the near the absorption energy of the carbon *K*-edge (~284 eV). The exposure time was 2 msec. The polarization (electric field) direction of the X-rays parallel and perpendicular to the stretching direction was able to be set without rotating the samples. Thus, I was able to observe the same area of the sample under different polarizations. A 2D map of the following optical density (OD) or NEXAFS spectra can be obtained at a given X-ray energy with a 50 nm resolution:[15]

$$\mathrm{OD} = -\ln(I/I_0) \tag{6.1}$$

where I and I_0 denote the transmitted X-ray intensity and incident X-ray intensity, respectively.

6.3 Results and Discussion

6.3.1 X-ray Scattering

Figure 6.1 shows the USAXS/SAXS/WAXS patterns at $L/L_0 = 1.09$. The patterns at $L/L_0 = 1.09$ became anisotropic. Note that USAXS/SAXS/WAXS patterns before the application of strain were isotropic, and detailed analyses of the patterns are also shown in Chapter 4.[5] In the USAXS pattern (Figure 6.1(a)), a butterfly pattern was observed, and the intensity was enhanced in the direction parallel to stretching. As mentioned in

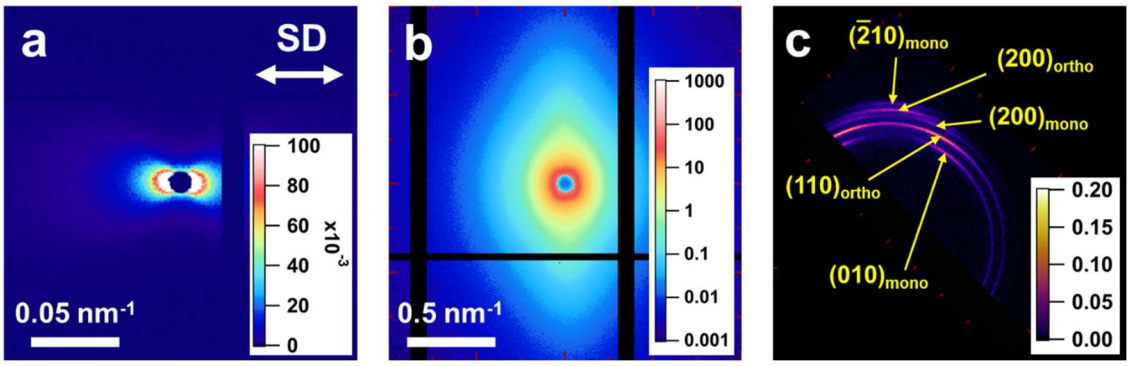

Figure 6.1 (a) USAXS, (b) SAXS and (c) WAXS patterns of HDPE at L/L_0=1.09. The arrow in part (a) corresponds to the stretching direction.

Chapter 4,[5] coupling between the stress field and density fluctuations induced the development of density fluctuations on the submicron scale. The SAXS pattern at L/L_0 = 1.09 shows strong scattering elongated in the direction perpendicular to the stretching direction (Figure 6.1(b)), suggesting that the structures on the order of 10 nm were elongated in the stretching direction. A clear peak that reflects the periodicity of the lamellar structures was not observed. The SAXS pattern at L/L_0 = 1.09 suggests that stretching reduced the periodicity of the lamellar structures and that fragmentation of lamellar structures occurred. In the WAXS pattern (Figure 6.1(c)), the diffraction peak of the (110) plane of the orthorhombic crystal ($(110)_{ortho}$ peak) was split in the directions tilted approximately ±30° from the meridian direction.[5]

The split reflections indicate a chevron-type morphology from the fragmentation and rotation of the lamellar structure by coarse slip.[5] In addition, the peak of the (010) plane of the monoclinic crystal ($(010)_{mono}$ peak), which was not observed before stretching, appeared in the same orientation as the split orthorhombic (110) peaks. Monoclinic transitions occur in orthorhombic (110) crystals due to cooperative shifting of molecular chains.[16] The degrees of crystallinity were determined to be 72% and 58%

for L/L_0 = 1.00 and 1.09, respectively, indicating that so-called mechanical melting occurs in association with stretching, as already discussed.[5,17,18] Lamellar fragmentation and subsequent mechanical melting would cause a decrease in the periodicity of the lamellar structure observed by SAXS. Note that the crystallinity at L/L_0 = 1.09 reflects the sum of the monoclinic and orthorhombic components.

6.3.2 STXM Observations

Figure 6.2 shows the NEXAFS spectrum (OD) of the entire field of view of the STXM image obtained for the stretched HDPE specimen. The characteristic peaks of the C–H bond (C 1s→σ^*_{C-H}) and C–C bond (C 1s→σ^*_{C-C}) were observed at 287.5±0.2 and 292±1 eV, respectively, near the carbon *K*-edge, as indicated by the arrows in Figure 6.2, agreeing with the previous result.[19-21] On the other hand, a plateau region was observed above 315 eV. It is well known that the plateau region far from the carbon *K*-edge is not affected by the orientation of chemical bonds but depends on the density of carbon and the sample thickness.[19] Thus, considering that the sample thickness is constant in the observed region, the 2D map of OD (OD image) above 315 eV reflects the density fluctuations.

First, I investigated the existence of density fluctuations in the specimen. Figure 6.3 shows the OD image at 318±2 eV obtained with horizontally polarized X-rays. SD and PD in Figure 6.3 denote the stretching direction and the polarization direction of the incident X-rays, respectively. The image at 318±2 eV obtained with vertical polarization was almost identical to that shown in Figure 6.3. The peak at 318±2 eV in Figure 6.3 shows spatial inhomogeneity, indicating that the density fluctuations were induced by strain. This result agrees with USAXS observation.

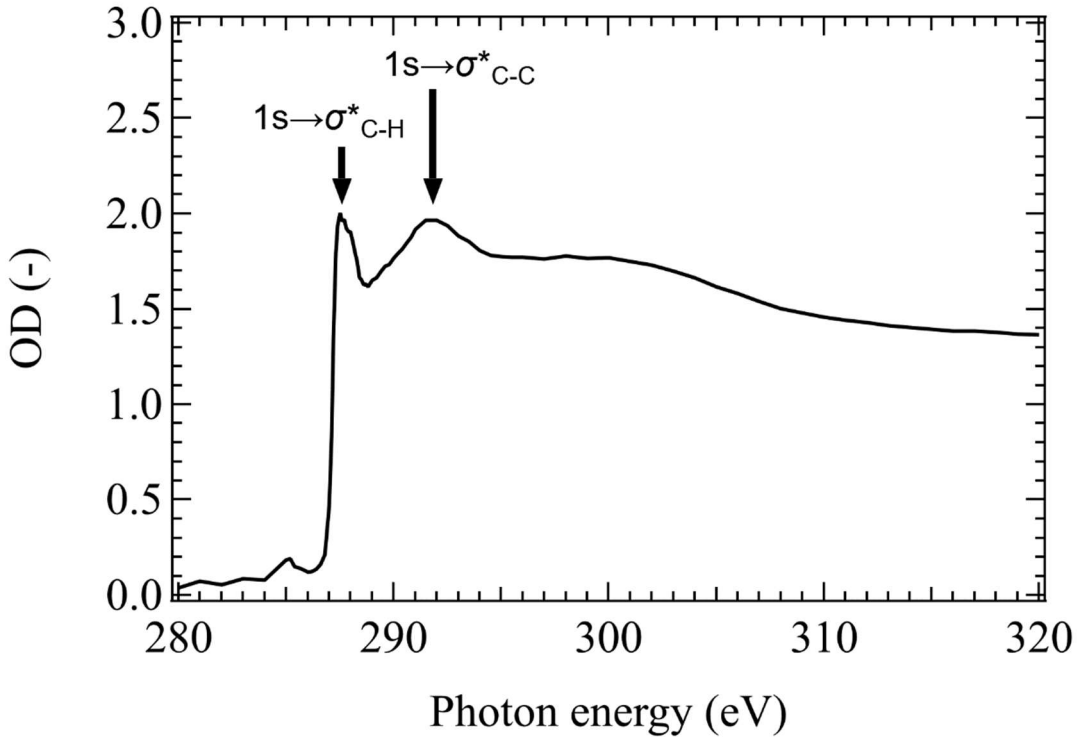

Figure 6.2 NEXAFS spectrum of HDPE at L/L_0=1.09. The optical density (OD) was obtained by averaging the spectra in the observed STXM image.

Next, I discuss the orientation fluctuations observed from the OD images at the peaks of C–C and C–H bonds. Wang et al. used STXM to reveal the orientation fluctuations of the fibril structure in linear low-density PE (LLDPE) spherulites.[19] They observed an as-spun thin film of LLDPE, and the fibril structure after deformation has not yet been investigated. Figures 6.4 and 6.5 show the effects of the polarization of incident X-ray on the OD images at 287.5±0.2 eV (C 1s→$\sigma^*_{C–H}$) and 292±1 eV (C 1s→$\sigma^*_{C–C}$), respectively. The figures show changes in the spatial distribution of OD with polarization for both incident X-ray energies, indicating the spatial inhomogeneity of the chain orientation in the samples.

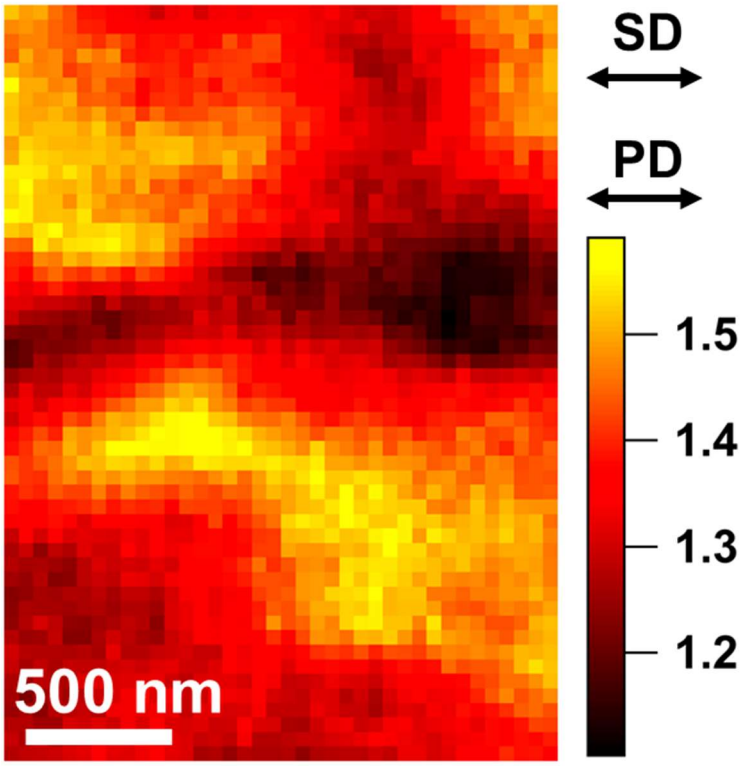

Figure 6.3 OD image of HDPE at 318±2 eV. The polarization direction (PD) of the incident X-rays was set to be parallel to the stretching direction (SD).

Figures 6.4 and 6.5 depend not only on the density but also on the chain orientation, while Figure 6.3 depends only on the density. To quantitatively discuss the orientation fluctuation, I extracted the information of the chain orientation by calculating the following orientational order parameter of a pixel $\langle P_2 \rangle$:[22]

$$\langle P_2 \rangle = \frac{3\langle \cos^2 \theta_A \rangle - 1}{2} \tag{6.2}$$

where θ_A denotes the angle between the transition dipole moment (TDM) $\boldsymbol{\mu}_{\mathrm{if}}$ of C–C bonds and the stretching direction. $\langle \cos^2 \theta_A \rangle$ is the average of $\cos^2 \theta_A$ in a pixel. $\langle P_2 \rangle$ is expressed by

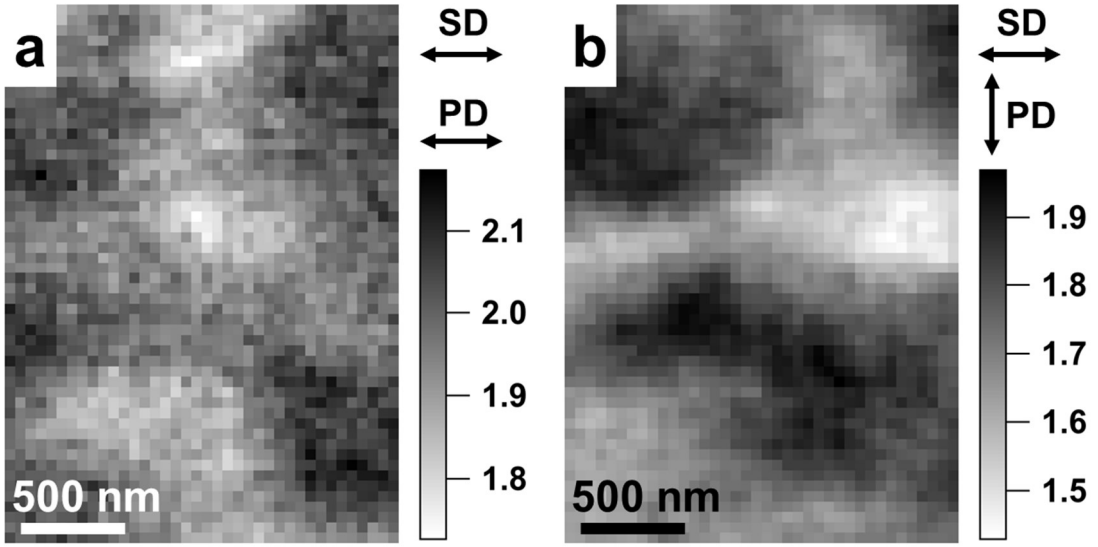

Figure 6.4 OD images of HDPE at 287.5±0.2 eV corresponding to the peak of the C–H bond. The polarization direction (PD) of the incident X-rays was set to be (a) parallel and (b) perpendicular to the stretching direction (MD).

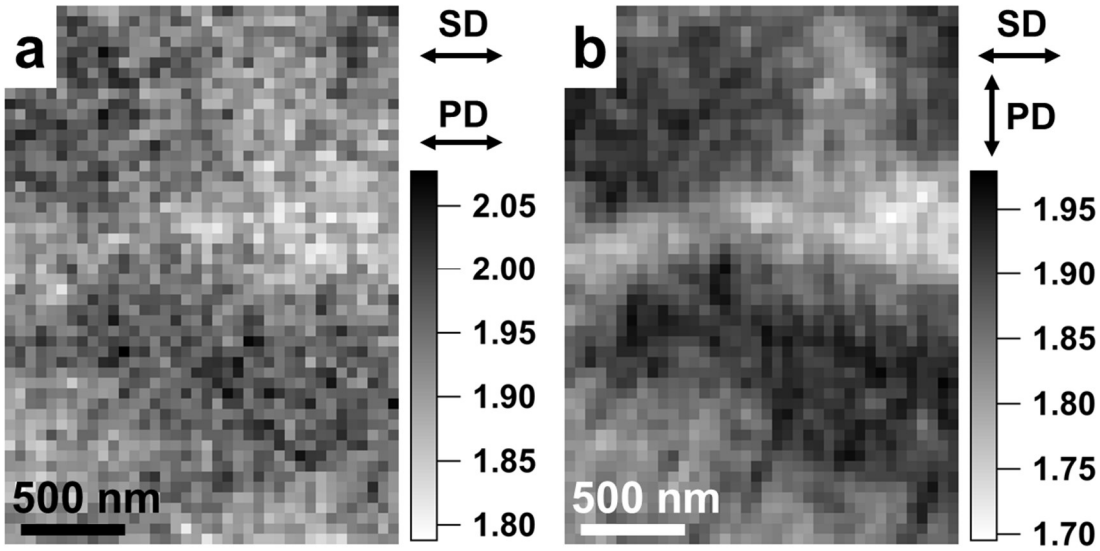

Figure 6.5 The OD image for HDPE at 292±1 eV corresponding to the peak of the C–C bond. The polarization direction (PD) of the incident X-rays was set to be (a) parallel and (b) perpendicular to the stretching direction (SD).

$$\langle P_2 \rangle = \frac{A_{||} - A_{\perp}}{A_{||} + 2A_{\perp}} \tag{6.3}$$

where $A_{||}$ and $A_{\perp}$ are the absorbance A obtained at 292±1 eV under condition where the electric field vector **E** is parallel and perpendicular to the stretching direction, respectively. The absorbance A is the OD originating from TDM and is proportional to the inner product of **E** and $\boldsymbol{\mu}_{\mathrm{if}}$:

$$A \propto |\mathbf{E} \cdot \boldsymbol{\mu}_{\mathrm{if}}|^2 \propto \cos^2 \alpha_A \tag{6.4}$$

where α_A is the angle between **E** and $\boldsymbol{\mu}_{\mathrm{if}}$. A is obtained by subtracting the background of the edge jump from the NEXAFS spectra.[23] The value of $\langle P_2 \rangle$ is 1 for perfect parallel alignment of the C–C bonds in the stretching direction, while the value is −0.5 for perfect perpendicular alignment. The $\langle P_2 \rangle$ images were calculated from Figures 6.5(a) and (b) and are shown in Figure 6.6. Comparing Figure 6.6 with Figure 6.3, I concluded that the spatial inhomogeneity of the chain orientation is correlated with density fluctuations. The chain orientation in the low-density region is stronger than that in the high-density region.

To investigate the density dependence of the chain orientation, I plotted OD as a function of energy in low-density and high-density regions in Figure 6.7. I defined high-density and low-density regions as the regions at $\mathrm{OD}_d > \overline{\mathrm{OD}_d} + 1.5\sigma$ and $\mathrm{OD}_d < \overline{\mathrm{OD}_d} - 1.5\sigma$, respectively. Here, OD_d, $\overline{\mathrm{OD}_d}$, and σ are the OD at 318±2 eV (Figure 6.3), the spatially averaged OD_d and the standard deviation of OD_d. In the figure, || and ⊥ denote the condition where the polarization of X-rays is parallel and perpendicular to the stretching direction, respectively. Ohta et al.,[20] and Stöhr et al.[21] found a polarization dependence in the NEXAFS spectra of PE: the intensities of the C–C bond (C 1s→σ*$_{C-}$

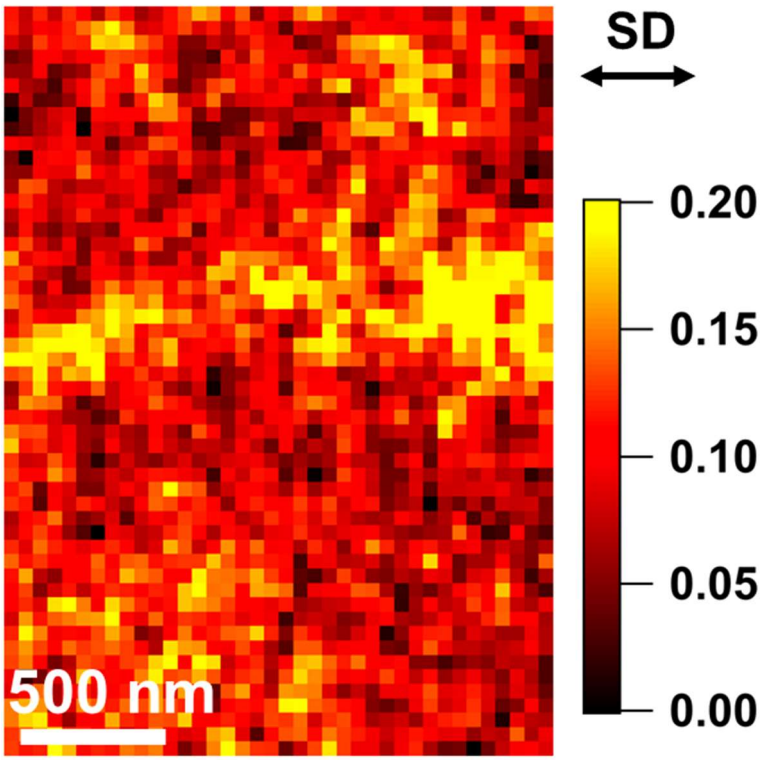

Figure 6.6 $\langle P_2 \rangle$ image of HDPE at 292±1 eV. The arrow in the figures corresponds to the stretching direction.

$_C$) and C–H bond (C 1s→σ*$_{C–H}$) reach their maximum and minimum values, respectively, when the polarization of X-rays is parallel to the orientation direction of PE. On the other hand, when the polarization of X-rays is perpendicular to the orientation direction of PE, the opposite results are obtained.

In the case of the high-density region, as shown in Figure 6.7(a), the intensity of the C–C bond under the || condition is slightly higher than that under the ⊥ condition. In the high-density region, the anisotropy of OD is dominated by crystalline structures. As shown by WAXS, stretching induced chevron structures, where the *c*-axis tilted approximately ±30° from the stretching direction. The asymmetric tilt induced the anisotropy of the OD. However, the intensity of the C–H bond under the || condition is

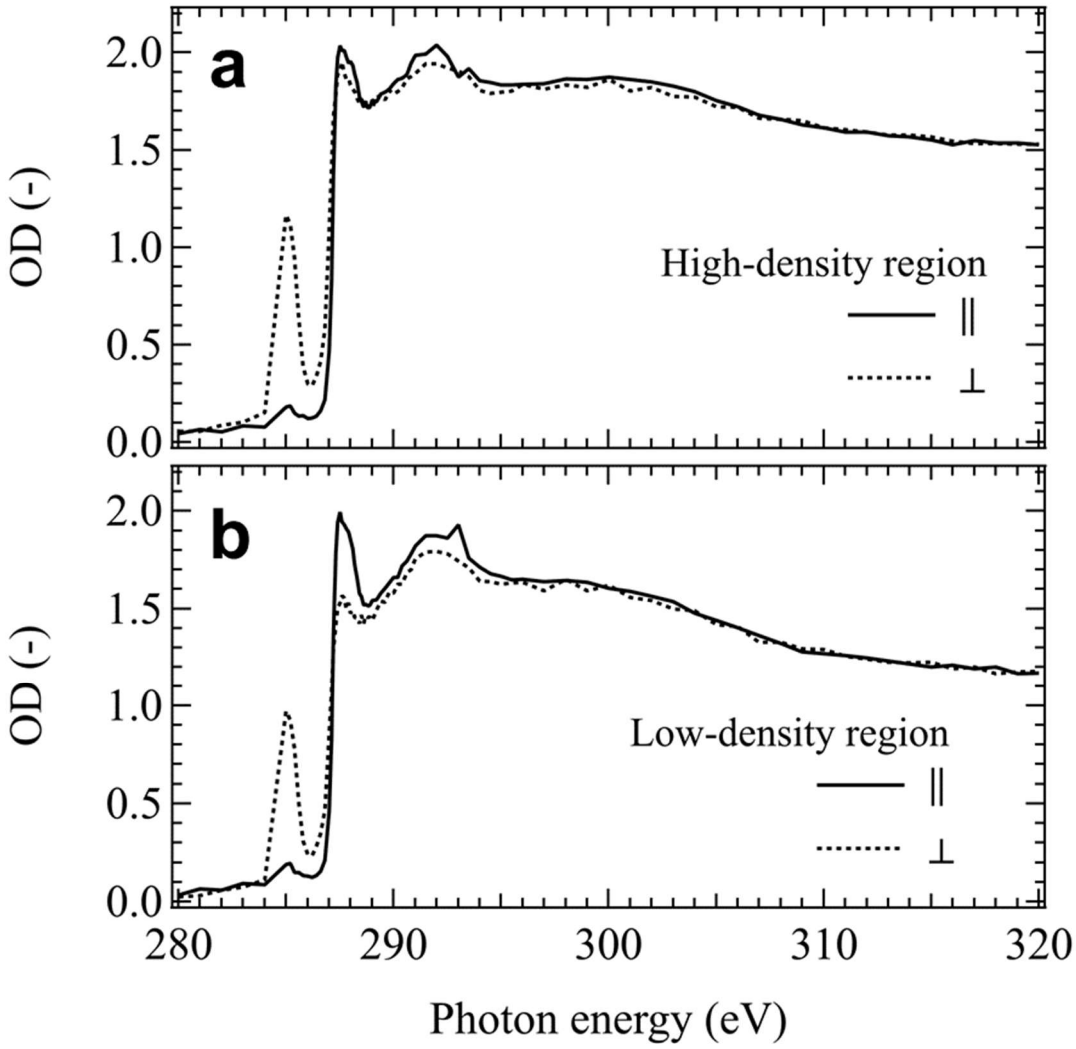

Figure 6.7 NEXAFS spectra of the (a) high-density region and (b) low-density region. || and ⊥ denote the condition where the polarization of X-rays is parallel and perpendicular, respectively, to the stretching direction.

slightly higher than that under the ⊥ condition. The direction of the C–H bond is perpendicular to the direction of the C–C bond, so the intensity of the C–H bond under the || condition should be lower than that under the ⊥ condition. This tendency originates from the fact that the mechanical melting of the lamellar structures occurred in association with stretching. In the melting state under stretching, the chain is oriented, but the direction of the C–H bond becomes random, reducing the intensity of the C–H bond under the ⊥ condition.

In the case of the low-density region, the intensity of the C–C bond of the || condition is also higher than that of the ⊥ condition. A distinct peak appeared at 293 eV, reflecting the high chain orientation[21] in the intensity of the C–C bond of the || condition, and the anisotropy in the low-density region was stronger than that in the high-density region, while the amount of the crystalline phase in the low-density region was smaller than that in the high-density region. This is because the strain induces a strong orientation in the crystalline phase. The *c*-axis may be aligned in the stretching direction. The peak at 293 eV shows that the PE chains are oriented parallel to the stretching direction. The stronger orientation in the low-density region suggests that inhomogeneous deformation occurs under stretching. A strong reduction was found in the intensity of the C–H bond under the ⊥ condition. This reduction results in mechanical melting. The amount of amorphous regions in the low-density region is larger than that in the high-density region, so a strong reduction was observed in the low-density region.

6.3.4 Conclusion

I used STXM as well as USAXS, SAXS, and WAXS to investigate the spatial inhomogeneity of the chain orientation in HDPE associated with the strain-induced density fluctuations on the submicron scale. At the strain where the butterfly pattern was observed in USAXS, I used STXM to obtain a real-space image of the strain-induced density fluctuations. STXM also showed that the chain orientation in the stretching direction in the low-density region is stronger than that in the high-density region. This originates from the stronger alignment of the crystalline phase in the low-density region. This result indicates that strain induces not only density fluctuations but also the spatial inhomogeneity of the chain orientation.

References

1. Wilchinsky, Z. W., *Polymer* **1964,** *5*, 271–281.
2. Fu, Q.; Men, Y.; Strobl, G., *Polymer* **2003,** *44*, 1941-1947.
3. Che, J.; Locker, C. R.; Lee, S.; Rutledge, G. C.; Hsiao, B. S.; Tsou, A. H., *Macromolecules* **2013,** *46*, 5279-5289.
4. Strobl, G. R.; Hagedorn, W., *J. Polym. Sci.: Polym. Phys. Ed.* **1978,** *16*, 1181-1193.
5. Kishimoto, M.; Mita, K.; Ogawa, H.; Takenaka, M., *Macromolecules* **2020,** *53*, 9097-9107.
6. Doi, M.; Onuki, A., *J. Phys. II* **1992,** *2*, 1631–1656.
7. Furukawa, A.; Tanaka, H., *Nat. Mater.* **2009,** *8*, 601–609.
8. Hashimoto, T.; Kume, T., *J. Phys. Soc. Jpn.* **1992,** *61*, 1839-1843.
9. Bastide, J.; Leibler, L.; Prost, J., *Macromolecules* **1990,** *23*, 1821-1825.
10. Mendes, E.; Oeser, R.; Hayes, C.; Boué, F.; Bastide, J., *Macromolecules* **1996,** *29*, 5574–5584.
11. Kilcoyne, A. L.; Tyliszczak, T.; Steele, W. F.; Fakra, S.; Hitchcock, P.; Franck, K.; Anderson, E.; Harteneck, B.; Rightor, E. G.; Mitchell, G. E.; Hitchcock, A. P.; Yang, L.; Warwick, T.; Ade, H., *J. Synchrotron Rad.* **2003,** *10*, 125–136.
12. Takeichi, Y.; Inami, N.; Suga, H.; Ono, K.; Takahashi, Y., *Chem. Lett.* **2014,** *43*, 373–375.
13. Ohigashi, T.; Arai, H.; Araki, T.; Kondo, N.; Shigemasa, E.; Ito, A.; Kosugi, N.; Katoh, M., *J. Phys.: Conf. Ser.* **2013,** *463*, 012006.
14. Masunaga, H.; Ogawa, H.; Takano, T.; Sasaki, S.; Goto, S.; Tanaka, T.; Seike, T.; Takahashi, S.; Takeshita, K.; Nariyama, N.; Ohashi, H.; Ohata, T.; Furukawa, Y.;

Matsushita, T.; Ishizawa, Y.; Yagi, N.; Takata, M.; Kitamura, H.; Sakurai, K.; Tashiro, K.; Takahara, A.; Amamiya, Y.; Horie, K.; Takenaka, M.; Kanaya, T.; Jinnai, H.; Okuda, H.; Akiba, I.; Takahashi, I.; Yamamoto, K.; Hikosaka, M.; Sakurai, S.; Shinohara, Y.; Okada, A.; Sugihara, Y., *Polym. J.* **2011,** *43*, 471-477.

15. Fu, J.; Urquhart, S. G., *Langmuir* **2007,** *2*, 2615–2622.

16. Takahashi, Y.; Ishida, T.; Furusaka, M., *J. Polym. Sci. Part B: Polym. Phys.* **1988,** *26*, 2267-2277.

17. Flory, P. J.; Yoon, D. Y., *Nature* **1978,** *272*, 226-229.

18. Lucas, J. C.; Failla, M. D.; Smith, F. L.; Mandelkern, L.; Peacock, A. J., *Polym. Eng. Sci.* **1995,** *35*, 1117–1123.

19. Wang, Y.; Zou, Y.; Araki, T.; Lüning, J.; Kilcoyne, A. L. D.; Sokolov, J.; Ade, H.; Rafailovich, M., *Macromolecules* **2010,** *43*, 8153–8161.

20. Ohta, T.; Seki, K.; Yokoyama, T.; Morisada, I.; Edamatsu, K., *Physica Scripta* **1990,** *41*, 150-153.

21. Stöhr, J., *NEXAFS spectroscopy*. Springer Science & Business Media: 1992; Vol. 25.

22. Hernández Cruz, D.; Rousseau, M.-E.; West, M. M.; Pézolet, M.; Hitchcock, A. P., *Biomacromolecules* **2006,** *7*, 836-843.

23. Fu, J.; Urquhart, S. G., *J Phys. Chem. A* **2005,** *109*, 11724-11732.

Summary

This thesis includes the studies on the role of stress field in the formation and destruction processes of the hierarchical structures in crystalline polyolefins. I summarize each chapter as follows.

In Chapter 1, I described the background, the motivation, and the outline of this thesis.

In Chapter 2, in order to elucidate the role of stress field in the crystallization process, I performed in-situ observations of P3MB1 during the isothermal crystallization using OM and X-ray scattering techniques. In addition, thermodynamic parameters such as T_m^0, ΔH, and σ_e of P3MB1 were first collected and compared with those of PE. As the degree of supercooling in P3MB1 decreased, the number of lamellar branches decreased, and eventually the morphology transition (spherulites → axialites → needle-like crystals) occurred. Because P3MB1 has much higher T_m than PE, the viscosity of the melt during crystallization of P3MB1 is much lower than that of PE. This is the leading factor that induced the morphology transition.

In Chapter 3, in order to reveal the spatial inhomogeneity of dynamics in the amorphous region after crystallization, I applied CV-SAS under solvent swelling to the EOC. Conventional CV-SANS with deuterium substitution has difficulty in separating the scattering functions of the crystalline and amorphous regions. Therefore, I showed that Et-toluene and Br-xylene have equivalent interactions (χ parameters) against the EOC, respectively, and performed CV-SAXS with the mixture of these solvents. I found the presence of the amorphous layers surrounding the crystallites, which are not swollen by the solvents, and the network structure of the crystallites via the non-swollen amorphous

layers. The volume fractions of the crystallites, the rigid amorphous regions, and the melt-like region estimated from CV-SAXS agreed with those obtained from pulsed ^{1}H-NMR. These results indicate that the rigid amorphous regions exist surrounding the crystallites.

In Chapter 4, I investigated how the stress field under deformation affects the changes in the hierarchical structures and mechanical properties of PE. I performed in-situ USAXS, SAXS, and WAXS measurements on HDPE and LLDPE under tensile testing. In the case of the HDPE, the butterfly pattern was observed in USAXS, which characterizes dynamic coupling between density fluctuations and stress at the yield point on the S-S curve. The scattering intensity immediately increased, and voids were generated. In the case of the LLDPE, the butterfly pattern was observed at the first yield point. The enhancement of the scattering intensity was smaller than that of HDPE, and the second yield point appeared with voids. In other words, the strain-induced density fluctuations (SIDF) on the submicron scale dominate the mechanical properties of PE.

In Chapter 5, in order to clarify the factors governing the SIDF in PE, I observed the changes in the hierarchical structures of various LLDPE with different comonomer characteristics by USAXS, SAXS, and WAXS under tensile testing. I found that the SIDF are suppressed when the density fluctuations on the submicron scale before stretching are small or when the decrease in the crystallinity during stretching is large.

In Chapter 6, in order to clarify the local inhomogeneity of chain orientation associated with the SIDF of PE, I performed STXM observations on the stretched PE samples. I was able to visualize the density fluctuations and the spatial inhomogeneity of the orientation on the submicron scale by varying the incident X-ray energy, respectively. In the high-crystallinity region, no significant change was observed in the orientation, while in the low-crystallinity region, the chains oriented in the direction parallel to the

stretching direction were observed. In addition, the decrease in the optical density due to mechanical melting was observed.

List of Publications

1. “A Study on the Isothermal Crystallization of Poly(3-methylbutene-1)”
   Kishimoto, M.; Mita, K.; Jang, J.; Takahashi, N.; Ogawa, H.; Nishida, K.; Kanaya, T.; Takenaka, M.
   Polymer Journal **2019**, *51*, 173–182.
   (Chapter 2)

2. “Spatial Distribution of the Amorphous Region Constrained by Polymer Crystallites”
   Kishimoto, M.; Takenaka, M.; Iwabuki, H.
   To be submitted.
   (Chapter 3)

3. “Effect of Submicron Structures on the Mechanical Behavior of Polyethylene”
   Kishimoto, M.; Mita, K.; Ogawa, H.; Takenaka, M.
   Macromolecules **2020**, *53*, 9097–9107.
   (Chapter 4)

4. “Strain-Induced Density Fluctuations in Linear Low-Density Polyethylene”
   Kishimoto, M.; Mita, K.; Ogawa, H.; Takenaka, M.
   To be submitted.
   (Chapter 5)

5. “Spatial Inhomogeneity of Chain Orientation Associated with Strain-Induced Density Fluctuations in Polyethylene”
   Arakawa, M.; Kishimoto, M.; Nakanishi, Y.; Mita, K.; Takenaka, M.
   Polymer Journal **2022**, *54*, 243–248.
   (Chapter 6)

Other Publications

6. "Distribution of Glass Transition Temperatures T_g in Polystyrene Thin Films as Revealed by Low-Energy Muon Spin Relaxation: A Comparison with Neutron Reflectivity Results"
Kanaya, T.; Ogawa, H.; Kishimoto, M.; Inoue, R.; Suter, A.; Prokscha, T.
Physical Review E **2015**, *92*, 022604.

7. "Decagram Scale Production of Deuterated Mineral Oil and Polydecene as Solvents for Polymer Studies in Neutron Scattering"
Klenner, M. A.; Cagnes, M.; Wood, K.; Mita, K.; Kishimoto, M.; Darwish, Tamim.
Polymer Chemistry **2020**, *11*, 4986–4994.

Acknowledgments

The present thesis is based on the study carried out at the Institute for Chemical Research (ICR), Kyoto University, from 2018 to 2022.

The author would like to express his most sincere thanks to Prof. Mikihito Takenaka for his continuous guidance, encouragement, valuable comments, and discussions through the course of the study.

Prof. Tsuyoshi Koga and Prof. Yo Nakamura are especially acknowledged for their critical review of this thesis.

The author would like to express his sincere thanks to Assoc. Prof. Hiroki Ogawa and Assist. Prof. Yohei Nakanishi for their helpful advice and encouragements, and he also thanks to all the members of Takenaka laboratory for their kind help.

The author wishes to express his gratitude to Prof. Toshiji Kanaya, Assoc. Prof. Koji Nishida, and Assoc. Prof. Rintaro Inoue for their guidance and teaching him the joy of discovery when he was a master course student.

The author greatly thanks Dr. Kazuki Mita and Mr. Kiminori Uchida (Mitsui Chemicals) for valuable discussions and opportunities for the synchrotron radiation X-ray experiments.

The author wishes to thank Dr. Hitoshi Iwabuki (Industrial Technology Center of Okayama Prefecture) for the pulsed ^{1}H-NMR measurements and valuable discussions.

The author is sincerely grateful to Assoc. Prof. Masatoshi Tosaka for his kind support in the SAXS measurements with Nanoscale Dynamic Structural Analysis X-ray System at ICR; to Dr. Hiroyasu Masunaga and Dr. Taizo Kabe (JASRI) for their kind

support in the USAXS, SAXS, and WAXS measurements at SPring-8 BL03XU; to Assist. Prof. Yasuo Takeichi, Assist. Prof. Shohei Yamashita, and Assist. Prof. Daisuke Wakabayashi (KEK) for their kind support in the STXM observation.

The synchrotron radiation X-ray experiments included in this thesis are listed as below.

Proposal No.	Facility	Beamline No.	Corresponding Chapter
2013B7266	SPring-8	BL03XU	Chapter 2
2014A7217	SPring-8	BL03XU	Chapter 2
2014B7266	SPring-8	BL03XU	Chapter 2
2015B7267	SPring-8	BL03XU	Chapter 2
2016A7217	SPring-8	BL03XU	Chapter 2
2016B7266	SPring-8	BL03XU	Chapter 2
2017A7215	SPring-8	BL03XU	Chapter 2 and 4
2017B7267	SPring-8	BL03XU	Chapter 4 and 5
2018A7217	SPring-8	BL03XU	Chapter 4 and 5
2018B7267	SPring-8	BL03XU	Chapter 4 and 5
2019A7215	SPring-8	BL03XU	Chapter 4 and 5
2019B7264	SPring-8	BL03XU	Chapter 4 and 5
2020G091	Photon Factory	BL-19A	Chapter 6
2020Y016	Photon Factory	BL-19A	Chapter 6

Finally, the author wishes to express his heartfelt thanks to his family for their continuous support and encouragement.

March 2022

Mizuki Kishimoto